Forschungszentrum Jülich
in der Helmholtz-Gemeinschaft

Institut für Werkstoffe und Verfahren der Energietechnik
Institut 1: Werkstoffsynthese und Herstellungsverfahren

Manufacture and Characterisation of Composite Graded Filter Membranes for Microfiltration

Li Zhao

Jül-4079

Manufacture and Characterisation of Composite Graded Filter Membranes for Microfiltration

Li Zhao

Berichte des Forschungszentrums Jülich ; 4079
ISSN 0944-2952
Institut für Werkstoffe und Verfahren der Energietechnik
Institut 1: Werkstoffsynthese und Herstellungsverfahren Jül-4079
D294 (Diss., Bochum, Univ., 2003)

Zu beziehen durch: Forschungszentrum Jülich GmbH · Zentralbibliothek
D-52425 Jülich · Bundesrepublik Deutschland
☎ 02461/61-5220 · Telefax: 02461/61-6103 · e-mail: zb-publikation@fz-juelich.de

Abstract

Microfiltration is specifically the filtration of substances that range in size from 0.05 μm to 10 μm, which has two common forms – through-flow (dead-end) and cross-flow. Microfiltration is used in both production and analytical applications, such as the filtration of particles from liquid or gas streams for different industries, e.g. chemical or pharmaceutical, clarification and sterile filtration and waste water treatment etc.

In this work composite microfiltration membranes were developed combining rugged substrates (both planar and tubular) made of sintered stainless steel powder with a patented coating technology – the wet powder spraying (WPS) method, in which a sintered titanium dioxide layer is permanently bonded to the porous stainless steel substrates. Through the optimisation of a conventional composition of the TiO_2 suspension, the spraying process of the WPS method and the sintering process of the graded structure, stable TiO_2 membrane layers are being developed with an average pore size of 0.1 μm and a thickness of 20~30 μm. Due to the utilisation of the ultrasonic wave and grinding methods the imperfections in the membranes could be decreased distinctly.

In order to investigate the flow process inside the graded structure, mathematical models were developed to simulate the flow rate both by fluid and gas. A modification was done to improve the models through comparing the calculated results with the measured results, which proved furthermore that the models were quite reliable in the simulation of such structures.

Kurzfassung

Mikrofiltration ist insbesondere die Filtration von Substanzen im Größenbereich von 0.05 bis 10 μm, die zwei übliche Formen aufweist – Durchströmung (totes Ende) und Kreuzstrom. Mikrofiltration wird sowohl in der Produktion als auch bei analytischen Anwendungen wie der Filtration von Teilchen aus Flüssig- oder Gasströmen für verschiedene Industrien, z.B. die Chemie- oder Pharma-Industrie, bei der Klärung und Sterilfiltration und in der Abwasseraufbereitung eingesetzt.

In der vorliegenden Arbeit wurden ein Mikrofiltrationsverbundmembran entwickelt, die robuste Substrate (sowohl planar als auch rohrförmig) aus gesintertem Edelstahlpulver mit einer patentierten Beschichtungstechnik – dem Nasspulverspritzen (WPS) kombinieren, wobei eine gesinterte Titandioxidschicht dauerhaft an die porösen Edelstahlsubstrate gebunden wird. Durch Optimierung einer herkömmlichen Zusammensetzung der TiO_2-Suspension in Verbindung mit dem Spritzverfahren der WPS-Methode und dem Sintern der gradierten Struktur werden stabile TiO_2-Membranschichten mit einer Porengröße von 0.1 μm und einer Dicke von 20~30 μm entwickelt. Durch Verwendung der Ultraschallwellen- und Mahlverfahren konnten die Störstellen in den Membranen deutlich verringert werden.

Zur Untersuchung des Strömungsprozesses in der gradierten Struktur wurden mathematische Modelle entwickelt, um die Strömungsrate sowohl durch Flüssigkeit als auch durch Gas zu simulieren. Eine Modifikation wurde durchgeführt, um die Modelle über den Vergleich der berechneten mit den gemessenen Ergebnissen zu verbessern, was darüber hinaus bewies, dass die Modelle in der Simulation solcher Strukturen recht zuverlässig waren.

Manufacture and Characterisation of Composite Graded Filter Membranes for Microfiltration

1 Introduction

Filtration has been identified traditionally as the separation of particulate material from a fluid mixture by the passage of most of the fluid through a porous material (the filter) that entraps the solids in its matrix or retains them on its surface (dead-ended filtration), or rejects the solids and allows them to continue along with a circulating feed stream (cross-flow filtration). The driving force for the process is the pressure difference applied across the filter, chemical potential or concentration difference etc. The most common definition of a membrane is that it is an interphase that divides two bulk phases.

From dairy applications to high-tech processing membrane separation systems are used for a wide variety of applications in a broad cross-section of industries, including power, waste treatment, textile, grain, food and beverage, pharmaceutical, biotechnology and many others [1, 2, 3].

Depending upon the intended use, membranes may be produced in many different configurations; for example, cartridges, plate and frame devices, tubes, disks, etc. Commonly used membrane substrate materials include polymeric compounds (organic membrane), sintered ceramic and metallic materials (inorganic membrane). According to the performance characteristics, membranes are placed in one of four categories; microfiltration (MF), ultrafinefiltration (UF), nanofiltration (NF) and reverse osmosis (RO). These categories deal mainly with the membrane's ability to reject or separate various size particles or molecules [1, 2].

Microfiltration is becoming increasingly popular as the preferred mode for a large variety of filtration applications involving separation and concentration of particulate suspensions or solutions, the recovery of low molecular weight substances and in some instances the recovery of macromolecules such as proteins; generally, the pore diameters of the MF membranes range from 0.05 to 10 micron [1, 2, 4].

The development of industrial inorganic microfiltration membranes gets rid of the limitation of polymeric membranes in terms of temperature, pressure, durability and cleaning ability; furthermore, they avoid the brittleness of traditional glass and ceramic monolayer membranes. The first attempt to use the high mechanical resistance of inorganic supports probably dates back to the 1960s, when dynamic membranes made of a mixture of zirconium hydroxide and polyacrylic acid deposited on a porous carbon or ceramic support were developed by the Oak Ridge National Laboratory in the United States [5, 6]. This also leads to the development of a new concept — composite microfiltration membranes (asymmetric filter membrane also) ,

which consist of two or more layers made of the same or different materials, for example: metallic substrate with ceramic applied layer. The porosity of each layer consists of a well-controlled size range to provide the desired separation selectivity. For such membranes, one side they combine high thermal capability and good thermal shock resistance, high chemical stability, high mechanical strength, good cleaning ability by means of high pressure or back flushing, and longer life time than polymer filters resulting in lower running costs; the other side the graded structure ensures a high permeability at a low pressure drop. The additional cost of these filters — caused by the more expensive manufacturing route — is largely compensated by greater lifetime and higher reliability [2, 4, 7-11].

The process employed to fabricate the filtermembrane is largely dependent upon the materials, the pore characteristics desired, and the specific physical characteristics to be improved. The earliest and most widely used materials for metallic supports are bronze and stainless steel [8, 12]. Then Ti, Zr, Pt and Ni began to be produced and used in filters by powder metallurgical techniques [13]. In general sintered metal filters fall into two categories: those produced by sintering loose powder in a mould (e.g. isostatic pressing), and those produced by compaction (e.g. uniaxial pressing) [14]. For the applied ceramic functional layer, which acts as microfiltration membrane, the common used materials are ZrO_2, Al_2O_3, TiO_2, SiO_2 [15-41], accordingly, slip casting [15, 32, 33, 35] and sol-gel [19-25, 31, 39-43] methods are adopted normally; the latter permits ultrafilter membranes to be obtained. Some other coating methods altered from gelcasting [44] to sedimentation casting [28, 29].

Aim of this Work

It is well known that graded metallic membranes have been successfully produced by the Wet Powder Spraying (WPS) technique [45-48]. By the means of this manufacture method, planar as well as tubular composite membranes can be produced using the same equipment. Using this technique graded filters completely made of stainless steel powder have been developed by Forschungszentrum Jülich and the know-how has been transferred to GKN. Based on this knowledge, a development of a microfiltration membrane consisting of an additional ceramic layer onto a metallic substrate was made in this work. The metallic supports are commercial Sika R® series produced by GKN Sinter Metals Filters GmbH. Based the already reported good performance of the asymmetric (composite) filter structure (e.g. TiO_2 onto stainless steel substrates) [35-37], TiO_2 powder is chosen as the functional-layer material to be coated onto the stainless steel substrates. Intermediate layers made of 316L stainless steel powder (the same as that of the substrate) are adopted here, which can prevent the penetration of the precursor of the top layer material into the pores of the support during the synthesis and the

collapse of the thin finished top layer into the large pores of the support. Furthermore, with the variation of the pore size and thickness of these layers, it helps to regulate the pressure drop across the top layer of the membrane to some extent.

The main part of this work is to develop aforementioned composite membranes on commercial substrates from GKN Sinter Metals Filters GmbH (Radevormwald, Germany) by applying the WPS technique. The average pore size of the functional layer should be approximately 0.1 μm and the thickness of this layer should be in the range of 20~30 μm. The main procedures include the optimisation of the suspensions, the optimisation of the spraying process both for the planar and tubular samples, and the optimisation of the sintering process. Additionally, some theoretical analyses were done to investigate the imperfections occurring in the layers; a mathematical model was set up to simulate the flowing process of the graded structure, so that the flow rate of the filters can be calculated depending on the thickness of the layers at a given pressure drop; vice versa, if a flow rate is required, the thickness of the functional filtration layer can be solved by the model.

2 Microfiltration Membranes

2.1 Definition and Classification of Membrane Separation Processes

Filtration is defined as the separation of two or more components from a fluid stream based primarily on size differences. In conventional usage, it usually refers to the separation of solid immiscible particles from liquid or gaseous streams. Membrane filtration extends this application further to include the separation of dissolved solutes in liquid streams and for separation of gas mixtures.

The primary role of a membrane is to act as a selective barrier. It should permit passage of certain components and retain certain other components of a mixture. By implication, either the permeating stream or the retained phase should be enriched in one or more components. Membranes can be classified by a.) nature of the membrane — natural versus synthetic; b.) structure of the membrane — porous versus nonporous, its morphological characteristics, or as liquid membranes; c.) application of the membrane — gaseous phase separations, gas-liquid, liquid-liquid, etc.; d.) mechanism of membrane action — adsorptive versus diffusive, ion-exchange, osmotic, or nonselective membranes [2].

Fig. 2-1 shows a classification of various separation processes based on particle or molecular size and the primary factor affecting the separation process [2, 49, 50]. The major membrane separation processes — reverse osmosis (RO), nanofiltration (NF), ultrafiltration (UF) and microfiltration (MF) — cover a wide range of particle/molecular sizes and applications. Among membrane separation processes, the distinction between the various processes is somewhat arbitrary and has evolved with usage and convention.

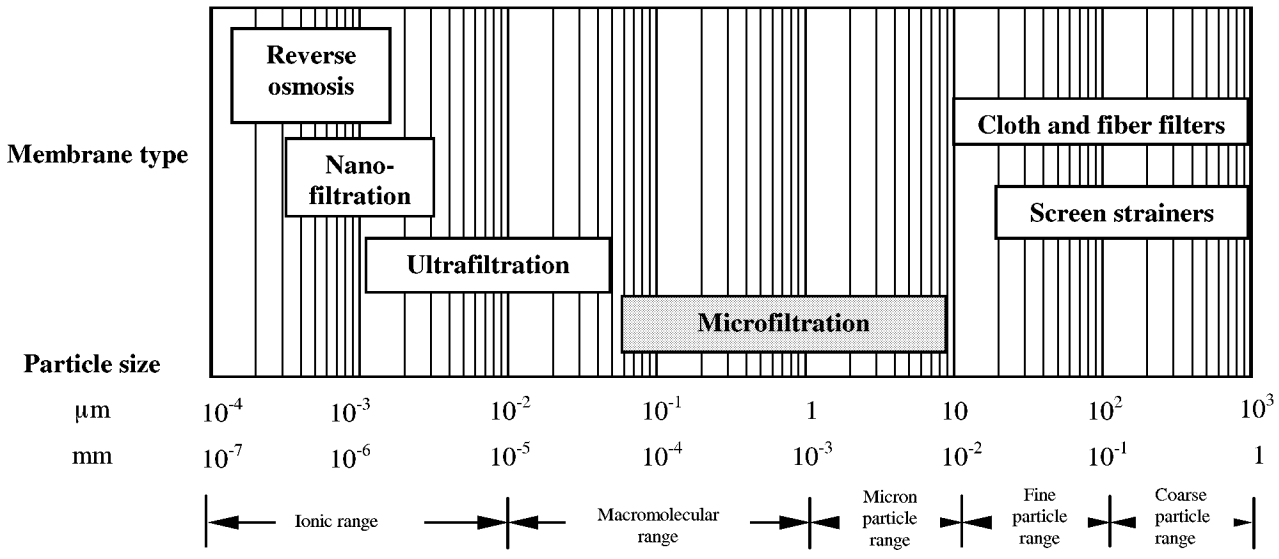

Fig. 2-1 Useful ranges of various separation processes [2, 49, 50]

Table 2-1 shows the characteristics of various membrane processes [1, 2]. What distinguishes the more common pressure-driven membrane processes — reverse osmosis, nanofiltration, ultrafiltration, and microfiltration — is the application of hydraulic pressure to speed up the transport process. Of course, it is not easy to give a very exact definition of the ranges according to the classification [50]. In its ideal definition, reverse osmosis retains all components other than the solvent (e.g., water) itself, which are capable of retaining not only electrolytes, but also small organic molecules. Nanofiltration membranes allow small-molecular solutes to permeate together with the water molecules. Macromolecules, such as proteins, with molecular weights between 5000 and 1000000, can be retained by ultrafiltration, the particles size should be in the range of 0.001-0.02 μm. Microfiltration, on the other hand, is designed to retain colloidal and suspended particles in the micro range of 0.05 μm to about 10 μm [1, 2, 4].

Table 2-1 Characteristics of membrane processes [1, 2]

Process	Driving Force	Retentate	Permeate
Reverse osmosis	pressure	all solutes	water
Nanofiltration	pressure	small molecules, divalent salts, dissociated acids	monovalent ions, undissociated acids, water
Ultrafiltration	pressure	large molecules	small molecules, water
Microfiltration	pressure	suspended particles	dissolved solutes, water

In all membrane filtration processes there exist two basic forms — through-flow (dead-end) and cross-flow. In through-flow configuration, the feed flow is perpendicular to the membrane surface. In cross-flow configuration, the feed stream flows parallel to the membrane surface and the cross-flow velocity can have a significant influence on flux. The former is referred to as surface (as opposed to depth) filtration also. In conventional surface filters, the filtered solids are allowed to build up as a cake at the surface of the filter, as shown in Fig. 2-2 a.). If such a principle were adopted for membrane filtration, the permeation rate through the combined membrane and surface cake layer would, in most applications, quickly fall to very low levels. Therefore, in all applications of reverse osmosis, nanofiltration and ultrafiltration, and in many applications of microfiltration, a crossflow is used to prevent this cake formation. The term crossflow refers to the direction of the feedstream tangentially over the surface of the membrane, in order to sweep rejected solutes away from the membrane, as shown in Fig. 2-2 b.). Because of the use of crossflow, membrane filtration processes separate

fluids into two product streams. There are the permeate, which is depleted of certain solutes, and the concentrate or retentate, which is enriched in those solutes.

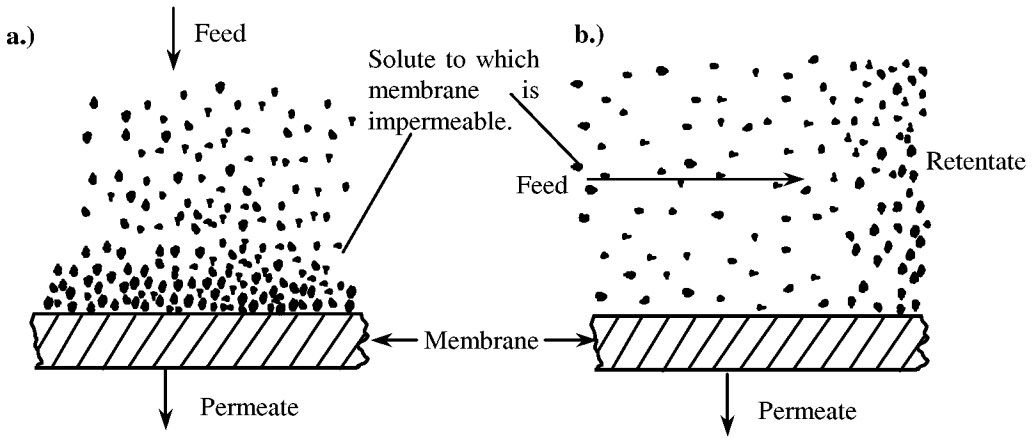

Fig. 2-2 Illustration of pressure-driven membrane process a.) through-flow filtration, b.) cross-flow filtration [1]

Terms such as symmetric and asymmetric are classified by the structure of the membranes. Symmetric membranes are systems with a homogeneous structure throughout the membrane. Asymmetric membranes have a gradual change in structure throughout the membrane. In most cases these are composite membranes consisting of several layers with a gradual decrease in pore size to the feed side of the membrane [51]. Fig. 2-3 a.) and b.) show the images of these two kinds of membranes.

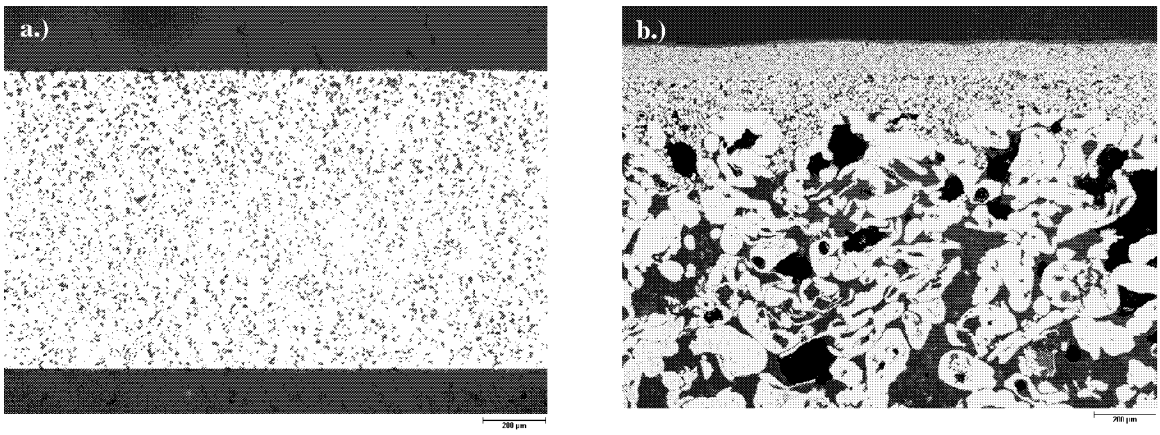

Fig. 2-3 Schematic representation of two types of membranes.
a.) symmetric membranes, b.) asymmetric membranes

The basic idea behind the asymmetric structure is to minimise the overall hydraulic resistance of the permeate flow path through the membrane structure. The permeate flux through a given layer is inversely proportional to the layer thickness and is, under simplified assumptions, proportional to some power of the pore size of the porous layer. It is, therefore, desirable to

have a separate layer (functional layer, membrane) as thin as possible and yet possessing defect-free physical integrity, and one or more layers of support which provide the necessary mechanical strength with negligible hydraulic resistance. This also helps to reduce the pressure required for back-flushing in microfiltration cleaning. The main advantage of asymmetric structures is the higher flow rate at a given pressure drop than the symmetric one due to the predominantly lower thickness of the functional filtration layer. The comparison of the flow rate of these two structures (Fig. 2-3 a.) and b.)) is shown in Fig. 2-4.

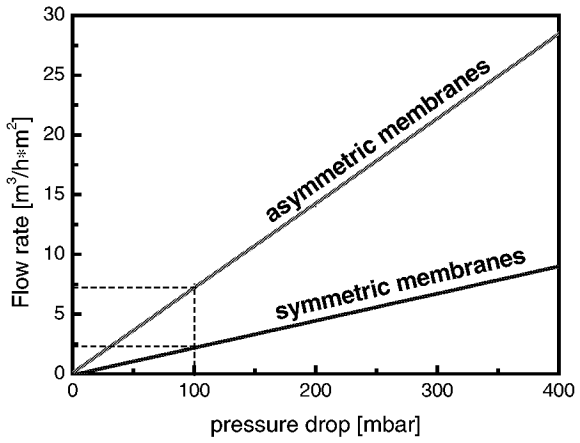

Fig. 2-4 Comparison of the flow rates of two different membrane structures, which are shown in Fig. 2-3 a.) and b.)

2.2 Synthesis Methods

There are different methods for formation of the membranes; however, membranes can be divided into two main groups, i.e.: organic membranes and inorganic membranes. Inorganic membranes can be divided further into metallic ones and ceramic ones. A comparison of different filter membranes is listed in Table 2-2 [8, 12, 13, 15-41, 51, 52].

Most of the industrial inorganic microfiltration membranes are of asymmetric structure, i. e. consist of a porous support and one or more filtration layers. The porous supports of the membranes are made of powders, which are sintered in order to obtain a unique structure, construction and rigidity. The filtration coating can be made of the same material as that of the support or other materials (the latter are also namely composite membranes), in which the thick and porous structure is serving as a mechanical support for a thin filtration layer [4].

It is noteworthy here that the microfiltration membranes made of metallic supports and ceramic applied layers lead to a combination of the advantages both of metallic and ceramic membranes. The construction of such membranes and the sintering process cause that these membranes have a very high resistance to organic and inorganic solvents, high pressures and

high temperatures and an improved cleanability. The main disadvantage is the relatively high production cost.

Asymmetric membranes produced by packing of particles from dispersions have the general structure as shown in Fig. 2-3 b.). The main support consists of a packing of rather coarse-grained material (micron range) which is produced in a classical way by uniaxial or cold isostatic pressing of a dry powder, by co-extrusion of a paste of ceramic powder with additions of binders and plasticisers or by slip-casting [14, 53]. After burning away the organic materials the so-called „green“ compact is sintered. In order to obtain detect-free membranes, thin top layers on the support system must fulfil more stringent requirements than

Table 2-2 Comparison of different materials commonly used for filter applications [8, 12, 13, 15-41, 51, 52]

clasisification / comparison	Inorganic membranes		Organic membranes
	Metallic Filters	Ceramic Filters	Polymeric Filters
materials	Stainless steel, bronze nickel titanium, zirconium Platium, Silver Monel, Inconel Hastelloy	Al_2O_3 ZrO_2 TiO_2 SiO_2	polysulphone TFE fluorocarbon polyamide polyethylene polyacrylonitrile
mechanical stability	reusable stable pore size distribution ductile behaviour	reusable, but handle with care due to the high brittleness	not reusable
chemical stability	corrosion resistance in case of suitable alloys	corrosion resistance	sensitive to corrosion environments
cleanability	cleanable (ultrasonic, hot steam, back flush, chemical, thermal)	limited cleanability due to the high brittleness	not cleanable
temperature resistance	high temperature resistance compatible with high heating and cooling rates	high temperature resistance incompatible with high heating and cooling rates	temperature-sensitive incompatible with high temperatures
ranges of filtration	particle retention microfiltration	microfiltration ultrafiltration nanofiltration	microfiltration ultrafiltration nanofiltration reverse osmosis

the one utilised in the manufacture of commercially available porous materials. Pore size distribution and roughness must be smaller than usual. The ways to obtain these characteristics are largely classified with practically no published information.

The quality of the support is especially critical if the formation of the top layer is mainly determined by capillary action on the support. Then, besides a narrow pore size distribution the wettability of the support system plays a role [51, 54]. In cases where the precursor particles of the membrane layer are very small in size compared to the pore size of the bulk of the support, the membrane particles can significantly penetrate the support pores and the resulting permeability of the membrane/support composite will deteriorate. A practical solution is to add one or more intermediate layers, whose pore sizes and thickness lie between those of the bulk support and membrane layer. The intermediate layer can be used to improve the quality of the support system.

To obtain smaller pore sizes as indicated above it is necessary to use fine-grained powders and suspensions in producing the top layer. This is obvious in well-packed systems of uniform particles, where the mean pore diameter is minimum, depending on the packing structure. Therefore, suspensions or pastes are prepared from a powder having a narrow particle size distribution. This implies a very good control of the agglomeration state of the material by deagglomeration treatments (e.g. milling, ultrasonification, moisturising the support surface and so on) and/or removal of the fraction with the largest diameters e.g. by sedimentation [51]. The most commonly used route for the top layer synthesis with packing methods are the slip-casting [15, 32, 33, 35] and sol-gel processes [19-25, 31, 39-43]. Combining the manufacturing technology and the applied materials of the membrane layer, the common category of the microfiltration can be also classified as alumina, zirconia, titania and silica membranes [4, 15-41, 51].

2.3 Commercial Products Overview

Today's inorganic microporous membranes are typically based on ceramics, although a few other materials are used as well, such as metal or carbon.

Industry sources estimate that about $30 million dollars per year of ceramic membrane modules for cross-flow liquid separations are sold. Microfiltration membranes are useful in all branches of industry where there is a need of separation, clarification, fractionation and concentration of both organic and inorganic matters. For example, food, dairy and beverage applications (including fruit juice clarification, and filtering wine and beer) account of about 50% of demand. Applications in biotech, pharma, water and wastewater treatment are also significant [55].

The development of industrial inorganic microfitration (MF) and ultrafiltration (UF) membranes resulted from the combination of three factors: a.) the know-how accumulated by the companies that built the nuclear gaseous diffusion plants; b.) the existence of ultrafiltration as an industrial process using polymeric membranes; c.) the limitations of polymeric membranes in terms of temperature, pressure and durability [7]. Particularly the porous ceramic membranes are essentially the side-products of the earlier technical developments in gaseous diffusion for separating uranium isotopes in the United States and France.

The first attempt to use the high mechanical resistance of inorganic supports probably dates back to the 1960s, when dynamic membranes made of a mixture of zirconium hydroxide and polyacrylic acid deposited on a porous carbon or ceramic support were developed by the Oak Ridge National Laboratory in the United States [5, 6]. The concept later evolved into the Ucarsep® membrane made of a layer nonsintered ceramic oxide (including ZrO_2) deposited on a porous carbon or ceramic support, which was patented by Union Carbide in 1973 [56].

All major industrial participants in the development that took place in the period 1980-1985, were companies which actively participated in the development and manufacture of inorganic membranes for nuclear applications. The pioneering work was performed by two companies that were most active in this program, namely SFEC and Ceraver [7].

In 1980, SFEC began selling complete ultrafiltration plants under the trademark of Carbosep®. Since membranes no longer had important nuclear applications in future, SFEC was sold in 1987 by the CEA to the French Company Rhone-Poulenc which merged them with their polymeric membrane division to form the new subsidiary, currently known ZrO_2- or TiO_2- based ultrafiltration membranes on 6 mm inner-diameter carbon tubes under the corporation name of Miribel [7, 55].

Ceraver developed a range of α-Al_2O_3 microfiltration membranes on an α-Al_2O_3 support with two key features: first, the multichannel support and second, the possibility to backflush the filtrate in order to slow down fouling. Since 1984 these membranes, which have 19 channels per element with 4 mm channel diameter are sold under the trademark Membralox®. The first generation Membralox® were essentially developed for MF applications. The second innovative feature of the Membralox® membranes was the possibility to backflush, a feature, the Carbosep® membranes did not offer. The ability to backflush can be very beneficial because in numerous applications fouling decreases the flux through a microfiltration down to roughly similar range of values as those obtained with an ultrafiltration membrane.

Backflushing is thus necessary to fully exploit the possibility of high flux offered by the relatively larger pore diameter (0.05~10 μm) of microfiltration layers [57].

In 1986, CGE, which by then had its primary focus in the energy and communication businesses, divested its association from materials, and sold the ceramic part of Ceraver, including the ceramic membranes division to Alcoa. Under the name U.S. Filter/SCT (acquired from Alcoa Separations Technology) it is now a subsidiary of the Vivendi Company (acquired in 1999) [55].

A few other players in the nuclear membranes activity also developed inorganic membranes for the filtration of liquids. This was the case with Norton-USA who with the know-how of Euroceral developed MF membranes made of an α-Al_2O_3 tubular support with an α-Al_2O_3 layer. These membranes were sold by Millipore under the trademark Ceraflo®. Now it is a subsidiary of U.S. Filter/SCT also [55].

Significant developments in microporous ceramic membranes over the last several years include Tami's emergence as a significant player behind U.S. Filter/SCT and Orelis (formerly TechSep) and U. S. Fiter's acquisition of Schumacher, which has partly acquired the technology from TriDelta (a German ceramic membrane manufacturer). Alumina, Zirconia and Titania modules are applied in different industrial branches [55].

Porous metals have long been commercially available for particulate filtration [8, 12, 13]. They have been used in some cases as microfiltration membranes that can withstand harsh environments, or as porous supports for dynamic membranes. Stainless steel is by far the most widely used porous metal membrane. Other materials include bronze, silver, nickel, Monel, Hastelloy and Inconel. Their recommended maximum operating temperatures range from 200 to 650°C. Depending on the pore diameter which varies from 0.2 to 5 microns, the water permeability of these symmetric membranes can exceed 3000 L/h-m^2-bar and is similar to that obtained with asymmetric ceramic microfiltration membranes [58]. Due to the relatively high costs of these membranes, their use for microfiltration has not been widespread. Only a few companies offer membrane products on a commercial scale: GKN (Sika-R®), Fairey Microfiltrex, Pall (PMM®), Mott, Osmonics (Duratrex®) and so on. Total annual sales of cross-flow metal membrane devices from these companies are believed to be close to $55 million dollars per year, if microporous filter elements with pore sizes of less than 10 microns are included in the estimate. About 75% of applications are used for liquid separations, primarily in the chemical and petrochemical industry. Particle recovery from gas is believed to make up the remaining 25% of the business.

As talking about composite microfiltration membranes, the products composed of TiO_2 onto tubular stainless steel support developed and patented by DuPont must be mentioned. Now Graver Separations, Inc. purchases the technology and the trademark is Scepter®. The modules are used primarily in liquid separations systems in sugar, corn wet milling, caustic recovery, and other food and beverage applications, which were proved to have a good performance [4, 36, 37].

Table 2-3 lists the major microfiltration membrane and module producers and manufacturers, as well as their products [55, 58].

Table 2-3 Commercial inorganic microfiltration membranes and filters [55, 58]

Manufacturer	Trade Name	Membrane Material	Support Material	Membrane Pore Diameter [μm]	Geometry of Membrane	Remarks
aaflowsystems Essingen, GER		AL_2O_3	AL_2O_3	0.1, 0.2, 0.5, 0.8, 1.4	monolith/tube	applications in food and dairy, process water
		ZrO_2	AL_2O_3	0.02, 0.05, 0.1	monolith/tube	
		TiO_2	AL_2O_3	0.005	monolith/tube	
Anotec Separations (owned by Whatman plc) Banbury, UK	Anopore®	AL_2O_3	none	0.02 to 0.2	flat disks, dead-end devices	laboratory scale liquid separation
Aquamarijin Micro Filtration BV Hengelo, Neth	Microsieve®	ceramic, metallic, polymeric	silicon, other	0.1 to 100	flat disks	very narrow pore size distribution
Atech innovations GmbH Gladbeck, GER		AL_2O_3	AL_2O_3	0.1, 0.2, 0.4, 0.8, 1.2	monolith/tube	-
		ZrO_2	AL_2O_3	0.01, 0.05	monolith/tube	
		TiO_2	AL_2O_3	0.01, 0.05	monolith/tube	
Ceror Separations Corning, NY		ceramic oxides	mullite	0.005 to 0.5	monolith/tube	liquid separation gas filtration
		ceramic oxides	mullite	0.5	plate	
Coors Technology, Inc. Golden, CO	CeramicaÅ®	AL_2O_3	AL_2O_3	0.2, 0.8, 5	tube	Liquid separation
	CeramicaÅ®	ZrO_2	AL_2O_3	0.04	tube	
Fairey Industrial Ceramics Ltd. Staffordshire, UK	Strata-Pore®	AL_2O_3	AL_2O_3	0.2, 0.35, 1.2, custom	tube	Owned by Fairey Group, plc

Fairey Microfiltrex Ltd. Hampshire, UK		metal fibres or powdered metal	none	≥ 3	plate/tube	
GKN Sintermetals Filters GmbH Radevormwald, GER	Sika- R®	metal powder or fibre	metal powder or fibre	0.5 and larger	plate/tube	liquid and gas filtration
Graver Separations, Inc. Glasgow	Scepter® Scepter®	TiO_2 ZrO_2, other	SS SS	0.1 to 1.0 0.001 to 0.1	tube tube	inside coated tube
Miribel, France	Carbosep® Kerasep®	ZrO_2 - TiO_2 ZrO_2 - TiO_2	carbon AL_2O_3 - TiO_2	0.14; 15, 50, 150, 300 kD 15, 150, 300 kD; 0.01, 0.2, 0.45, 0.8, 1.4	tube tube	acquired from SFEC
NGK Insulators, Ltd. Nagoya, Janpan	Cefilt® Cefilt®	AL_2O_3 TiO_2	AL_2O_3 AL_2O_3	0.1 to 5.0 0.004 to 0.05	tube tube	drinking- and wastewater
Osmonics, Inc. Minnetonka, MN	Ceratrex® OSMO® Duratrex®	AL_2O_3 Ceramic metal powder silver	AL_2O_3 AL_2O_3	0.02 to 25 0.005 to 5.0 0.2, 0.5, 2, 5, 10, 20, 40 100 0.2, 0.45, 0.8, 1.2, 3.0, 5.0	plate tube tube tube	manufact. in Phoenix, AZ used in lab scale
Pall Corporation	PMM® PO5®	metal powder	none	0.2, 5, 10, 15, 20	tube	-
SpinTek Huntington Beach, CA		AL_2O_3, ZrO_2 TiO_2, SiO_2	SS (stain-less steel)	MF and UF	tube	treating waste and proces-sing water
Tami Industries Nyons, France		AL_2O_3 ZrO_2 TiO_2		0.14 to 1.4 15-300 kD 1-8 kD	plate/tube plate/tube plate/tube	liquid separation
U.S. Filter/SCT Tarbes, France	Ceraflo® Membralox®	AL_2O_3 AL_2O_3 ZrO_2 TiO_2	AL_2O_3 AL_2O_3 AL_2O_3 AL_2O_3	0.2 to 10 0.2, 0.5, 0.8, 1.4, 3.0, 5.0 0.02, 0.05, 0.1 1.0 and 5.0 daltons	tube tube tube tube	Nanofiltration membrane introduced in 1995
USF/Schumacher Crailsheim, GER	Schumasiv®	AL_2O_3 $ZrO_2 – TiO_2$	AL_2O_3 AL_2O_3	0.005 to 1.2	tube tube	liquid and hot gas filtration

Note: kD is kilo Dalton.

2.4 Characteristics of Filtermembranes

The separation efficiency (permeability) of inorganic microfiltration membranes depends, to a large extent, on the microstructural features of the membrane/support composites such as pore size and its distribution, pore shape, porosity and so on. For commercial inorganic membranes the membrane/support microstructures, geometry and other material-related properties must be taken into consideration for specific separation applications. The main characteristics of the filtermembranes will be addressed in the following [58, 59].

Porosity

Porosity is the fraction of the bulk volume of the porous sample that is occupied by pore or void space. Sometimes, this word is used inaccurately with a different meaning; for example, in the expression „graded porosity" of a filter consisting of layers of different grain sizes, „porosity" is not a measure of void fraction but rather of void size. Depending on the type of the porous medium, the porosity may vary from near zero to almost unity.

The various experimental methods used to determine porosities can be subdivided in the following categories: a.) optical methods; b.) imbibition method; c.) mercury injection method; d.) gas expansion method and f.) density methods [60, 61].

Permeability

Permeability is the term used for the conductivity of the porous medium with respect to permeation by a Newtonian fluid. The conductivity contributed by the porous medium is independent of both fluid properties and flow mechanisms, whose value is uniquely determined by the pore structure.

Typically, the liquid permeability is obtained with water being the permeate and expressed in terms of L/h-m^2-bar. The gas permeability is often expressed in terms of air or nitrogen permeability. In most cases, the „flow rate" of the above media is taken as a reference to scale the performance of different filter membranes.

Pore Size

Pore size plays a key role in determining permeability and permselectivity (or retention property) of a membrane. For gases, the pore size of the membrane also affects the prevailing transport mechanisms through the pores.

The structural stability of porous inorganic membranes under high pressures makes them amenable to conventional pore size analysis such as mercury porosimetry and nitrogen adsorption/desorption. The commercial mercury porosimeters can usually provide pore diameter distribution data in the range of 3.5 nm to 7.5 microns. It is a useful and commonly used method for characterising porous particles or bodies. For membranes with pore

diameters smaller than 3.5 nm (UF and NF), the nitrogen adsorption/desorption method based on the widely used BET theory can be employed [58]. Another possible solution to the problem of analysing multiple-layered membrane composites is a newly developed method using NMR spin-lattice relaxation measurements [62].

The most widely used industrial measuring method is so-called „bubble-point" test. The method essentially states that a given pressure difference is required to displace a liquid (having a surface tension and a contact angle with the pore surface) from a pore having a diameter „*d*" with a gas such as air or nitrogen. This method has been approved as an ASTM procedure [63].

The bubble point test is also often used for detecting failures of the membrane. If there are any cracks or pinholes in the membrane, the method will see them as the largest pores and the first bubbles will appear at a much lower than usual pressure.

Microscopy

A scanning electron microscope (SEM) generates electron beams and forms an image from the emitted electrons as a result of interaction between the bombarding electrons and the atoms of the specimen. With their improved resolution and competitive pricing, SEMs have become a basic surface and microstructural characterisation tool in membrane characterisation. Transmission electron microscopy (TEM) has higher resolution power than SEM and can be used to characterise some special membranes or their precursors. Some elemental analysis can be performed by SEM equipped with EDX. Also light microscope (LM) is an important supplement for characterising the cross section of the composite structure of membranes.

Thickness

The thickness of the separative membrane layer for asymmetric membrane structures represents a trade-off between the physical integrity requirement, on one hand; and the high flux requirement, on the other hand. Current commercial products show a membrane thickness of as thin as approximately 5 microns but generally in the 10 to 30 micron range. The bulk support and any intermediate support layers vary in thickness.

Due to the structural stability of inorganic membranes they do not suffer from any appreciable dimensional instability problems during machining process. So the thickness of different layers can be fixed by SEM or LM methods.

In order to prove chemical resistances and mechanical properties of inorganic membranes some other characteristics such as steam sterilisation and shear strength test are also done.

3 Experimental and Simulant

3.1 Starting Materials

3.1.1 Substrates

According to the two basic forms of filtration — through-flow (dead-end) and cross-flow the commercial products are mainly distinguished from planar (disks, plates) to tubular (tubes). Sika-R® serial products made of 316L stainless steel manufactured in GKN were taken as substrates for all attempts. Table 3-1 lists the information of the used substrates in detail, whose microstructures are shown in Fig. 3-1 a.) to c.).

Table 3-1 Description of the substrates used in this work

Name of the substrates	Manufacture route	Porosity [%]	Pore size distribution [µm]			Starting particle size [µm]	Geometry	Surface roughness* [µm]	
			d_{min}	MFP	d_{max}			R_a	R_m
Sika R 20 AX	co-axial pressing	43	12	20	37	200~300	disks, 3 mm thick ϕ 25 mm, ϕ 48 mm, ϕ 93 mm	10	110
Sika R 10 AX	co-axial pressing	43	12	17	25	100~200	disks, 3 mm thick ϕ 25mm, ϕ 56mm, ϕ 93mm	10	100
Sika R 15 IS Outside coating	isostatic pressing	36	13	19	45	200~300	tubes, 5, 10, 25 mm long ϕ_{out} 10 mm ϕ_{in} 5.8 mm	40	250

Note: MFP — average pore size; R_a — average roughness; R_m — maximum roughness; * measured by Surface Laser Profilometer (Polaris Cor.) by IWV-2, FZJ

3.1.2 Powders

TiO_2 powder < 0.3 µm from Kerr McGee was chosen as the functional layer material due to the lower sintering temperature comparing with Al_2O_3 and ZrO_2, a good adhesive property to

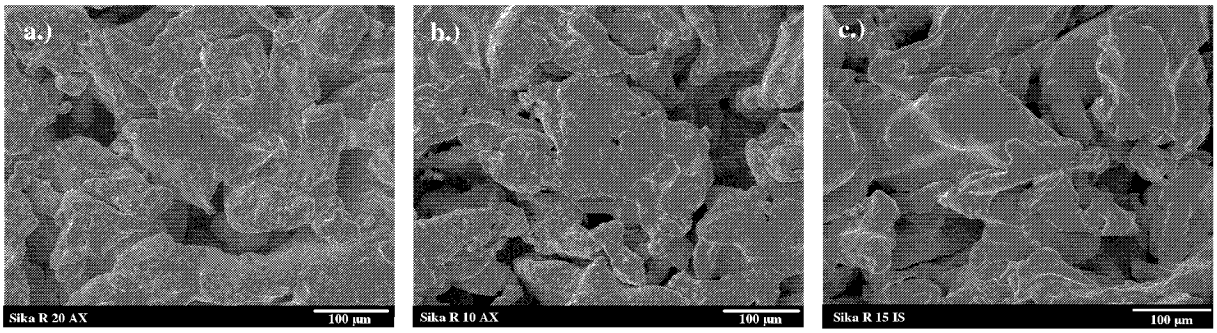

Fig. 3-1 Microstructures of different substrates, a.) Sika R 20 AX; b.) Sika R 10 AX; c.) Sika R 15 IS

the stainless steel substrates [35-37] and the required pore size (approx. 0.1 µm) of the membrane. The material of the intermediate layers was chosen the same as that of the substrate — 316L stainless steel for considering the integrity and stability of the graded structure. Table 3-2 and 3-3 give the information of the powders, whose microstructures are shown in Fig. 3-2.

Table 3-2 Information of the powders used in the work

Powders	Manufacturer & Trade name	Manufacture route	Nominal particle size [µm]	Particle size distribution [µm]*[a]			Density [g/cm^3]
				d_{10}	d_{50}	d_{90}	
TiO_2	Kerr McGee, GER Tronox® R-KB-3	sulfate process	< 0.3	0.03	0.18	0.43	4.1*[b]
316L (particle size < 5 µm)	Osprey, UK MP/316L®	gas atomisation	< 5	1.38	2.94	7.33	8.0[64]
316L (particle size < 16 µm)	Carpenter, FIN Anval 316L®	gas atomisation	< 16	4.23	8.79	18.07	8.0[64]

*a: measured by Laser Partikel Sizer (Fritsch, Analysette 22®) in IWV-1, FZJ; *b: nominal datum

Table 3-3 Nominal composition of the powders, [wt%]

R-KB-3[a]	TiO_2				Al_2O_3		
	0.95				0.05		
	Rutile-pigment, lattice-stabilised with Al_2O_3, powder coated with Al and organically treated						
	C	Cr	Ni	Mo	Si	Mn	Fe
316L (ST 1.4404[b])	0.03*	16.5/18.5	11.0/14.0	2.0/2.5	1.0*	2.0*	balance

a: data sheet of Kerr McGee; b: DIN 17440, 17445; * maximum

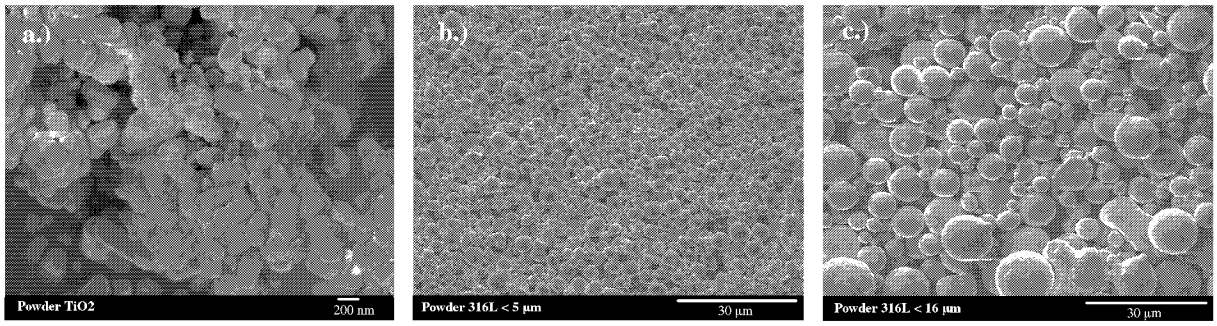

Fig. 3-2 Microstructure of the powders, a.) TiO_2 powder from Kerr McGee; b.) Powder 316L (particle size < 5 µm) from Osprey; c.) Powder 316L (particle size < 16 µm) from Carpenter

3.1.3 Chemicals

According to the synthesis method adopted for coating, a stable and homogeneous suspension is a predominant factor for obtaining a good layer-quality; therefore the chemicals used in the work have mainly three different applications: a.) carriers for the powders, for example,

Table 3-4 Information of the main chemicals used in the work

Chemicals	Manufacturer & Trade name	Properties
ethanol	AHK Alkoholhandelskontor Sorte 464	Molecular formula: C_2H_5OH Vapour pressure: 59 mbar (20°C) Density: 0.79 g/cm^3
terpineol	Merck Schuchardt α-terpineol to synthesise	Molecular formula: $C_{10}H_{18}O$ Vapour pressure: 0.24 mbar (40°C); Boiling point: 220°C Density: 0.94 g/cm^3 (20°C); not soluble in water
PVAc	Wacker Vinapas® B5 sp	Viscosity, 10% in ethyl acetate: 1.8 ± 0.2 mPas Density: 1.17 ± 0.01 g/cm^3 Molecular weight: 20-25 × 10^3
PEI	Sigma-Aldrich Ethylene imine polymer solution	Molecular formula: $\left[(CH_2)_2 - N\begin{matrix}H\\H\end{matrix}\right]$ ~50% in water Molecular weight: ~600000-1000000
HAc	Merck Acetic acid 96% to analyse	Molecular formula: CH_3COOH Vapour pressure: ~ 15 mbar (20°C) Density: 1.06 g/c m^3 (20°C)

ethanol, water and terpineol; b.) binder for the powders, for example, polyvenyl acetate (PVAc), and polyethylenimine (PEI); c.) dispersing agent for the suspensions, for example, acetic acid (HAc) and polyethylenimen (PEI). It must be mentioned here that PEI has two functions — binding and dispersing [69]. Table 3-4 lists the properties of the chemicals talked above.

3.2 Suspensions

3.2.1 Starting Point

Many experiences have been accumulated by IWV-1, FZJ to make metallic and ceramic powders into stable and homogeneous suspensions used for coating [45, 65-69]. A basis referencing these experiences on determining the composition of the suspensions was taken as a starting point for the following work. Table 3-5 shows the composition of the three different suspensions. The composition of TiO_2 suspension was based on a suspension developed for ZrO_2 powder used in SOFC project. The stainless steel suspensions were developed in a previous R&D project with GKN. The know-how has been transferred to GKN already for standard production of graded filters Sika R 0.5 AS and Sika R F AS.

Table 3-5 Initial composition of different suspensions used in this work

Suspension	Composition [wt%]	Milling
TiO_2	39.5% powder 59.3% ethanol 1.2% PEI	Mixing with ϕ 3 mm YSZ beads, powder : beads (wt.%) = 1:3 rolling 48 h by 200 rpm
316L (particle size < 5μm)	67.9% powder 26.0% ethanol 2.9% water 3.2% PVAc	Mixing with ϕ 3 mm YSZ beads powder : beads (wt.%) = 1.3:1 rolling 16 h by 200 rpm
316L (particle size < 16 μm)	75.0% powder 20.3% ethanol 2.2% water 2.5% PVAc	Mixing with ϕ 3 mm YSZ beads powder : beads (wt.%) = 1.3:1 rolling 16 h by 200 rpm

3.2.2 Optimisation Methods

As mentioned, the suspensions made of stainless steel powders have been developed and used in the commercial products successfully (e.g. Sika R 0.5 AS by GKN) [45-47], so the characterisation work for the two suspensions 316L (particle size < 5 μm) and 316L (particle

size < 16 μm) was concentrated only on the influence of ageing on the viscosity of the suspensions.

For TiO_2 suspension, due to its fine-grained particle size and narrow particle size distribution there occurred agglomeration during the spraying process. The possible reasons were: too rapid evaporation rate of the solvent and not well dispersed powder agglomerates. So the main purpose of the optimisation for TiO_2 suspension was involved in how to decrease the evaporation speed of the suspension and improve the homogeneity of the suspension.

Lowering the Evaporation Rate of the TiO_2 Suspension

In order to decrease the evaporation rate of the TiO_2 suspension the composition of the solvent should be optimised. The ethanol should be substituted by some substances, which vaporise slower than the pure ethanol. A couple of liquids were chosen to take this test, whose properties pertaining to evaporation are listed in Table 3-6 [121].

Table 3-6 Some characteristics of the solvents [121]

	Ethanol	Terpineol	Water	IsoPropanol
Boiling Point [°C]	78.5	220	100	82.4
Vapour Pressure [mbar]	59 (20°C)	0.24 (40°C)	23.4 (20°C)	42.5 (20°C)

The experiments were carried out in an air conditioning laboratory, in which the temperature was kept constant at 21.5°C. A piece of 85 mm × 85 mm polished stainless steel surface was used as substrate. A certain amount of liquid (200 μl for each test) was dropped onto the substrate, which was placed on a balance open to air. Then the variation of the liquid weight due to evaporation can be measured changing with the time.

Dispersing the TiO_2 Suspension by the Additive

Agglomeration of particles is caused by attractive forces which consist of hydrogen bond (bridging water), van der Waals force, Coulomb's force and physical friction between particles. With decreasing particle size, attractive forces increase, leading to enhanced agglomeration of particles [8]. The surface properties of particles in the medium affect the stabilisation of a suspension which is attributed to balance between the van der Waals attractive forces and Coulomb repulsive forces caused by adsorbed ions on the particle surfaces [70].

In general, suspensions can be dispersed by electrostatic, steric, or electrosteric stabilisation mechanisms. Electrostatic stabilisation is accomplished by generating a common surface charge on the particles. Steric stabilisation, on the other hand, is achieved by adsorption of

polymeric additives which serve to form protective colloids. Electrosteric stabilisation requires the presence of adsorbed polymer or polyelectrolyte and a significant electrical double-layer repulsion [71]. Colloidally stable ceramic suspensions can be obtained by creating a high charge density on the particle surface with results in a strong double-layer repulsion (electrostatic stabilisation), or by adsorbing polymers on the particle surfaces where the interpenetration of the polymer layers generate a repulsive force, so-called polymeric or steric stabilisation [76-78].

Z-potential and pH-value of the solution are the two most important parameters controlling electrostatic stabilisation in aqueous as well as non-aqueous media. In aqueous media, high surface charge densities, corresponding to high surface potentials, can be obtained by working far away from the point of zero charge (pH_{pzc}) of the powder. A similar approach can be used also in non-aqueous media, providing that an operational pH scale (pH^*) and thus an isoelectric point pH^*_{iep}, for the specific solvent can be defined. The ionic strength controls the ranges of the double-layer repulsion. Since low-dielectric-constant media have a low degree of electrolyte dissociation, the double-layer repulsion can be very long range resulting in a slowly decaying potential. It was shown that there should be enough ions in solution to render the potential decay around the particles steep, but there should not be such a high ion concentration that the van der Waals attraction overcomes the double layer repulsion [79-86].

The experience from the literature [71-75] show that in highly concentrated oxide suspensions, problems related to high viscosity, ageing and processing of multiphase systems can be drastically reduced by using polyelectrolytes (e.g. polyacrylic acid — PAA and polymethacrylic acid — PMAA) as dispersants or deflocculants. Similarly, the same function can be performed by adding acetic acid (HAc), HCl or citric acid into the suspensions [77, 78]. The zeta (ζ)-potential, which is an electrical potential at the slip (shear) plane between particles and medium, is an important guide to those interfacial properties. As the double-layer potential decays slowly in nonaqueous media, the particle surface potential and zeta-potential are approximately equal [69-78].

Referencing the above literature review an attempt to improve the quality of the TiO_2 suspension was done in two steps, one is decreasing the evaporation rate of the solvent by the addition of terpineol; the other is dispersing the suspension by the addition of acetic acid. By means of zeta-potential, pH-value, viscosity and particle-size measurements the ageing test of the suspension was implemented. By varying the milling duration of the suspension an optimised milling time was decreased.

3.3 Wet Powder Spraying (WPS) Process

3.3.1 Introduction of the Process

The Wet Powder Spraying (WPS) technology was developed and patented for the production of functional ceramic and metallic layers in the institute IWV-1, FZJ [128, 129] and proved to be also a promising method to produce porous structures [65-67]. The suspension, consisting of a powder-carrier-binder mixture, is sprayed onto a substrate using a modified spraying gun. The gun is mounted on a two-axis manipulating system which allows a meandering line movement in the case of flat surfaces, whereas a cylindrical substrate can be coated by using a rotating axis. Fig. 3-3 shows a schematic diagram of this method.

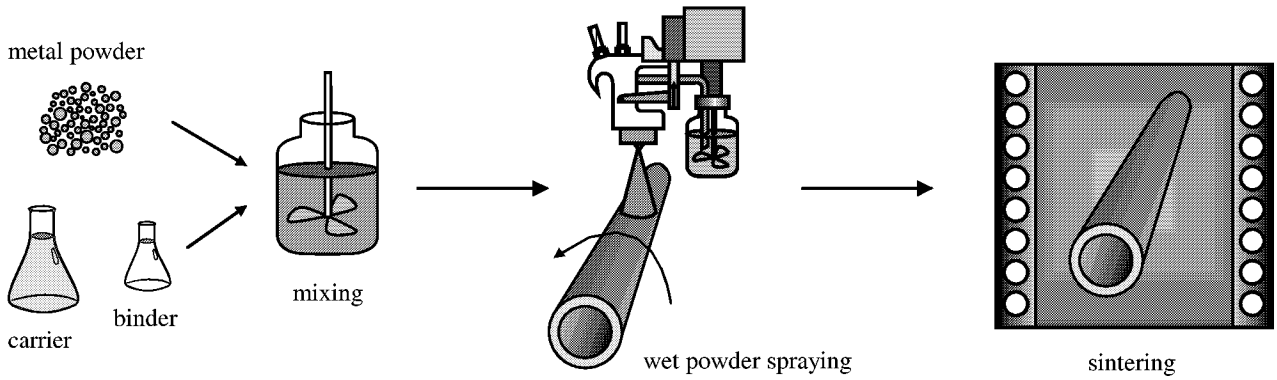

Fig. 3-3. Schematic diagram of the wet powder spraying method

The key parameters of the spraying process are the nozzle size of the gun, the distance between the nozzle tip and the substrate, the breadth of the spraying beam, the feed rate of the suspension, the operating pressure and the operating speed of the manipulating system. For planar coating the flow rate of suspensions, the operating speed and pressure exert the main influence on the thickness of the layer. Multilayer-spraying is one way to obtain layers of a well defined thickness. In case of tubular coating the rotation speed of tubular specimens is also a very important parameter, which combines the aforementioned three parameters, determining the layer thickness of tubular specimens.

After drying in a dust-free hood the samples can be sintered. Due to the small binder amount of the coatings (normally < 3 wt.%) a combined debindering and sintering cycle can be carried out.

3.3.2 Function of the Spraying Gun

The schematic diagram and the photograph of DeVilbiss spraying gun JGV 563 are shown in Fig. 3-4 a.) and b.). The air and the suspension are separately marked as blue and red colour in the diagram. The assembled spraying gun and the suspension container are photographed in Fig. 3-5.

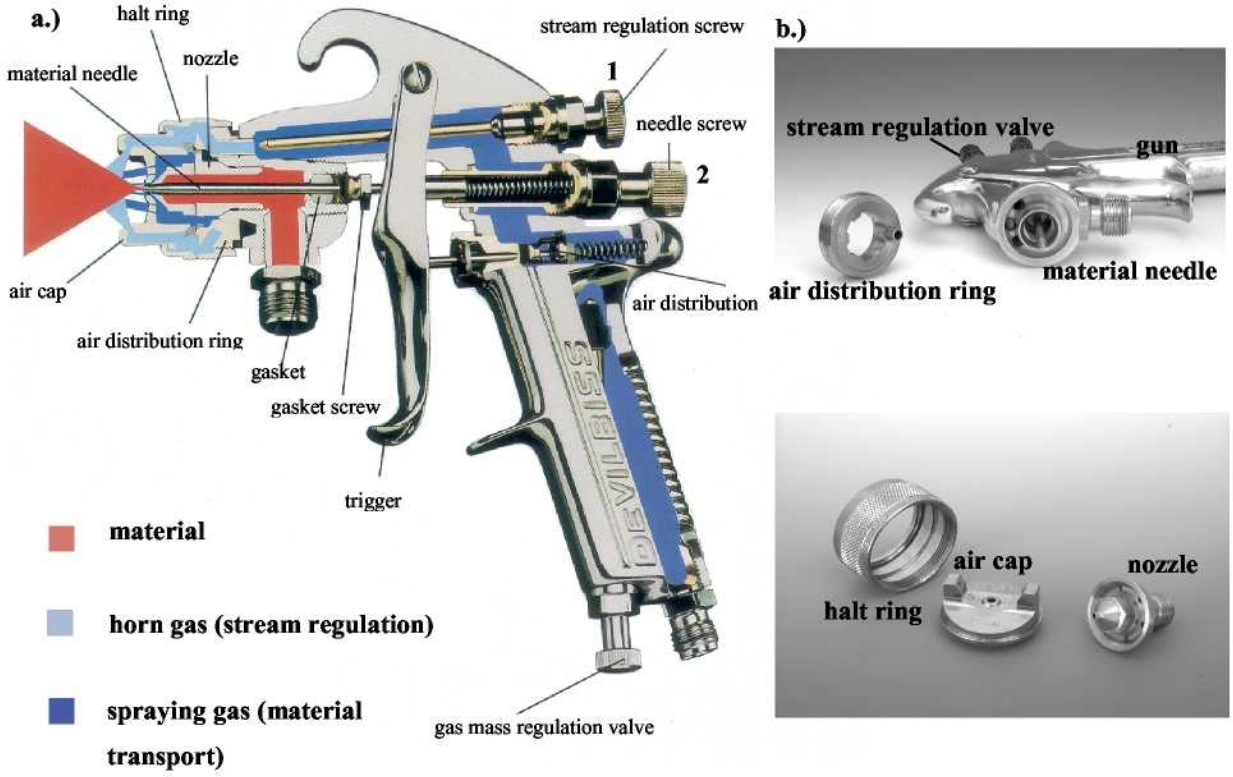

Fig. 3-4 a.) Schematic diagram of DeVilbiss spraying gun;
b.) Photograph for the elements of the spraying gun

Fig. 3-5 Photograph of the spraying gun and the suspension container

The suspension supply in the function diagram is marked with red colour, which is controlled both by the spraying pressure (acting onto the trigger) and the material-needle screw (Screw 2

in Fig. 3-4 a.)). The latter functions by adjusting the aperture between the needle and the nozzle.

The pressed air supply is marked blue in the diagram, which is divided by the air distribution ring (Fig. 3-4 b.)) into spraying gas (dark blue) and horn gas (light blue). The spraying gas flows inside the air distribution ring, through the six drilled holes of the nozzle (Fig. 3-4 b.)), to atomise the suspension from the aperture of the nozzle, also forming a conical jacket of the spraying beam shown in Fig. 3-4 a.). The spraying gas volume is adjusted by the stream regulation valve (Screw 1 in Fig. 3-4 a.)) in the cubicle of the gun (Fig. 3-4 b.)). The horn gas leaking from the air cap (Fig. 3-4 b.)) acts upon the conical spraying beam, which can be deformed from circle to ellipse. The horn gas volume is adjusted by the stream regulation valve also.

Fig. 3-6 a.) shows a schematic illustration of the spraying process; a sketch of the fine turning screw is shown on the right side, which is assemble onto the screw 1 and the screw 2 (Fig. 3-5); by turning this screw the spraying beam (screw 1) and the feed rate of suspensions (screw 2) can be controlled. An elliptical coat surface comes into being as the spraying gun keeps spraying in stillness shown in Fig 3-6 b.). By changing the spraying parameters talked above, the ellipse length and breadth can be varied. The extreme case is a circle. Fig. 3-6 c.) shows the meander moving style of the gun. Of course, the distance between the two meander lines is also an influence parameter of the spraying process.

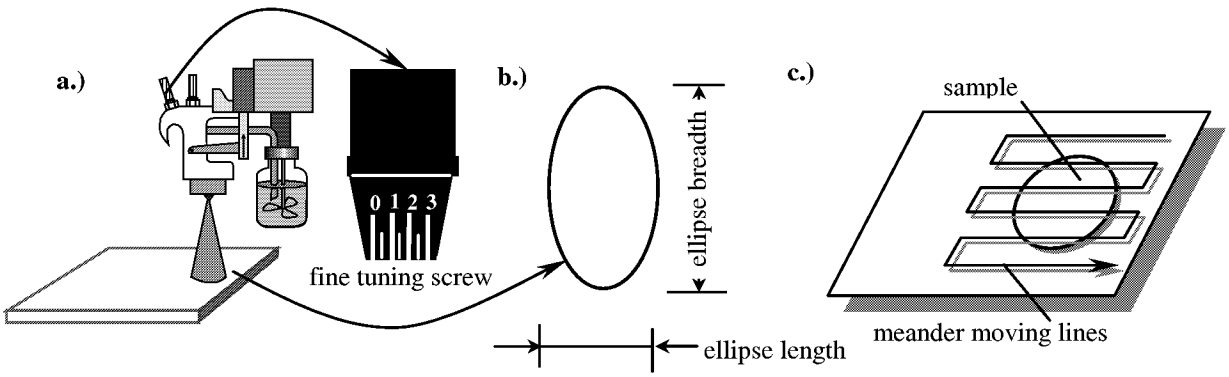

Fig. 3-6 Illustration for the spraying process,
a.) gun is spraying, by controlling the „fine tuning screw“ shown on the right side the horn gas can be adjusted; b.) a coat surface without gun's movement, normally in ellipse form; c.) meander movement of the gun

3.3.3 Optimisation Methods

As told above that the most important spraying parameters of the WPS method are the nozzle size, the spraying pressure, the spraying beam, the spraying distance between the gun and the

substrate, the feed rate of suspensions and the moving speed of the spraying gun. For the sprayed layer, the thickness is a determinative factor. So in the following attempt, the main task was to find a relationship between the spraying parameters and the thickness of the layer, i.e. the thickness distribution over the cross section of the layer. For tubular coatings the rotation speed of the samples is a predominant influence parameter.

Planar Coating

In order to avoid an unnecessary waste of the limited porous metallic substrates, the spraying experiments aiming to optimise the spraying parameters were carried out on 420×297 mm transparencies for determination of the feed rate of the suspension and layers' thickness, the others were on paperboard for illustration of the shape of the spraying beam. The reason for the adoption of transparencies is that they have uniform shape and surface, homogeneous weight distribution, and it is easy to measure the thickness of the sprayed layer onto the transparency by thickness measurement device (button method). Fig. 3-7 shows a sketch of a coat surface onto a transparency, the arrow in the diagram manifests the moving direction of the spraying gun. The length of the coat surface is defined in the program (210 mm), the breadth changes with the spraying parameters. To measure the thickness accurately the coat was sprayed only one layer. Table 3-7 shows the main spraying parameters and their abbreviations, which will be used in the context. The scale on the screw 1 (Fig. 3-5) is defined as SB and on the screw 2 (Fig. 3-5) as SA in Table 3-7. The standard parameter sets obtained from the empirical data are listed in Table 3-8.

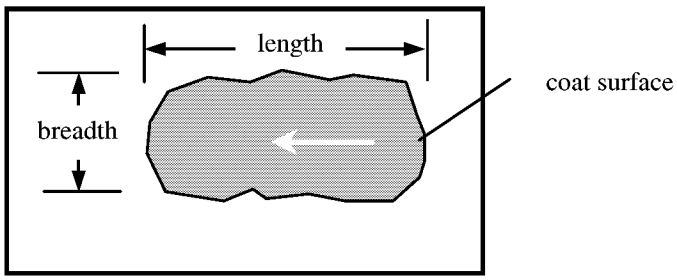

Fig. 3-7 Sketch of a coat surface

The optimisation was started by changing only one parameter shown above, the others kept constant. For example, the whole analyses began from changing the feed rate of suspensions. The experiment was planed in three steps. Firstly, to define the shape of the spraying surface, the spraying gun kept spraying for 5 seconds at different scales of the horn gas screw (screw 1 in Fig. 3-5); then one layer spraying was made to observe the trace of the suspension; at last, to define the feed rate of the suspension at each scale, the suspensions were sprayed onto

Table 3-7 Main spraying parameters and their abbreviation

Main spraying parameters/ units	Abbreviation
Nozzle size/ [mm]	N
Spraying pressure/ [bar]	P
Spraying distance/ [mm]	D
Spraying speed/ [mm/min] (velocity of the spraying gun)	V
Scale of spraying beam/ [unit] (Through changing the horn gas the shape of the coat surface is changed from circle to ellipse.)	SB
Scale of feed rate of suspensions/ [unit] (Through changing the opening of the nozzle aperture, the feed rate of suspensions is changed)	SA

Table 3-8 Standard parameter sets from the empirical data

Parameters / Suspensions	N	P	D	V	SB	SA
316L (particle size < 5 μm)	1.8	1.5	250	3500	3	13
316L (particle size < 16 μm)	1.8	1.5	250	3500	5	20

films at a fixed time (3.6s for 316L suspensions or 18s for TiO_2 suspensions) with different scales; i. e., through measuring the weight of the residues on the film, a correlation between the scale and the feed rate of the suspension can be decided. Even there existed some mass loss during the spraying, which can be neglected comparing with the residue on the film. This method can be also used to predict the other parameters listed in Table 3-7.

As talked above the thickness is a key factor for the sprayed layer, how to obtain an accurate value of the thickness proves very important. The middle lines in the breadth and length direction are measured, which represent the thickness distribution of the coat surface shown in Fig. 3-8. The whole optimisation was concentrated on how to obtain a defined layer thickness by changing the aforementioned spraying parameters.

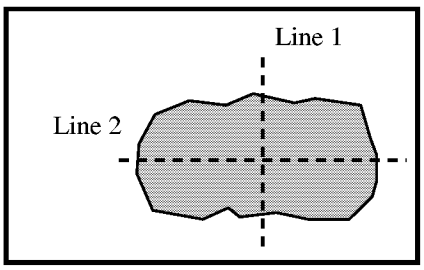

Fig. 3-8 Two measuring lines on a sprayed surface in the breadth and length directions

Tubular Coating

For coating the tubular substrates, except that the dominant spraying parameters were defined similar to the planar substrates, the rotation speed of the tubes is an other key factor in this case. If the rotation speed is too slow and not matched with the moving speed of the spraying gun, the suspension stripes on the tubes can be observed clearly. So for optimising such a spraying process, the stripe is an important indicator to judge if a good layer has been obtained or not. Fig. 3-9 shows a sketch for a rotating tube. The fine slope lines represent stripes. The moving speed of the spraying gun is defined as ‚V_G' [mm/min] and the rotation speed is ‚ϖ_R' [1/min]. The distance between two stripes is marked as ‚s' [mm]. Then we have:

The time (t) of one rotation of the tube should be: $t = 1/\omega_R$ (3.3.1)

The stripe distance (s) decided by the moving speed of the spraying gun: $s = V_G \cdot t$ (3.3.2)

Combining (3.3.1) and (3.3.2): $s = V_G/\omega_R$ (3.3.3)

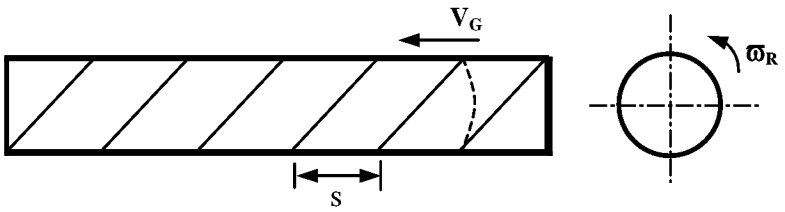

Fig. 3-9 Sketch for coating a tube

It means that the distance of stripes can be decided by the rotation speed of tubes and the moving speed of the spraying gun. Fig. 3-10 shows a coat surface of TiO_2 suspension onto paperboard, whose spraying parameters are listed under the picture.

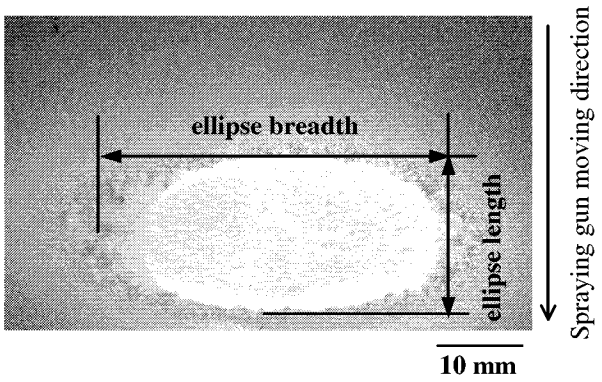

Fig. 3-10 Photograph of a coat surface sprayed by the TiO_2 suspension
The spraying parameters are: Nozzle = 1.8 mm, Pressure = 0.5 bar, Spraying distance = 230 mm, Scale of spraying beam = 5 unit, Scale of the feed rate of suspension = 7 unit, 5 seconds spraying without gun's movement

How the stripes come into being, it is explained in Fig. 3-11 a.) and b.) clearly. The ellipse length (Fig. 3-10) of the spraying surface is defined as "*W*".

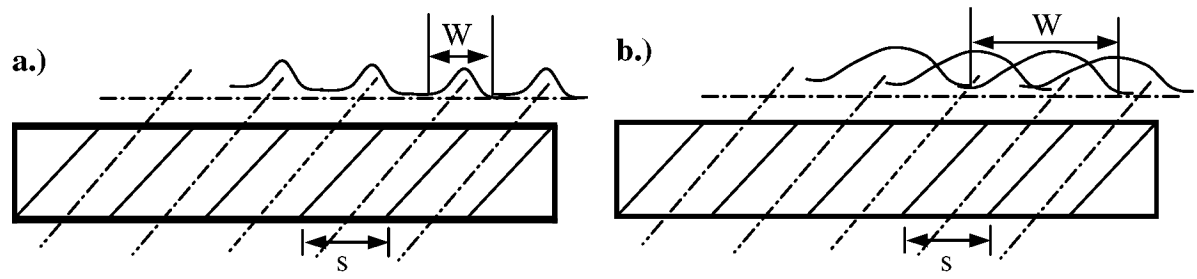

Fig. 3-11 Relationship between the spraying beam and the stripe distance

If $W < s$, then the sprayed layer is stretched and distributed as that shown in Fig. 3-11 a.), i.e. the stripes emerge onto tubes. If $W > s$, then the summits of the sprayed layer overlaps with each other, there exists no obvious boundary of the stripes onto the substrates, shown in Fig. 3-11 b.). It manifests that the spraying surfaces overlap with each other; the stripes, caused by the existence of uncoated substrate area, can not be seen anymore. If a quite thick layer is preferred, then the condition $W >> s$ should be fulfilled, for the overlapping contributes to that; if a very thin layer is required, the difference between W and s should be small enough, the ideal situation is $W = s$.

Basing on the above analysis for tubular coating, the parameter set should obey the following rule — the rotation speed of the tubes and the spraying speed of the gun should match with each other.

The thickness optimisation for the tubular samples should be done also and can only be implemented by metallographical method; it is unlike that of planar coatings and can not be carried out onto transparencies.

3.4 Sintering

The pore size distribution of the porous medium is decided by two factors: the particle size distribution of the starting powder and the sintering process. To fabricate porous materials with high open porosity, the sintering mechanisms without densification are important, i.e. surface diffusion and evaporation — condensation result in neck growth without densification. As a result, porous materials sintered by these mechanisms can have sufficient mechanical strength based on well grown necks with relatively high open porosity, which have higher fluid permeability than those with poorly grown necks. This phenomenon is due to the deviation in pore shape. Pores with well grown necks are more spherical in shape and are lower in friction of fluid flow than those with poorly grown necks. Thus, the sintering mechanism influences pore geometry, as well as porosity [8].

3.4.1 Optimisation of the Sintering Temperatures

The samples coated with TiO_2 layer were sintered by different temperature from 800°C to 950°C in vacuum for holding time of 1 hour. Heating up and cooling down rates in vacuum sintering was 5 K/min. A temperature profile is shown in Fig. 3-12.

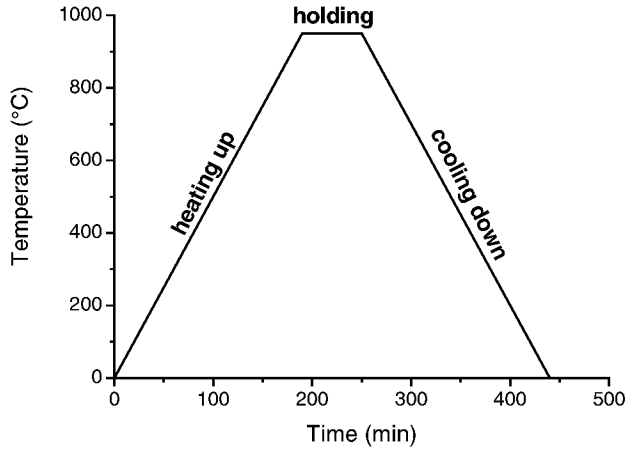

Fig. 3-12 A temperature profile of the sintering process for TiO_2 layer

The 316L stainless steel layers of particle size < 16 μm and of particle size < 5 μm were sintered also in vacuum and the heating rates keeps 5 K/min similarly. The sintering temperatures were chosen to 800°C, 850°C, 900°C and 1000°C for the 316L layer (particle size < 5 μm). Analogically the interlayer of 316L (particle size < 16 μm) was sintered by

800°C, 900°C and 1000°C separately. The referencing sintering conditions in GKN of these two powders were in vacuum by 1060°C, 3h and 925°C, 3h separately.

SEM images were adopted here to observe if there formed sintering necks between particles or the particles were over-sintered and to evaluate the optimal sintering temperature easily.

3.4.2 Cofiring

Referencing the work of Lenk etc. [86] a „cofiring" process was adopted into the experiment. That means, the applied layer is coated onto the green body of the support layer, then after drying these two layers are sintered together.

As shown in Fig. 3-13, two experimental routes were tried, one is the cofiring between the 316L of particle size < 5μm steel powder and the TiO_2 powder, the other is the cofiring between the 316L of particle size < 16μm and the 316L of particle size < 5μm steel powders.

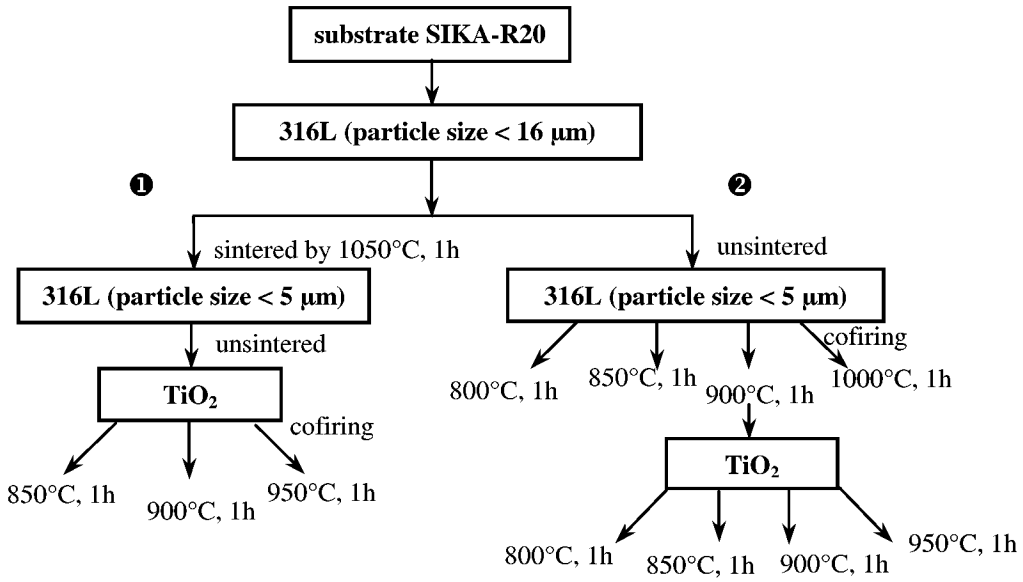

Fig. 3-13 A scheme for optimising the cofiring process and the sintering temperature of different layers

3.5 Characterisation Methods

Characterisation methods for the whole work are mainly divided into following several groups due to different purposes — a.) characterisation of applied particles and suspensions; b.) characterisation of microstructural features for filter membranes; c.) characterisation of permeability of filter membranes; d.) characterisation of mechanical strength and chemical resistance for filter membranes.

Viscosity Measurement

Viscosity is a very important parameter for the suspensions used in the WPS method. The high viscosity of suspensions leads to a blockage of the nozzle and imperfections onto the

sprayed layer surface. Viscosity was measured by rotation-viscosimeter (Viscolab-Rheometer, HAAKE, Germany) by the rotation speed of 0~350 rpm. An estimation of the average value was made in the range of 200~350 rpm.

Zeta-Potential and pH Value Measurement

As told above, zeta-potential and pH value were measured to characterise the dispersing ability of the dispersant used to stabilise the TiO_2 suspension. The applied installation is DT1200 (Dispersion Technology, USA).

Particle Size and Specific Surface Area Measurement

Particle size distribution of starting powders has a dominant influence on the micro pore structure of porous media. There are several installations used in IWV-1: Laser Partikel Sizer (Fritsch, Analysette 22®, Germany) and UPA equipment (Ultrafine Particle Analyzer, Grimm, Germany). The latter is suitable for very fine particles and was used to trace the agglomerates in the TiO_2 suspension.

Combining the particle size with specific surface area measurement an optimisation for milling duration of the TiO_2 suspension was done. The latter is based BET method (Braunauer-Emmett-Teller) and DIN 66 131f done by AREA-Meter II (Ströhlein Instruments, Germany).

SEM, LM and XRD

Microstructure of particles, sintered coating surface and fractured surface of filter membranes were measured by scanning electron microscope (Joel JSM T300 and LEO 1530 – Gemini).

All cross section structure of filtermembranes was measured by Light Microscope (Olympus PMG3, Germany), by which the thickness of different layers can be decided.

In order to detect the reaction between TiO_2 layer and 316L SS substrate a phase analysis was made by X-ray diffraction (XRD, D5000, Siemens).

Surface Roughness Measurement

As talked in the section 2.2, the quality of support layers has a fateful influence on the applied layer. Roughness measurement was taken as a means to inspect the surface homogeneity, which was done by Surface Laser Profilometer (Polaris Cor.).

Bubble-Point Test and Pore Size Distribution

The „Bubble-Point Test“, also referred as „gas bubble test“, provides a simple method of determining the size of the apparently „largest“ pore. The porous element to be tested is immersed in a liquid with a low surface tension (usually alcohol). Following this, pressurised air is applied to one side of the sample and the air pressure increased until the first bubble appears. This pressure is called the „Bubble-Point“ pressure. Fig. 3-14 shows the process

clearly. Under the assumptions that the surface tension and the pressure difference required can open the first pore and the pore shape is an ideal cylinder, the „apparently" largest pore can be calculated according to the equation 3.5.1.

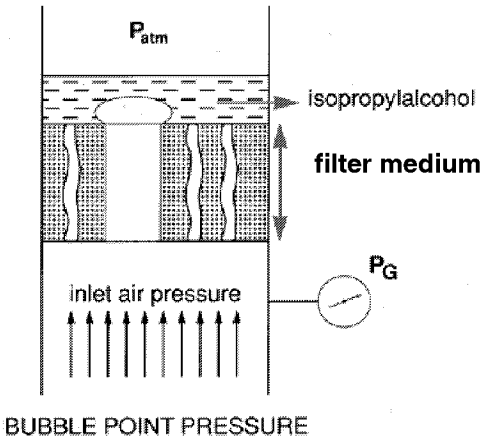

Fig. 3-14 Principle of Bubble-Point Test

$$d_x = \frac{4 \cdot \sigma \cdot \cos\varphi}{\Delta P_x} \qquad (3.5.1)$$

where d_x — „apparent" pore diameter [m]

σ — surface tention [N/m]

φ — wetting angle [°]

ΔP_x — pressure drop at the filter [Pa]

The diameter d_x relates to a circular pore, whose circumference equals to that of the real irregularly shaped pore. Of course, a pore size spectrum is measured during the test, which is determined using an automated measuring instrument (Coulter Porometer, USA) based on „Bubble-Point" principle (ASTM E 1294).

Due to the relation between the pores and the bubble pressure, the „Bubble-Point" test can also be used to detect the imperfections (e.g. pinholes and cracks) in the functional layer, which lead to bubble emerging at quite low pressure drops.

Permeability

The permeability is a very important characteristic of filter membranes. The flow rate is a symbol to evaluate the permeability of a filter medium, which is dependent on the applied differential pressure. Measurement of the flow rate, usually using air or water, can be made according to DIN ISO 4022. Fig. 3-15 shows a measurement diagram of flow rate, the calculation formula is listed on the right side.

In our case, after the probes were produced, they were sent to the company GKN to take the tests of the pore size distribution and the flow rate. Normally water and air are chosen as the flow media. The pressure difference lies in the range of less than 600 mbar.

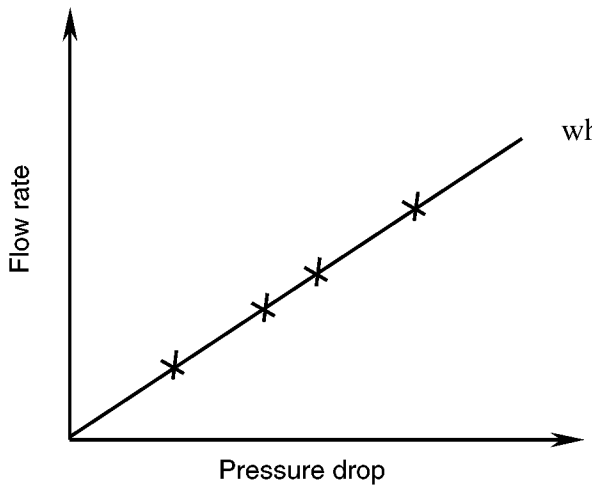

Fig. 3-15 Diagram for flow rate measurement

$$\Delta P = \frac{\dot{Q} \cdot L}{A}\left(\frac{\mu}{\alpha} + \frac{\rho \cdot \dot{Q}}{\beta \cdot A}\right) \qquad (3.5.2)$$

where ΔP — pressure drop [Pa]

$\dot{Q}$ — flow rate [m^3/s]

L — thickness of samples [m]

α — laminar coefficient [m^2]

β — inertial coefficient [m]

A — surface area of samples [m^2]

ρ — density of flow medium [kg/m^3]

μ — viscosity of flow medium [Pas]

Stability Test

In order to check the mechanical stability of the samples a test was made as shown in Fig. 3-16.

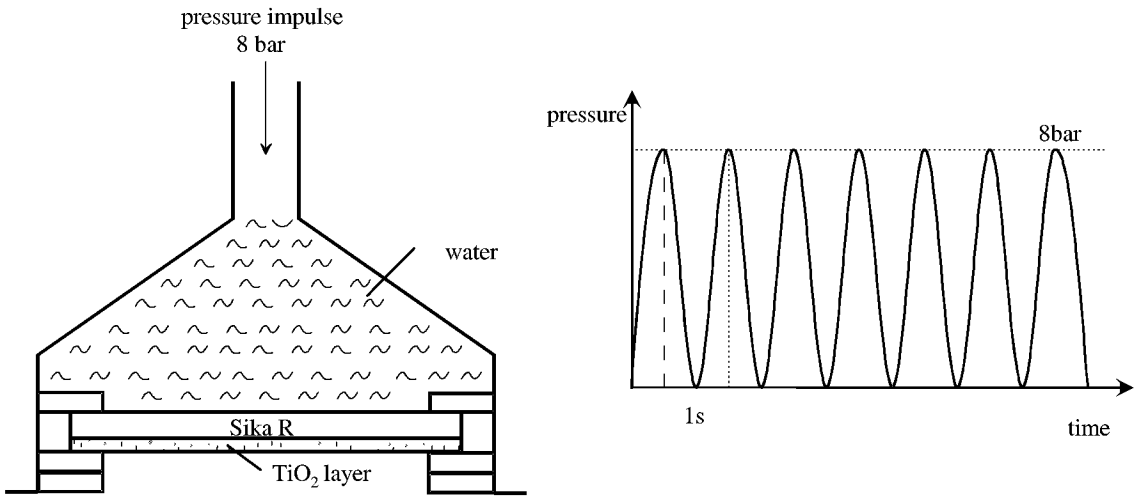

Fig. 3-16 Schematic illustration of stability test

Samples were fixed by a clamp device. The pressure brought on by water exerted on the support side of samples periodically. The peak value of the pressure is 8 bar and one cycle interval is approximate 1 s. The samples underwent as far as 1 million cycles in the test.

Steam Sterilisation

In order to test if filter membranes can endure a harsh working environment, especially for the beverage and wine filtration application, a steam sterilisation test was done. Samples were wrapped with aluminium foil and put in an autoclave, heated up from ambient temperature to

120°C, holding 20 min, cooled down at the same rate 5 K/min, then the samples were kept in a drying chamber. This cycle was repeated 10 times and samples were characterised by SEM.

3.6 Simulation of the filtration process

3.6.1 Original Thought

For a rational system design, it is essential to have as much detailed knowledge of transport and separation mechanisms as possible to maximise the flux across the filter membrane. Furthermore, the permeability is also an important parameter to guide the manufacture of the filter membranes.

Permeability is the term used for the conductivity of the porous medium with respect to permeation by a Newtonian fluid. Its value is uniquely determined by the pore structure. A practical unit of permeability is the darcy. A porous material has permeability equal to 1 darcy if a pressure difference of 1 atm (1.013×10^5 Pa) will produce a flow rate of 1 cm^3/s (10^{-6} m^3/s) of a fluid with 1 cP (10^{-3} Pa·s) viscosity through a cube have sides 1 cm (10^{-2} m) in length. Thus,

$$1\ darcy = \frac{10^{-6}(m^3/s)\cdot 10^{-3}(Pa\cdot s)\cdot 10^{-2}m}{10^{-4}(m^2)\cdot 1.013\times10^5 Pa} \tag{3.6.1}$$

is equal to 0.987×10^{-12} m^2 [87].

The permeability k is defined by Darcy's law. In sufficiently slow, unidimensional, steady flow:

$$\dot{Q} = \frac{kA}{\mu}\cdot\frac{\Delta P}{L} \tag{3.6.2}$$

This is a linear law, similar to Newton's law of viscosity, Ohm's law of electricity, Fourier's law of heat conduction, and Fick's law of diffusion. In the Eq. (3.6.2), $\dot{Q}$ is the volumetric flow rate, A is the normal cross-sectional area of the sample, L is the length of the sample in the macroscopic flow direction, $\Delta P \equiv P_1 - P_2$ the hydrostatic pressure drop, and μ is the viscosity of the fluid.

The flow rate measurement is an important method to characterise the filter membrane. Fig. 3-17 shows the flow rate measurement results from GKN catalog.

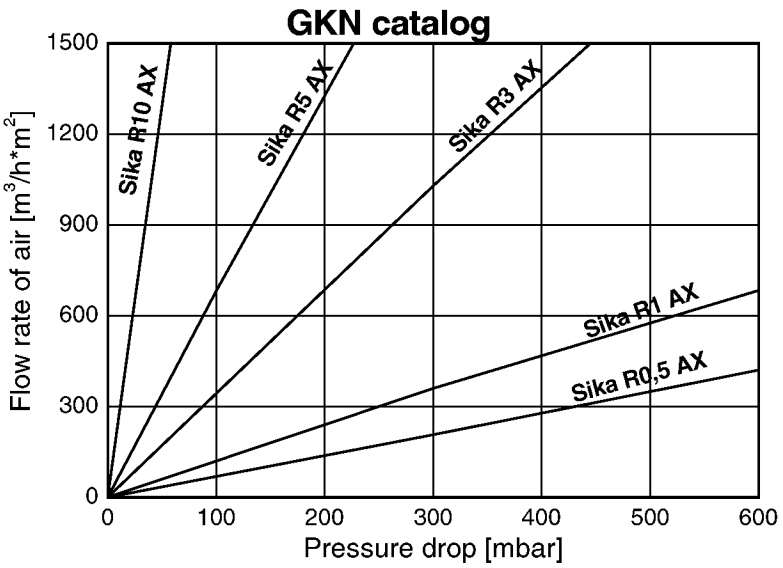

Fig. 3-17 Flow rate results of different products from GKN catalog

In principle, measurement at a single steady flow rate permits calculation of the permeability from Darcy's law; however, there is usually considerable experimental error caused by the experimental equipment in these measurements, and it is both advisable and customary to perform measurements at various low flow rates, plot the flow rates versus the pressure drop, and match a straight line to the data points. According to Darcy's law, this line must pass through the origin. The scatter of the data points might sometimes cause the best-fitting straight line not to pass through the origin, however. If the data points cannot be fitted with a straight line, then Darcy's law is not being obeyed and the system needs to be investigated to find the cause of the deviation [87]. It is obvious in the Fig. 3-17 that the flow-rate measurement results of the specimens satisfy the requirement of Darcy's law, the flow is steady and laminar at quite low pressure drop. So an analytical solution can be drawn by applying Darcy's law to calculate the flow rate of the graded filter structure.

In this work a mathematical model was built up to simulate the flow process of a graded filter structure and predict the flow rate of it with the help of Darcy's law and the pore structure of the filter membrane. Then the model can offer a beneficial data bank for the graded porous structure, which leads to a better understanding of this structure and a guidance of the manufacture process.

3.6.2 Literature Review

As talked to mathematical models in simulating the permeability of porous media, Dullien [59, 87] overviewed many different modelling approaches for the treatment of single-phase flow and categorised them according to his own experience in this field. Of course, each approach has a certain validity, and the better the various models will be reconciled with each other, the more adequate our understanding of flow through porous media will become.

Referencing the category method of Dullien and combining the application range of Darcy's law, the models for single-phase flow can be categorised in the following several different ways. Due to the special characteristics of gases in porous media the flow models of gases distinguish from those of liquids.

Permeability models based on conduit flow

The flow of a fluid in many porous media can be imaged with equal justification to occur either in a network of closed conduits or around solid particles forming a spatial array. The simplest approaches based on the idea of conduit flow do not pay any attention to the fact that different pores are interconnected with each other, which are called „capillaric permeability models" by Dullien. All „capillaric" models are inherently one-dimensional. Fig. 3-18 illustrates how the conduit is defined.

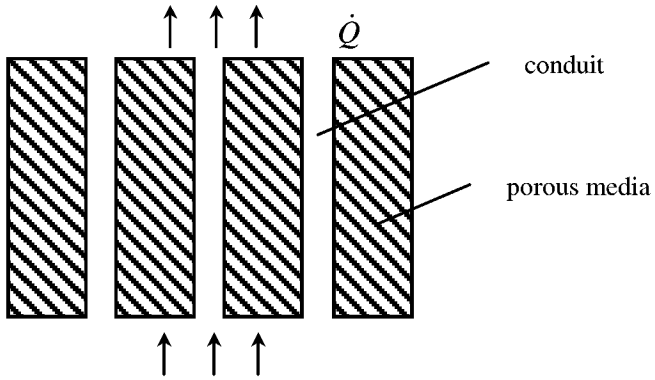

Fig. 3-18 Illustration of the physical meaning of conduit flow

Among the different capillary permeability models the so-called Carman-Kozeny model enjoys much greater popularity than the others, which is often called the „hydraulic radius theory". In this theory [88-91] the porous medium was assumed to be equivalent to a conduit, the cross section of which has an extremely complicated shape but, on the average, a constant area. For low and intermediate porosity the conduit flow approach is quite appropriate.

The Carman-Kozeny theory is aimed at laminar flow, whereas the hydraulic radius concept is known in hydraulics to be a good approximation of reality. In analogy with the established

practice in hydraulics, the channel diameter D_H governing the flow rate through the conduit was assumed to be four times the hydraulic radius, defined as the flow cross-sectional area divided by the wetted perimeter, that is:

$$D_H = \frac{4 \times void\ volume\ of\ medium}{surface\ area\ of\ channels\ in\ medium} \tag{3.6.3}$$

A Hagen-Poiseuille type equation is assumed to give the average pore, interstitial, or seepage velocity v_p in the flow channels:

$$v_p = \frac{\Delta p}{L_e} \cdot \frac{D_H^2}{16 k_0 \mu} \tag{3.6.4}$$

where L_e is the average path length of flow and k_0 is a „shape factor", which was found to lie between 2.0 and 3.0, as suggested originally by Carman. The pore velocity v_p and the fluid velocity v in Darcy's law:

$$v = \frac{k}{\mu} \cdot \frac{\Delta p}{L} \tag{3.6.5}$$

are assumed to be related as follows:

$$v_p = \frac{v}{\phi} \cdot \frac{L_e}{L} = v_{DF} \cdot \frac{L_e}{L} \tag{3.6.6}$$

The $v_{DF} \equiv v/\phi$ is the average pore velocity defined by the „Dupuit-Forchheimer assumption", which is very often used to define an average interstitial velocity (ϕ is the porosity). The multiplication of v by L_e/L in Eq. (3.6.6) is due to Carman. It corrects for the fact that a hypothetical fluid particle used in the macroscopic flow equations and flowing with velocity v covers a path length L in the same time as an actual fluid particle, flowing with velocity v_p, covers an average effective path length L_e, as illustrated schematically in Fig. 3-19. From this picture, the concept of the effective length can be understood easily.

A supposed flow path is shown in the picture (Fig. 3-19). It is assumed that the volume flow rate $\dot{Q}$ keeps the same both for the two different case (Fig. 3-18 and Fig. 3-19). The porosity ϕ of the porous medium can be calculated as that listed on the right side. Then a relation between the pore velocity v_p and the fluid velocity v in Darcy's law can be obtained.

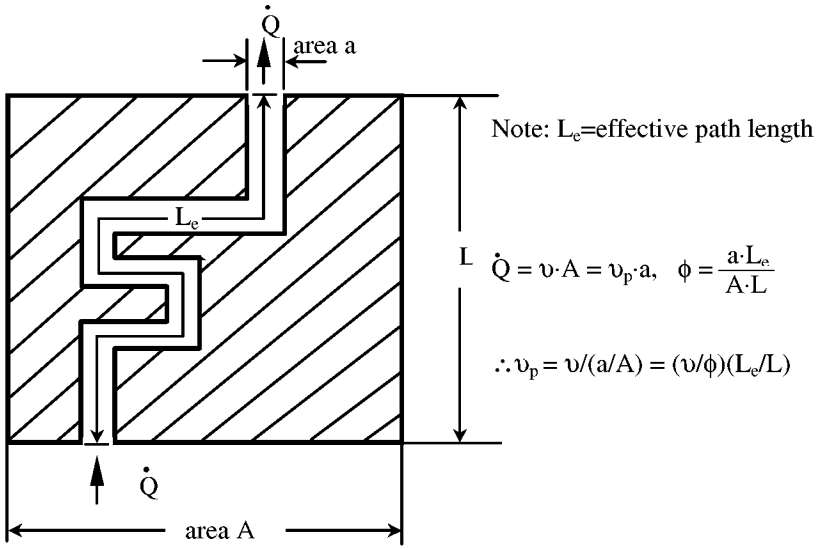

Fig. 3-19 Illustration of the physical meaning of Eq. (3.6.6) [59]

Unfortunately, the accurate value of L_e is seldom, if ever, known and, therefore, the true value of υ_p is also uncertain in most porous media. Combination of the preceding three Eqs. (3.6.4) – (3.6.6) gives the permeability k_{CK} (Carman-Kozeny):

$$k_{CK} = \frac{\phi\, D_H^2}{16 k_0 (L_e / L)^2} \tag{3.6.7}$$

This is the basic form of all capillaric models, differing only in the method of calculating the mean square diameter and in the value used for $k_0(L_e/L)^2$, which is a function of pore geometry.

The „hydraulic diameter“ can be also expressed as follows (equal to Eq. (3.6.3)):

$$D_H = \frac{4\phi}{S_0(1-\phi)} \tag{3.6.8}$$

where S_0 is the specific surface area based on the solid's volume. By combining Eqs. (3.6.7) and (3.6.8), the usual form of the Carman-Kozeny equation for permeability is obtained:

$$k_{CK} = \frac{\phi^3}{k_0 (L_e / L)^2 (1-\phi)^2 S_0^2} \tag{3.6.9}$$

where $(L_e/L)^2$ is usually called hydraulic „tortuosity factor“ (γ). According to Carman, the best value of the combined factor $k'=k_0(L_e/L)^2$ to fit most experimental data on packed beds is equal to 5, where k' is the so-called Kozeny constant.

In the case of nonspherical particles the surface average equivalent sphere diameter is defined as:

$$\overline{D}_{p2} \equiv \frac{6V_p}{S_p} \tag{3.6.10}$$

where V_p / S_P is the volume-to-surface ratio of the particulate system.

Defining the mean particle diameter $\overline{D}_{p2}$ as the diameter of the hypothetical sphere with the same S_0 as the particles, that is:

$$\overline{D}_{p2} \equiv \frac{6}{S_0} \tag{3.6.11}$$

Then the following equation can be obtained immediately (Kozeny constant $k'=5$ is considered):

$$k_{CK} = \frac{\overline{D}_{p2}^2}{180} \cdot \frac{\phi^3}{(1-\phi)^2} \tag{3.6.12}$$

The hydraulic „tortuosity factor“ $\gamma \equiv (L_e / L)^2$ is not a property of the porous medium, but it is a parameter of the one-dimensional model of the medium. As illustrated schematically in Fig. 3-20, if the sample length in the direction of macroscopic flow is L, the porosity of the

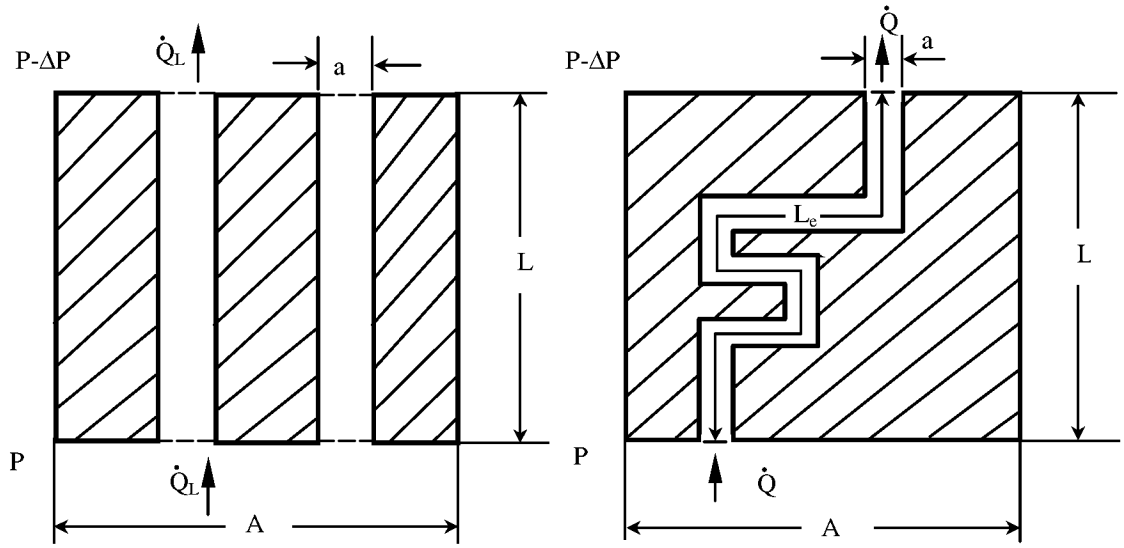

$$\dot{Q}_L = 2a(\Delta P / L)(D_H^2 / (16k_0\mu)) = \phi A(\Delta P / L)(D_H^2 / (16k_0\mu))$$

$\phi=2a/A$; $L_e=2L$

$$\dot{Q}_{L_e} = a(\Delta P / L_e)(D_H^2 / (16k_0\mu) = (\phi A / 2)(\Delta P / L_e)(D_H^2 / (16k_0\mu) = (a / 2)(\Delta P / L)(D_H^2 / (16k_0\mu)$$

$$\dot{Q}_L / \dot{Q}_{L_e} = (L_e / L)^2 = \gamma = 4$$

Fig. 3-20 Illustration of the physical meaning of the „tortuosity factor“ [59]

For the given geometrical set-up the tortuosity factor is $\gamma=4$.

sample is ϕ, the pressure drop is ΔP and the flow rate is $\dot{Q}$, the capillaric model consists of tubes of length L whereas the effective length of pores in the medium is $L_e > L$. Therefore, in the medium the pore velocity for the given ΔP is (L/L_e) times less, and also number of pores in parallel is (L/L_e) times less because the model's porosity must match ϕ (the porosity of the medium). As a result, a tube length L_e gives, for the same values of ϕ, L and ΔP, $(L/L_e)^2$ times lower flow rate.

It is important to mention that the very concept of γ is limited to one-dimensional models because the tortuousness of the pore network is intrinsically incorporated into three-dimensional models.

The Carman-Kozeny equation is of approximate validity. It has been found particularly useful for measuring surface areas of some powders. In the case of particles that deviate strongly from the spherical shape, broad particle size distributions, and consolidated media, the Carman-Kozeny equation is often not valid. The frequent claim that the main reason for disagreement between permeabilities predicted by the Carman-Kozeny equation and experimental values lies in high sample tortuosities is unfounded.

Within the conduit flow approach, many modifications to the Carman-Kozeny model have been done, for example, bundle of capillary tubes models tried to change the parallel channel diameters distribution, also in serial-type capillaric models each channel was assumed to consist of segments of different diameters distributed according to volume-based pore size distribution [93, 94]. In the statistical model, based upon the calculation of the probability of occurrence of sequences of pairs of pores of all the possible sizes, and of the contribution to the permeability made by each such pair, leads to an expression of the permeability as the sum of a series of terms, in which the random nature of the interconnect and orientation of the pores has been emphasised [94-98].

Phenomenological flow models

Empiricism, often aided by dimensional analysis and theoretical considerations, is one way of approaching the problem. The correlation obtained as a result of such procedures is called „phenomenological models“ [87]. This approach is independent of considerations pertaining either to conduit flow or to flow around submerged objects. Fig. 3-21 shows a diagram to understand the physical meaning of this method.

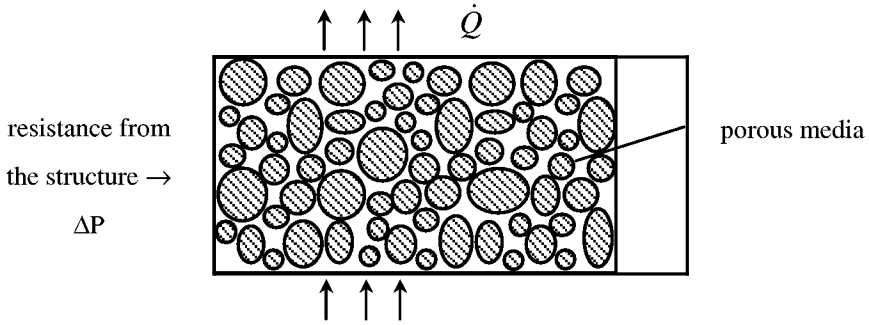

Fig. 3-21 A porous media packing

According to the analysis of Rumpf and Gupte [99], there is the following relationship among the dimensionless parameters:

$$\frac{\Delta P}{\rho v^2} = f(v\overline{D}_p/\nu,\ L/\overline{D}_p,\ \phi,\ q_i,\ \psi_i,\ structure) \tag{3.6.13}$$

where ΔP is the pressure drop over the distance L, ρ is the density of the fluid, ν is the kinetic viscosity, ϕ is the bulk porosity, q_i are the particle size distribution parameters, and ψ_i are the particle shape parameters. The various parameters that characterise particle shape and packing structure may be very difficult to evaluate in the general case. The complications may even become insurmountable if there are several very different particle shapes present in the pack. Neglected in the dimensional analysis were the compressibility or expandability of the pack, the effects of interfacial energy, suspended matter, dissolved gases, and, in the case of gaseous flow, the mean free path of the molecules. They studied the special case of random packs consisting of various distributions of spherical particles over the relatively wide range of porosity ($0.35 \le \phi \le 0.7$), and the range of Reynolds numbers ($10^{-2} \le Re_p \le 10^2$). A narrow distribution extending over a range of particle diameters, $D_{pmax}/D_{pmin} \approx 7$ were tested by them. Rumpf and Gupte [99] got a relation of the friction parameter multiplying porosity function for the uniformly random bead packs and Reynolds number:

$$f_p = K(5.6/\mathrm{Re}_p)\cdot\phi^{-5.5} \tag{3.6.14}$$

with K=1.00 and 1.05 for the narrow distribution and the too wider distributions, respectively. It is important to realise that an empirical relationship of the form

$$f_p = const/\mathrm{Re}_p \tag{3.6.15}$$

implies Darcy's law with

$$k = \overline{D}_p^2/const \tag{3.6.16}$$

The relationship of Eq. (3.6.14) found by Rumpf and Gupte [99] becomes, after introducing the definitions of f_p and Re_p,

$$\frac{\Delta P}{L}\cdot\frac{1}{\mu\upsilon}=\frac{5.6K\phi^{-5.5}}{\overline{D}_{p2}^{2}} \tag{3.6.17}$$

where $\overline{D}_{p2}$ is surface average sphere diameter; on comparison with Darcy's law, results in the following expression for the permeability:

$$k=\frac{\overline{D}_{p2}^{2}\phi^{5.5}}{5.6K} \tag{3.6.18}$$

Rumpf and Gupte [99] compared the fits obtained by their data when using their model with that so-called Blake-Kozeny equation [100] and showed the advantage of theirs.

It was pointed out by Scheidegger [101] that for various porous media the value of the Reynolds number above which Darcy's law is no longer valid has been found to range between 0.1 and 75. The transition from the linear portion (range of validity of Darcy's law) to the non-linear one is gradual. At flow rates outside the range of validity of Darcy's law, the two best known relationships are the Ergun equation [102] for intermediate values of Re_p and the Burke-Plummer equation [101] for higher values of Re_p.

The Ergun equation is a special form of the Forchheimer equation [103]:

$$\Delta P/L=\alpha\mu\upsilon+\beta\rho\upsilon^{2} \tag{3.6.19}$$

where ΔP and L are the same as those in Darcy's law (Eq. (3.6.2)), α is reciprocal permeability ($1/k$) and β the so-called inertia parameter, μ is the fluid viscosity, υ is the fluid velocity and ρ is the fluid density, with α and β expressed in terms of pore structure parameters as follows:

$$\alpha=A\cdot\frac{(1-\phi)^{2}}{\phi^{3}\overline{D}_{p2}^{2}} \tag{3.6.20}$$

and

$$\beta=B\cdot\frac{1-\phi}{\phi^{3}\overline{D}_{p2}^{2}} \tag{3.6.21}$$

where A (180) and B (1.8 or 4) are the „constants", ϕ is the porosity of the porous structure, $\overline{D}_{p2}$ is the surface average equivalent sphere diameter in the case of nonspherical particles.

It is easy to find out that the Forchheimer equation is a modification to Darcy's law with adding an inertia term to it. The basic issue is whether the Forchheimer equation is the correct flow equation over the entire practical range of flow rates or not. There have been suggestions to add a cubic third term in the velocity [104, 105]. Many researchers [106-108] contributed

their efforts to rearrange the equation and test the form using a mass of literature data and concluded that the physical model underlying the Forchheimer equation is adequate. It has been customary in the literature to refer to a „turbulent" range whenever the inertia term in the Forchheimer equation is predominant.

Phenomenological models have proved to be particularly useful in the case of packs of fairly uniform and isometric particles or of fibres. They relate the transport coefficients of the porous media to grain or fiber properties and packing structure.

Network models

Originally, networks were studied extensively in electrical circuitry, where the „junctures" or „nodes" can be regarded as mathematical points without size or resistance. Often the networks studied for the purpose of modelling pore structure are assumed to be like electrical networks. However, in fact, the pore structure of the vast majority of porous media consists of an interconnected three-dimensional network of pores, or capillaries, which have very definite characteristic shape, size, volume and resistance. Hence, it is logical to model capillary pressure curves and other transport properties of porous media with the help of network models of the pore structure. With the help of high powered computers eventually it will be possible to calculate quasi-static capillary displacement in the sample deterministically.

One can distinguish one-, two- and three-dimensional „networks". A one-dimensional network is a chain, that is, not a network in the true sense of the word. The only difference between the bundle of capillary tubes model and a one-dimensional „network" is that the former model each tube has a uniform diameter, whereas in the latter the diameter changes along the axis of the tube in some regular or irregular manner.

A two-dimensional network is a lattice. Inspired from the work of Chartzis and Dullien [109], Koplik [110] carried out calculations on two-dimensional regular networks consisting of circular junctions (pores) centered at the intersections of straight channels (necks) and found linear relations of the Hagen-Poiseuille type between the flow rate and the pressure drop in both the pore and the neck. The following regular networks were treated: square, hexagonal, Kagomé, trigonal and crossed square, shown in Fig. 3-22.

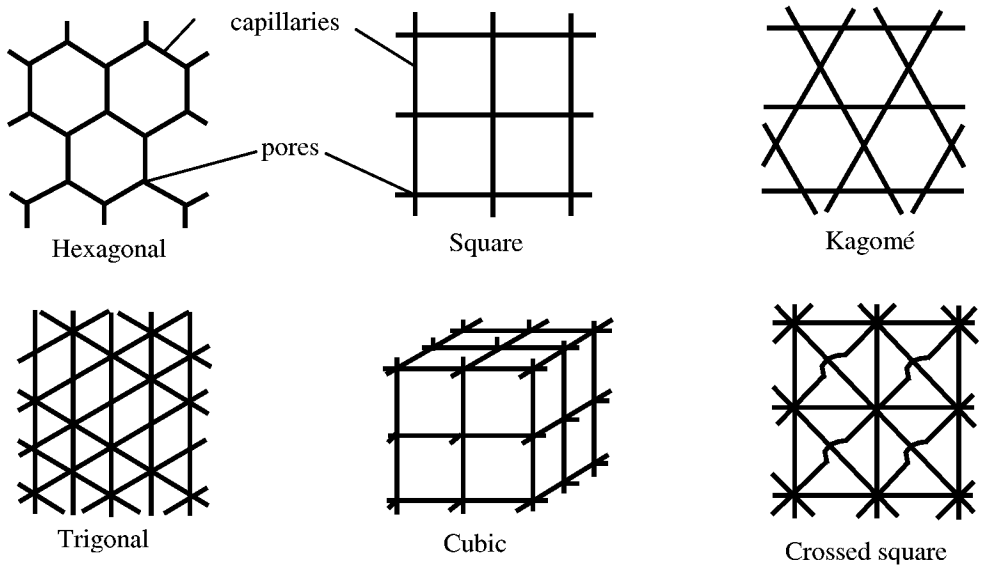

Fig.3-22 Various network models of permeability [110]

The basic difference between three-dimensional networks and two-dimensional networks lies in the point: only in three-dimensional networks it is possible to have two continuous phases present simultaneously. In two-dimensional networks only one phase can be continuous — the second phase must be discontinuous. The term „continuous phase“ or „continuum“ means that one can go from any point within that phase to any other point within the same phase without ever going outside the phase. What we concern here is only the single phase flow, so the three-dimensional system will not be discussed.

In a network of straight lines, the lines from „bonds“ meet at points, which are called „nodes“. In the present paper the words „bond“, „capillary“, „pore work“, and „pore throat“ have the same meaning. The same holds true for „sites“, „nodes“ and „pore bodies“. Calculation of the penetration of the network in a way that is independent of the density function of the sample and depends only on the type of the network considered, its dimensionality, and its co-ordination number [109] has certain advantages with respect to economy of computations.

Considering a flow process microscopically, it is a displacement process between wetting phase and nonwetting phase in the porous media. At one point when the capillary pressure P_c is surpassed, the nonwetting phase can be displaced by the wetting phase or vice versa depending on the pore necks orientation. This point is called „breakthrough“ or „threshold“ or „entry“ capillary pressure. This procedure is known as „percolation“.

A bond or a node is penetrated by the wetting fluid if both of the following conditions are fulfilled: 1.) the bond or the node is open; 2.) the bond or the node is connected to the

injection face of the sample by an uninterrupted chain of bonds and nodes that are also open (i.e., is accessible from the outside).

The detailed topology of a real porous network is extremely difficult to model. As a consequence of the resulting description for the pore space connectivity, the calculation of transport properties in such complex structures usually requires an enormous computational effort. Boston's group [111-113] adopted a regular square lattice as an implied topological representation of the system. The simulations have been performed with 50×50 networks randomly generated to produce several different prescribed porosity. Fig. 3-23 shows a typical realisation of the porous medium of their method and Fig. 3-24 shows the velocity flow field through a porous medium for a given porosity, ϕ=0.8, Re=0.01.

They investigated the origin of the deviations from the classical Darcy's law by numerical simulation of the Navier-Stokes equations in two-dimensional disordered porous media. They applied the Forchheimer equation as a phenomenological model to correlate the variations of the friction factor for different porosity and flow conditions. At sufficiently high Reynolds numbers, when inertia becomes relevant, a transition from linear to non-linear behaviour which is typical of experiments was observed.

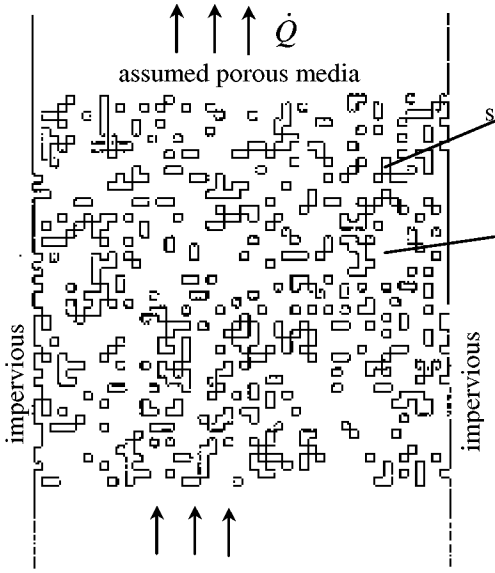

Fig. 3-23 A typical realisation of the porous medium (ϕ=0.8) [111]

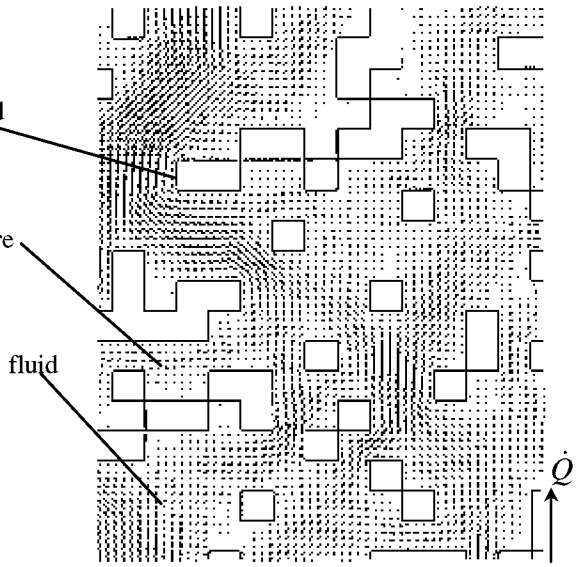

Fig. 3-24 Close up section of the plot of the velocity flow field through a porous medium at low Reynolds number (ϕ=0.8, Re=0.01) [111]

Their conclusions with the Navier-Stokes equations indicate that the Forchheimer model should be valid for low *Re* and also for a limited range of high *Re* numbers, even when inertial non-linearity can significantly affect the momentum transport at the pore scale.

Basing the Boston group's method, Wang et al. [114] drew a conclusion that Darcy's law is only correct for fluid flows in macroscopically homogeneous porous media, not for fluid flows in fractals.

Gas-flow in porous medium

The standard procedure for determining the permeability of porous media is based on the fundamental assumption that, as long as the rate of flow is proportional to the pressure gradient the permeability constant of a porous medium is a property of the medium, and is independent of the fluid used in its determination. Although this is true for most liquids, the permeability constant as determined with gases is dependent upon the nature of the gas, and is approximately a linear function of the reciprocal mean pressure. This effect can be explained by taking into account the phenomena of slip, which are related closely to the mean free path of the gas molecules [115].

Flow of gases in porous media has certain special characteristics that distinguish it from the flow of liquids, which is treated in the literature mostly together with pore diffusion. An important difference between flow of liquids and gases in porous media is that in the latter case the velocity at the solid walls cannot, in general be considered zero, but a „slip" or „drift" velocity at the wall must be taken into account. This effect becomes significant when the mean-free path of the gas molecules is of magnitude comparable to the pore size. When the mean-free path is much smaller than the pore size, the slip velocity becomes negligibly small. As in liquids the mean-free path of molecules is of the order of the molecular diameter, so the non-slip condition always applied in liquid flow [59].

The physical meaning of slip velocity is easily understood if only the mechanism of momentum transport in a gas is considered. Gas molecules travel a certain distance between two consecutive collisions and also between the last collision with another gas molecule and the wall. The „wall velocity" means the average flow velocity of the molecules at a distance equal to the mean-free path from the wall. In gas flow through a capillary, the molecules at a distance equal to the mean-free path from the wall have, on the average, a nonzero velocity in the direction of flow. As the mean-free path becomes an increasingly greater fraction of the capillary diameter, the „wall velocity" increases in significance relative to the average velocity.

The limiting situation in which the mean-free path of the gas molecules is greater than either the diameter of the capillary or its length is called „molecular streaming" or Knudsen flow. Under these circumstances only collisions between gas molecules and the walls of the tube arise. Therefore, Knudsen flow takes place by diffusive, in contrast to viscous, mechanism.

As the mean-free paths of gas molecules are, at room temperatures and pressures, roughly in the range of 0.01 to 0.1 μm, flow in pores under 10 nm diameter is usually of the Knudsen type [116].

According to the work of Scott and Dullien [117], the flow of gases under high vacuum, through fine capillaries, or through the small pores of a solid has been divided into three regimes, that of laminar or Poiseuille flow, the so called „slip" flow region, and a region of molecular streaming or Knudsen flow.

In the treatment of Scott and Dullien the molecules were divided into two groups: those that on the average do not collide with other molecules between two consecutive wall collisions and those that do. The fractional number of molecules in each group was estimated on the basis of collision probability considerations. The two flows were calculated and were assumed to be additive. Therefore, we have:

$$\frac{G}{\Delta P/L} = \left[1 - e^{-\sinh^{-1}\left(\frac{2r}{\lambda}\right)}\right]\left(\frac{\pi r^3}{M\overline{\upsilon}_m} + \frac{\pi r^4 P_m}{8\eta RT}\right) + e^{-\sinh^{-1}\left(\frac{2r}{\lambda}\right)} \cdot \frac{16r^3}{3M\overline{\upsilon}_m} \qquad (3.6.22)$$

slip term laminar term Knudsen term

where G is molar flow rate, r is the pore radius, λ is the mean free path, $\overline{\upsilon}_m$ is the mean molecular velocity, depending on the molecular mass M, can be calculated by Eq. (3.6.23), η the gas viscosity, $P_m=(P_1+P_2)/2$ the mean pressure, R the gas constant, T the temperature.

$$\overline{\upsilon}_m = \sqrt{\frac{8RT}{\pi M}} \qquad (3.6.23)$$

It is apparent that when $\lambda \gg 2r$, Eq. (3.6.22) reduces to the Knudsen formula; when $\lambda \ll 2r$, Eq. (3.6.22) becomes the Poiseuille equation. So the Knudsen number is defined as:

$$Kn = \frac{\lambda}{2r} \qquad (3.6.24)$$

$$\text{with} \quad \lambda = \frac{16\eta}{5\pi P_m}\sqrt{\frac{\pi RT}{2M}} \qquad (3.6.25)$$

Poiseuille flow (laminar flow) though a porous medium, occurs for $Kn \ll 1$; and Knudsen diffusion, occurs for $Kn \gg 1$; when $Kn \cong 1$, it is in the range of slip flow.

It is to be noted that in gas permeance a „permeability" k_D, can be defined by the equation [59]

$$\upsilon_g P = k_D \Delta P / L \qquad (3.6.26)$$

where k_D has the same dimensions [area/time] as the diffusion coefficient, can be deduced from Eq. (3.6.22):

$$k_D = \left[1 - e^{-\sinh^{-1}\left(\frac{2r}{\lambda}\right)}\right] \cdot \left(\frac{rRT}{M\overline{\upsilon}_m} + \frac{r^2 P_m}{8\eta}\right) + e^{-\sinh^{-1}\left(\frac{2r}{\lambda}\right)} \cdot \frac{16rRT}{3\pi M\overline{\upsilon}_m} \qquad (3.6.27)$$

Then the mole flow rate of the gas can be calculated by the gas general law:

$$G = \frac{P\upsilon_g}{RT} \qquad (3.6.28)$$

3.6.3 A Model Setup

Description of the problem

Permeability of the graded filtration structure is a very important parameter for the application and production. Flow rate through the filter membrane by air and water at a certain atmosphere is taken as a predominant measure to characterise the structure. A typical graded filter structure is shown in Fig. 3-25, which is composed of the substrate, the 316L functional layer (particle size < 16 μm and < 5 μm), and TiO_2 active layer. The particle size of the starting powder of each layer gradually decreases along the direction from substrate to the active layer, which leads to the decrease of the pore size.

In general, there are two types of substrates, planar and tubular. The radial flow through a cylindrical substrate is quite different from the unidirectional flow encountered in flat substrate. Radial geometry leads to mathematical complexities not encountered in analysis of planar moulds, because the pressure is not linear in terms of the radius and the pressure drop across the cake is not constant [118]. In most cases, however, the thickness of the cake on a porous tube is small compared to curvature radius of the substrate surface and the filtration process can approximately be described as one-dimensional filtration [119]. The correlation between the thickness and diameters of such hollow cylinder is described in Appendix 7.1.

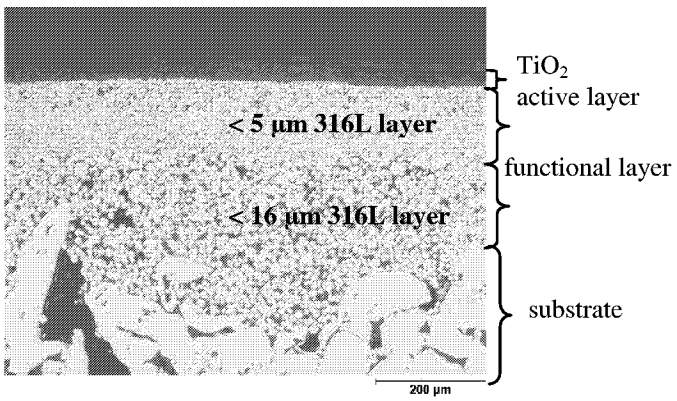

Fig. 3-25 Graded structure of a tubular probe

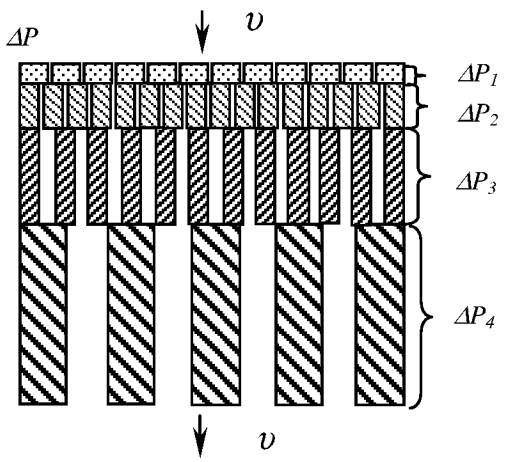

Fig. 3-26 An ideal conduit distribution in the graded structure

Description of the Model

A mathematical model basing Darcy's law was built up to simulate the flow process of the graded structure, which can predict the flow rate combining the pore structure of different layers, vice versa, if a desired flow rate was required, an optimal thickness pertaining to TiO_2 active layer can be estimated.

As described above, a permeability model based on conduit flow was adopted here. The key point of this method is that the porous medium was assumed to be equivalent to a conduit without paying any attention to the fact that different pores are interconnected with each other. Fig. 3-26 shows the illustration of an ideal conduit distribution of the graded structure. In this model the interfaces between two layers, which can be observed in Fig. 3-25, are neglected. However, it must be known that a boundary resistance could appear when two porous media are interpenetrated [120].

Combining the above analysis, Darcy's law in Eq. (3.6.1) can be rewritten into the following several equations for the graded structure:

$$\frac{\Delta P_i}{L_i} = \frac{\upsilon \cdot \mu}{k_i} \tag{3.6.29}$$

$$\Delta P = \sum_{i=1}^{4} \Delta P_i \tag{3.6.30}$$

$$\dot{Q} = \upsilon \cdot A \tag{3.6.31}$$

where i represents different layers, 1: TiO_2 active layer; 2: 316L (particle size < 5 μm) functional layer; 3: 316L (particle size < 16 μm) functional layer; 4: substrate; υ is the fluid velocity.

Now how to define the permeability k is the crucial point. Elmaleh et al. [120] adopted Carman-Kozeny model in their two-layer graded structure to make some prediction on pore numbers in the two different layers. Inspired from their work, the Carman-Kozeny model will be also used here for its simplicity and accuracy at a quite low *Re* number.

Comparing the permeability parameter of the Carman-Kozeny equation Eq. (3.6.12) and that in Forchheimer equation (Eqs. 3.6.19 to 3.6.21), it is obvious that $k=1/\alpha$. The difference between these two equations lies only on the inertial item in the latter. In our case, as told in the section 3.6.1, the experimental data show that the laminar flow dominates in the process. If the pressure drop is enlarged, *Re* number is increased, the flow is out of the laminar range, the equation Eq. (3.6.29) should be substituted by Eq. (3.6.19) to ensure the validity of the model.

Solving the Equations

As told above, the main aims of the model are to simulate the flow rate of the graded structure in a fixed manufacture route and to estimate an optimal thickness value of TiO_2 active layer at a desired flow rate.

Computational codes based on above algorithms were compiled and listed in Appendix 7.2 and 7.3. The flow charts are shown in Fig. 3-27 for fluid flow and Fig. 3-28 for gas flow. It is known from the above investigation that the difference between the fluid flow and the gas flow lies only on the calculation of the permeability *k* pertaining to different flow media.

Table 3-9 listed input data set for a sample (Sika R 10 AX).

Table 3-9 An example for input data set,
the data are referred to a commercial Sika R 10 AX membrane from GKN catalog.

Parameters	Signs	Names in the code	Data
For fluid flow			
Viscosity of the fluid (water)	μ	VMIU	1.005×10^{-3} Pas
Thickness of different layers	L	AL	3 mm
Hydraulic diameter	D_H	DH	17 μm
Average particle size	D_{p2}	DP2	150 μm
Pressure drop	ΔP	DELTP	300 mbar
Measured filter area	A	A	55.40 cm^2
Porosity	ϕ	FAI	43%
For gas flow			
Viscosity of the gas (air)	η	YITA	1.82×10^{-5} Pas
Thickness of different layers	L	AL	3 mm
Hydraulic diameter	D_H	DH	17 μm
Average particle size	D_{p2}	DP2	150 μm
Pressure drop	ΔP	DELTP	300 mbar
Measured filter area	A	A	55.40 cm^2
Atmosphere pressure	P	P	1.013×10^5 Pa
Atmosphere temperature	T	T	293 K
Gas constant	R	R	8.31×10^3 J/kmol·K
Molecular weight (air)	M	AM	28.964 kg/kmol
Mean free path (air)	λ	ALAMDA	6.08×10^{-8} m

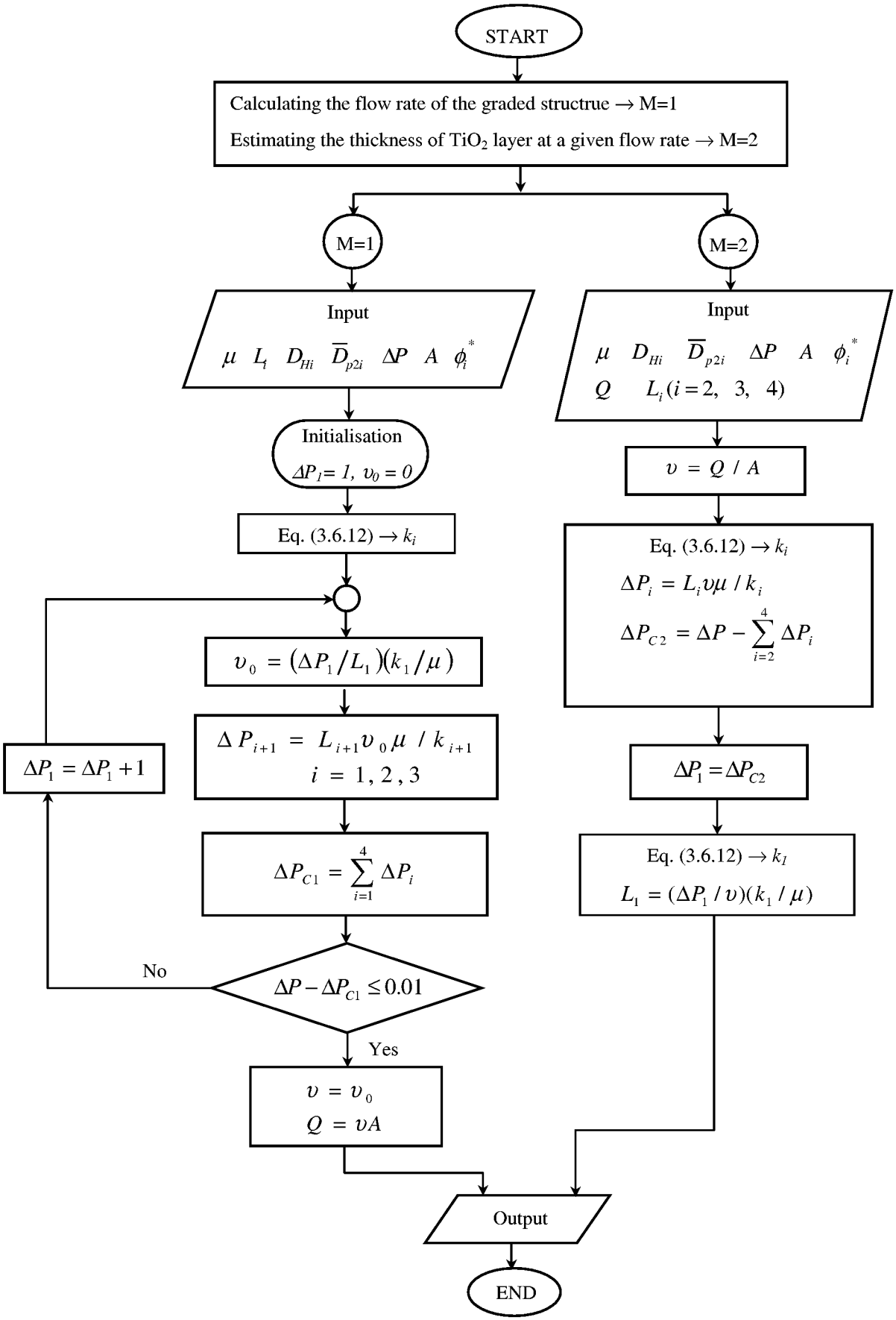

* note: if ϕ_i can not be obtained from the experiments, which can be calculated by Eqs. (3.6.08) and (3.6.11).

Fig. 3-27 Flow chart of the graded structure modelling for fluid flow,
a description of all symbols is given in the appended nomenclature.

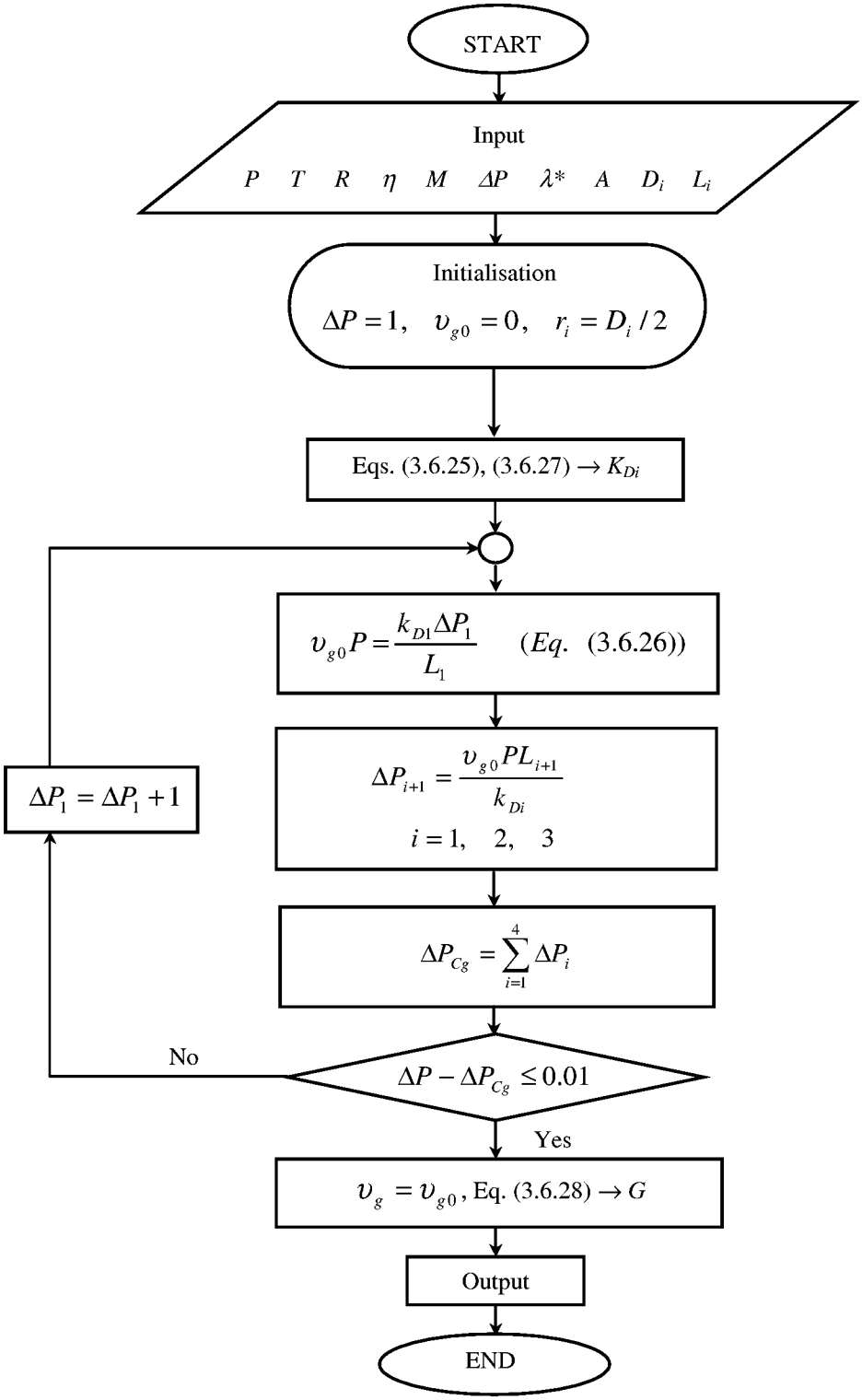

* note: λ can be calculated from Eq. (3.6.25), also can be obtained from experimental data [115] ≅ 6.08×10^{-8} m

Fig. 3-28 Flow chart of the graded structure modelling for gas flow,
a description of all symbols is given in the appended nomenclature.

4 Results and Discussions

All experiments commenced with depositing the TiO_2 layer onto a graded substrate made of Sika R 20 + 316L (particle size < 16 μm) intermediate layer. The compositions of the suspensions were listed in Table 3-5. After spraying the awesome droplets and agglomerates of TiO_2 layer can be observed clearly even under optical microscope. The sample was sintered at 950°C, 1h. Fig. 4-1 show the SEM images of the sample, the spraying parameters are listed on the right side of the picture.

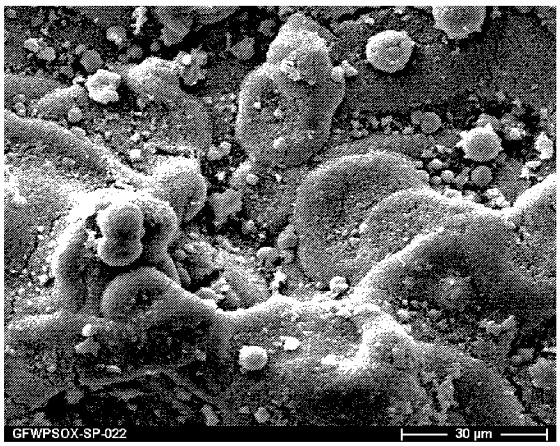

Nozzle:	1.8 mm
Pressure:	0.5 bar
Distance:	250 mm
Velocity:	3500 mm/min
Spraying Beam:	5 units
Suspension feed rate:	3 units
Meander:	1 line
Layers:	5

Fig. 4-1 SEM image of the surface structure of one planar sample, × 1000

The possible reasons, which led to so uneven structure of the surface, were inferred as following: a.) the big droplets came into being during the spraying process, due to the rapid evaporation rate of the solvent; b.) the undispersed powder agglomerates in the suspension were sprayed onto the layer; c.) unsuitable spraying parameters caused the inhomogeneity of the coating.

Basing above analyses a series of optimisations of the suspensions and the spraying process were carried out.

4.1 Optimisation of the Suspensions

4.1.1 Lowering the Evaporation Rate of the TiO_2 Suspension

The drying curves of different mixtures were obtained by measuring the variation of the liquid weight changing with the time. Fig. 4-2 a.) to c.) show the measurement results.

From these drying curves of different mixtures it is obvious that the composition of the mixtures has a great influence on the evaporation rate. The addition of terpineol or water can slow down the drying speed compared with that of pure ethanol. Moreover, pure isopropanol dries faster than pure ethanol.

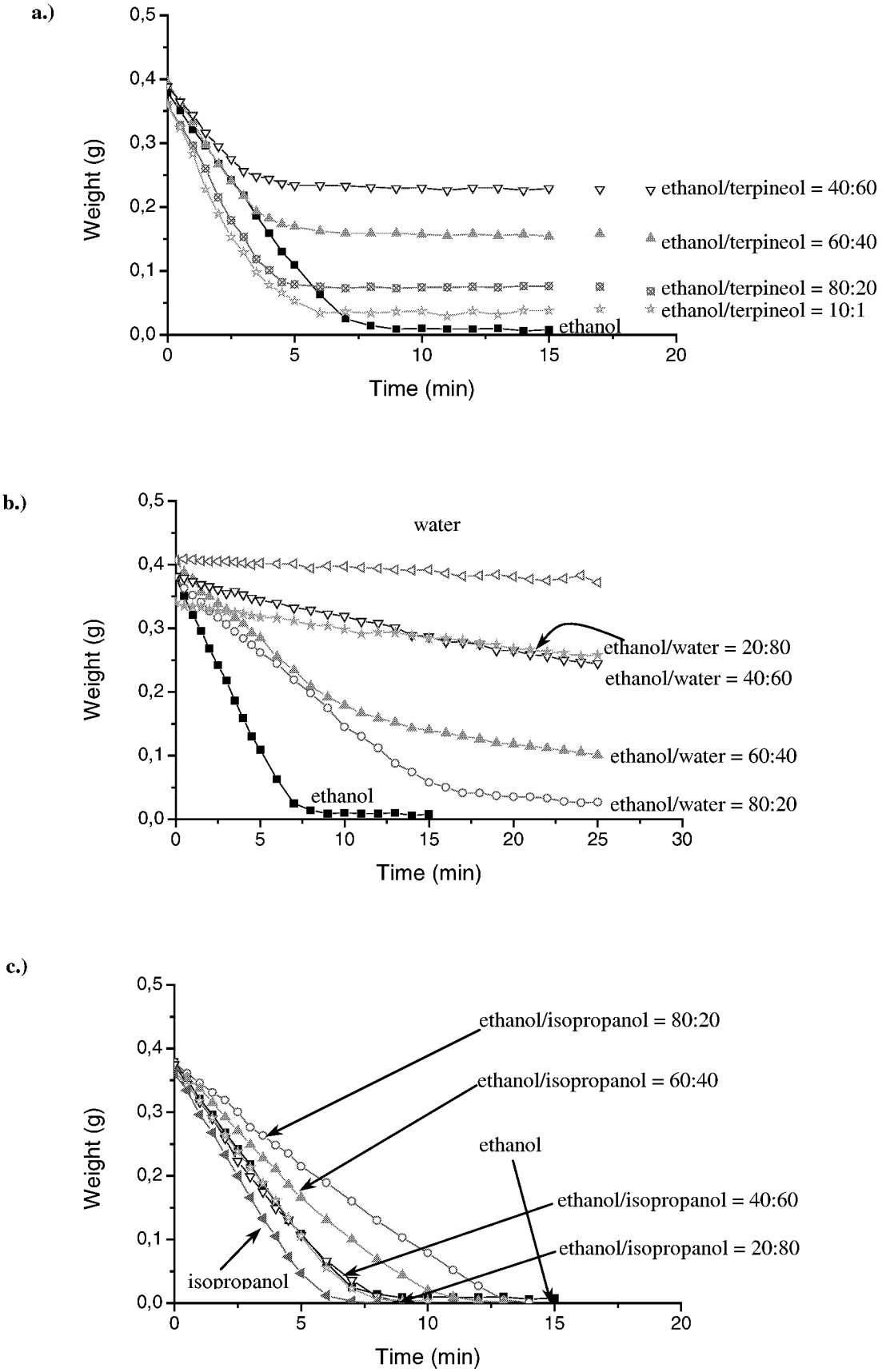

Fig. 4-2 Drying curves of different mixtures, the unit of the proportion is wt.%

a.) ethanol and terpineol; b.) ethanol and water; c.) ethanol and isopropanol

Comparing the drying curves in the three diagrams the former two are preferable because of the evident changes in drying speed. Considering that water has a higher polarity than terpineol, which probably leads to the corrosion of the substrate, the mixture of ethanol-terpineol was taken as the new solvent to substitute ethanol.

In order to find the proper ratio between ethanol and terpineol different suspensions were made with different proportion between ethanol and terpineol, also these suspensions were used to spray onto substrates to verify if the variations brought any improvement of the layer quality. During this process it was found that the viscosity of the suspensions had a great influence on the spraying. There existed a risk that the nozzle would be blocked when spraying with a quite viscous suspension. The viscosity measurement results of these suspensions are shown in Fig. 4-3. The surface structure of the samples, which was produced by these suspensions are shown in Fig. 4-4 a.) and b.).

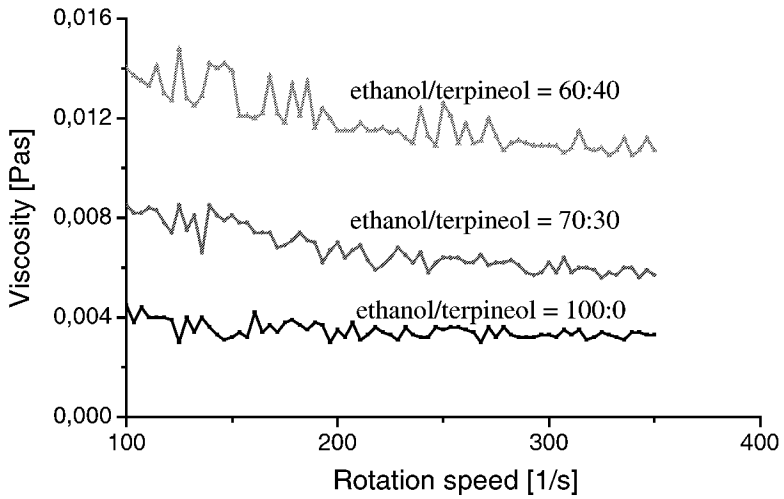

Fig. 4-3 Influence of terpineol content on the viscosity of the suspension

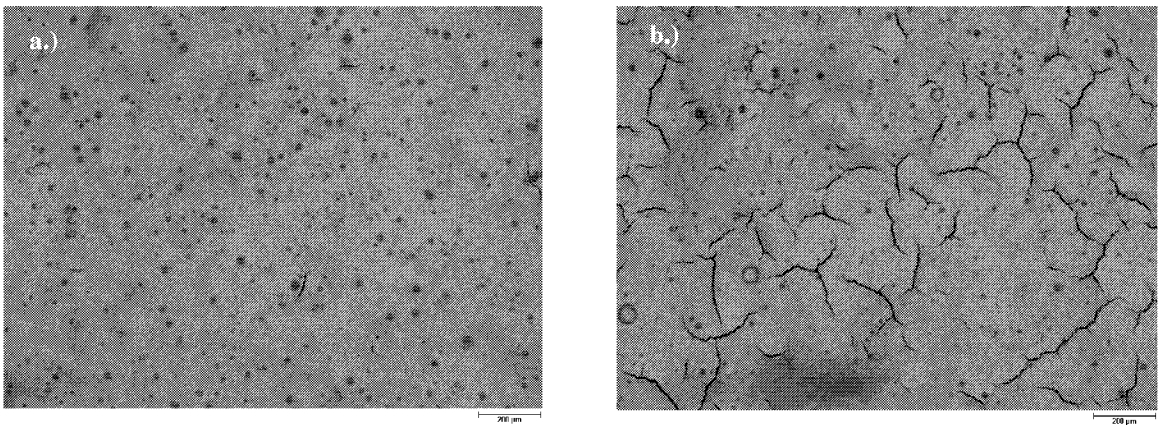

Fig. 4-4 Surface structure by LM

a.) using the suspension — ethanol/terpineol = 70:30; b.) using the suspension — ehtanol/terpineol = 60:40

Comparing the surface structures in Fig. 4-4 and Fig. 4-1, it is obvious that the layer quality has been improved though some agglomerates can be also observed. Comparing the spraying ability of different suspensions, it has been found that the viscosity of the TiO_2 suspension should not be greater than 7 mPas, otherwise there causes a clog of the nozzle and a worse quality of the sprayed layers (see Fig. 4-4 b.)). For further attempts the weight ratio between ethanol and terpineol was fixed as 70:30.

4.1.2 Dispersing the TiO_2 Suspension

The electrokinetic behaviour was determined as a function of pH^*. The isoelectric point of the TiO_2 suspension in ethanol-based solvent is pH^*_{iep} = 4.2 [77]. After adding PEI into the suspension, the isoelectric point was shifted to the base side, which can be seen in Fig. 4-5. The isoelectric point for the TiO_2 powder in ethanol with 3 wt.% PEI is approximately 9.6. The weight percent of PEI is calculated by using the amount of PEI divided that of the solid. If the amount is referred to the whole suspension, it becomes 1.2 wt.%.

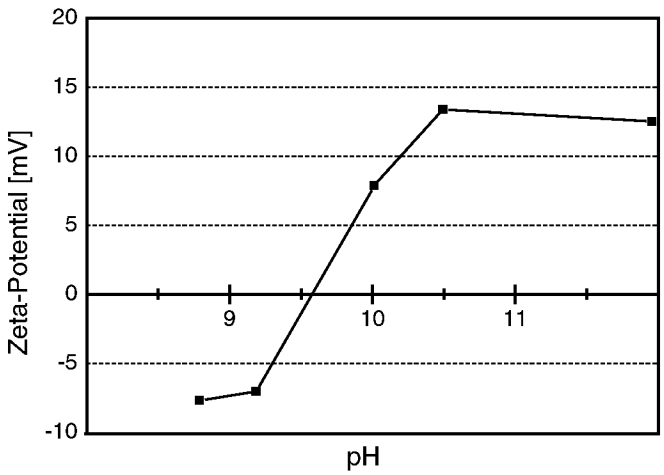

Fig. 4-5 Relationship between zeta-potential and pH value
of the TiO_2 suspension (39.5 wt.% powder in ethanol + 3 wt.% PEI referred to the solid content)

For the very low polarity of terpineol, the addition of it has almost no influence on the isoelectric point. As aforementioned, electrostatically stabilised suspensions of ceramic powders in ethanol can be obtained by changing the operational pH and controlling the ionic strength (Debye length). Adding acid into the suspension which shifts pH^* sufficiently far away from the pH^*_{iep} is able to disperse the primary particles and stabilise the suspension providing that the pH value is in the right range.

Referencing the work by Widegren etc. [77] it is found that TiO_2 can be stabilised over a wide range of acetic acid (HAc) addition. By means of pH measurements and settling tests 6.6 wt.% HAc (over the whole suspension) was added into the suspension. The isoelectric point pH^*_{iep} was shifted to approximate 4.5~5.0. After over 24 h settling, there was no obvious particle/liquid interface observed.

4.1.3 Controlling the Viscosity of the Suspension

Viscosity of the suspension (TiO_2 + ethanol + terpineol + HAc + PEI) is an important parameter for the spraying process. A relation between the PEI content and the viscosity was found shown in Fig. 4-6. It is obvious from the curve that the 0.8 wt.% PEI content leads to a viscosity peak 0.015 Pas, then if the PEI content is increased, the curve keeps quite plain. Of course, this highest viscosity point should be left far away, 1.5 wt.% PEI was chosen as an optimum content for the suspension. Again, the content of PEI was referred to the solid's content.

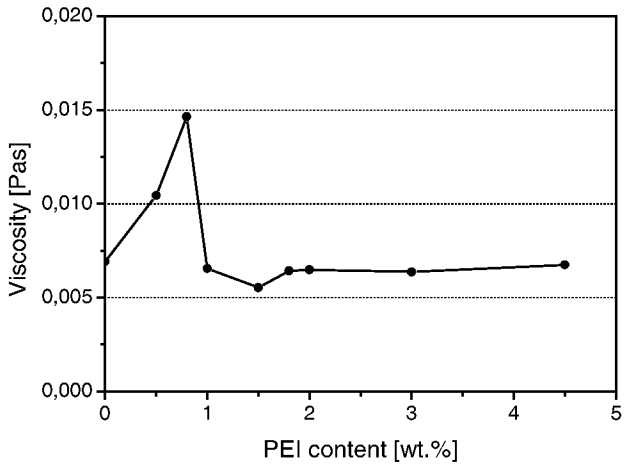

Fig. 4-6 Influence of the PEI content on the viscosity of the TiO_2 suspension, the PEI content is referred to the solid content.

Based on the above optimisation work a modified TiO_2 suspension was obtained, whose composition is listed in Table 4-1.

Table 4-1 Definition of a standard suspension for the continuous attempts

composition	weight percent [%]
TiO_2	39.8%
ethanol	37.1%
terpineol	15.9%
HAc	6.6%
PEI	0.6%

4.1.4 Ageing Test of the Suspensions

An ageing test was designed for the standard suspensions. During the period of 51 days the zeta-potential, pH value, particle size distribution and viscosity of the TiO_2 suspension were measured in one week interval. The ageing curves of different parameters are shown in Fig. 4-7 a.) to d.). It has to be mentioned here that before each measurement the suspensions were set in a tubular mixer to be homogenised at least for half a hour.

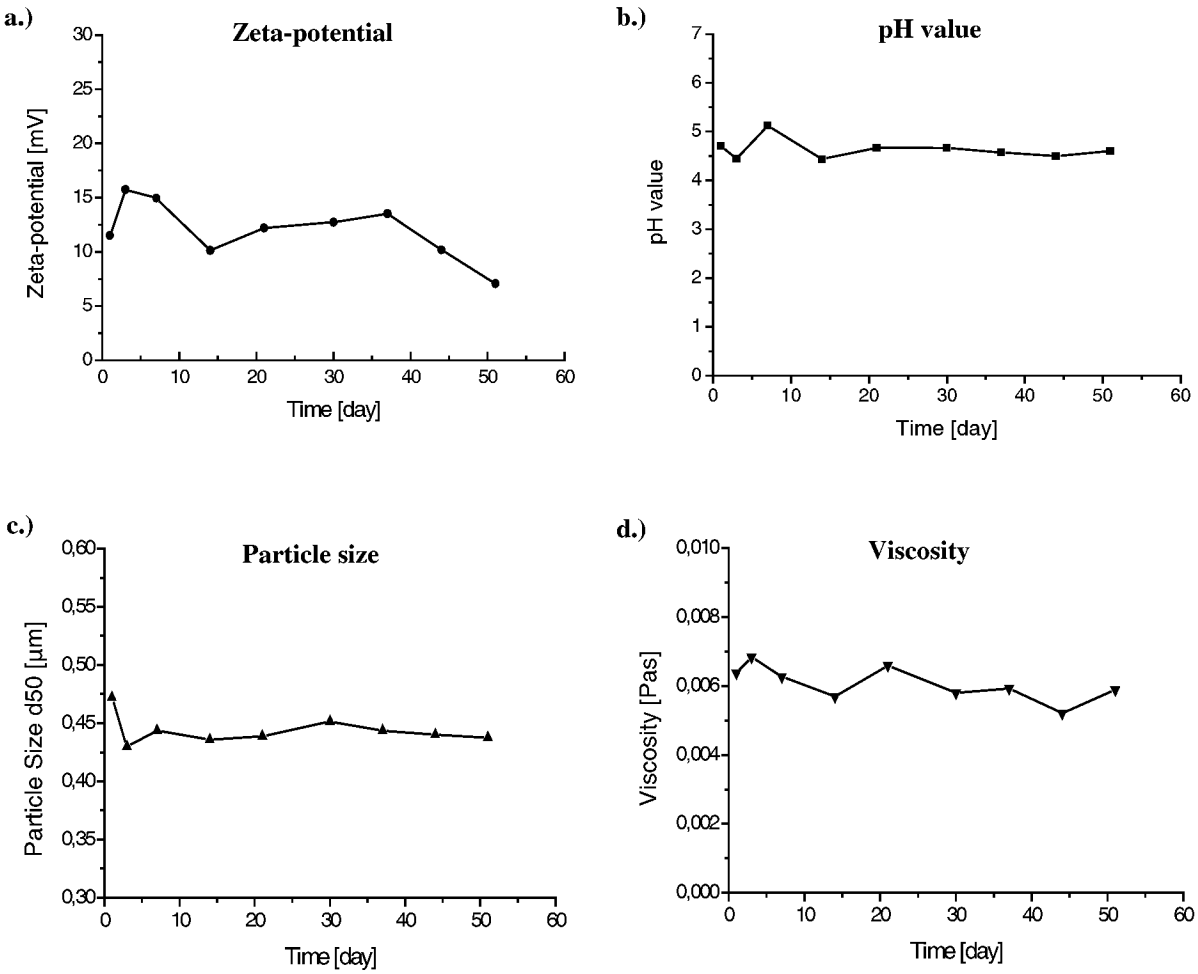

Fig. 4-7 Ageing curves of different parameters for the standard suspension,
a.) zeta-potential; b.) pH value; d.) average particle size (measured by UPA); d.) viscosity

It can be observed from these diagrams that the four parameters keep quite stable during the test period, except that zeta-potential shows a slight decreasing tendency and the viscosity curve shows a small decrease along with time.

The ageing curve of 316L (particle size < 5 µm) suspension was tested only by measuring viscosity, for it is the only qualified parameter which can be used to describe the characteristics of the stainless steel suspension here. Fig. 4-8 shows the ageing curve in 35

days duration. It is known from the diagram that the suspension was almost unchanged during the storage. Therefore, the same spraying behaviour can be expected even after 35 days.

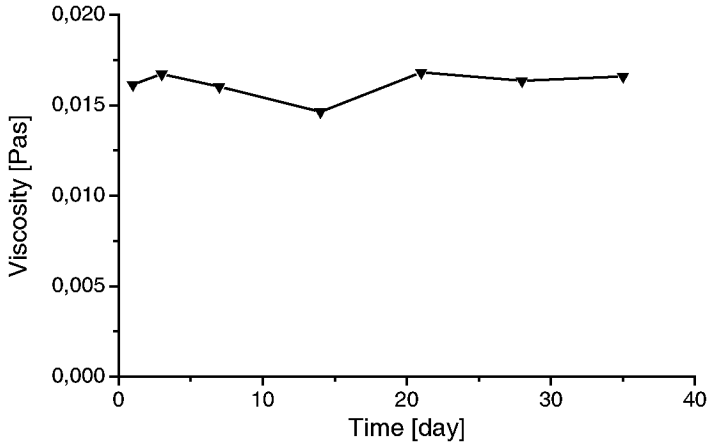

Fig. 4-8 Ageing curve of the viscosity of the 316L (particle size < 5 μm) suspension

4.1.5 Improving the Milling Process

Milling duration is very important for the industrial capacity. Overtime milling leads to a waste of energy also. A milling test was done — after milling by a fixed time, the particle size distribution and specific surface area were measured, whose results are shown in Table 4-2.

Table 4-2 Particle size distribution and specific surface area of the TiO_2 changing with the milling time

parameters \ milling duration [h]		0	3	9	27	81
Particle size distribution* [μm]	d_{10}	0.03	0.02	0.03	0.03	0.03
	d_{50}	0.18	0.16	0.11	0.13	0.13
	d_{90}	0.43	0.43	0.19	0.38	0.43
Specific surface area [m^2/g]		15.35	14.95	14.77	15.0	14.79

* Note: the particle size distribution was measured by Laser Particle Sizer.

It is known from the above table that the milling has an influence on the d_{50} value and specific surface area of the powder to some extent. Between 9 hours and 81 hours milling, there exists no great difference in the average particle size and the specific surface area. So the milling time of the TiO_2 suspension was shorted to 20 h.

4.2 Optimisation of the Spraying Process

4.2.1 Characterising the Main Spraying Parameters for Planar Application

Influence of the Spraying Beam

The shape of the spraying beam is controlled by the amount of horn gas, adjusted by the screw 1 (marked in Fig. 3-4 and Fig. 3-5). The different spraying surfaces of the suspensions made of the TiO_2 and the 316L (particle size < 5 μm), which were produced by changing the amount of horn gas, are photographed and shown in Fig. 4-9 and Fig. 4-10 separately. With adjusting the screw 1 the shape of the spraying surfaces changes from circle (SB=1) to ellipse (SB>1).

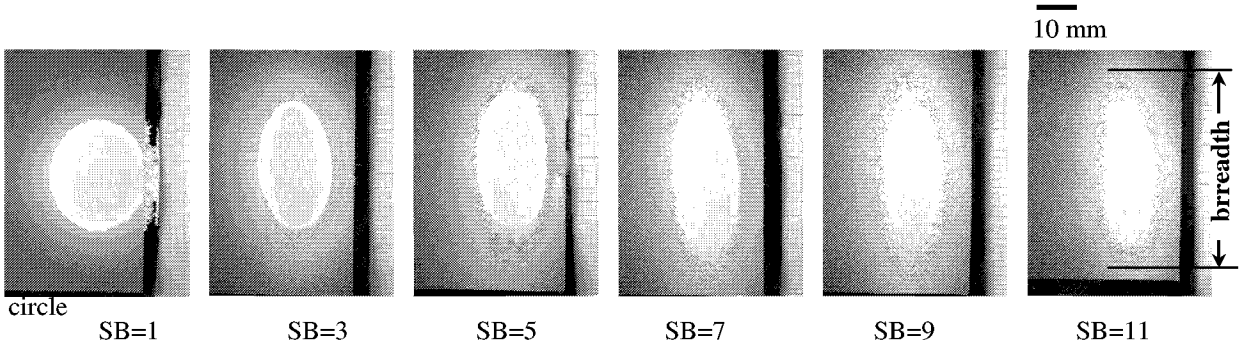

Fig. 4-9 Spraying surfaces of the TiO_2 suspension changing with the scales on the Screw 1, N=1.8, P=0.5, D=230, V=0, SA=7, the gun keeps spraying for 5 seconds in stillness.

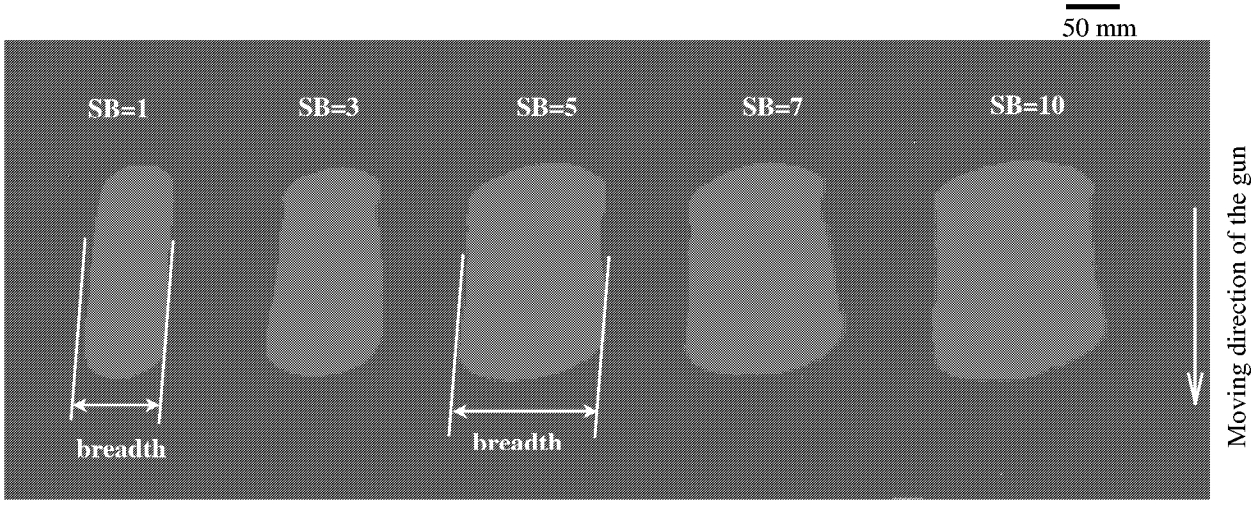

Fig. 4-10 Spraying surfaces of the 316L (particle size < 5 μm) suspension changing with the scales on the screw 1. Spraying parameters: N=1.8, P=1.5, D=230, V=3500, SA=10, the gun moves 210 mm in the arrow direction as shown on the picture.

Subsequently, the influence of the scales of the screw 1 on the feed rate of suspensions has been investigated. The results of different suspensions are shown in Fig. 4-11 a.) TiO_2 suspension and b.) 316L suspension (particle size < 5 μm).

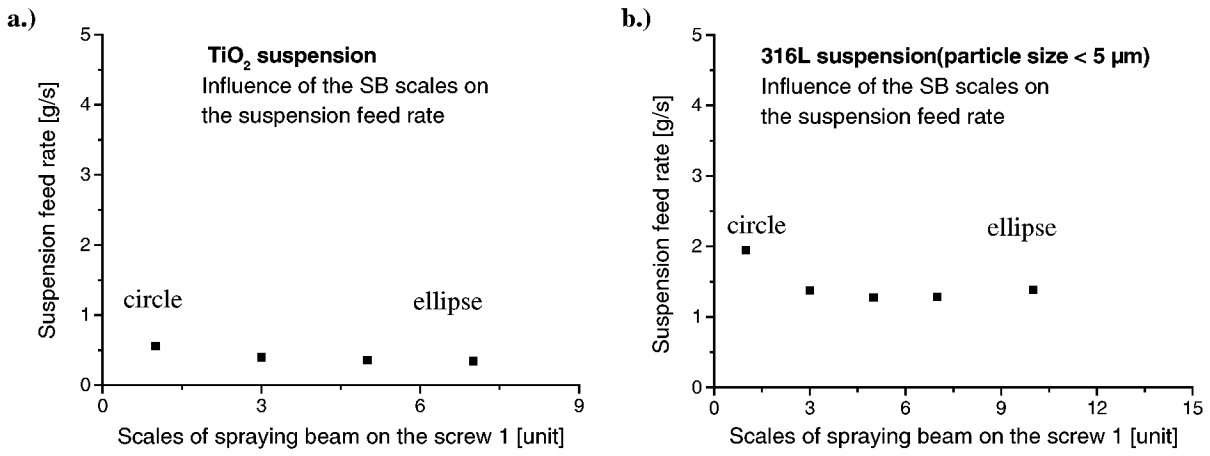

Parameter set: N=1.8, P=0.5, D=230, V=3500, SA=7 Parameter set: N=1.8, P=1.5, D=230, V=3500, SA=10

Fig. 4-11 Corelation between the spraying beam and the feed rate of the suspension

a.) TiO_2 suspension; b.) 316L (particle size < 5 µm) suspension

As told in the experimental part, according to the principle of the spraying gun, the screw 1 regulates only the shape of the spraying beam, which will be changed from circle to ellipse by varying the scales from 1 to greater than 1, and should have no influence on the feed rate of suspensions. From Fig. 4-11 a.) and b.) this conclusion can be verified to some extent even there exists a slight increase when the scale is adjusted very low, e.g. approximate 1.

The thickness distribution of different sprayed layers as those shown in Fig. 4-10 was measured. The results are shown in Fig. 4-12 a.) to b.) for TiO_2 layers, Fig. 4-13 a.) and b.) for 316L (particle size < 5 µm) layers.

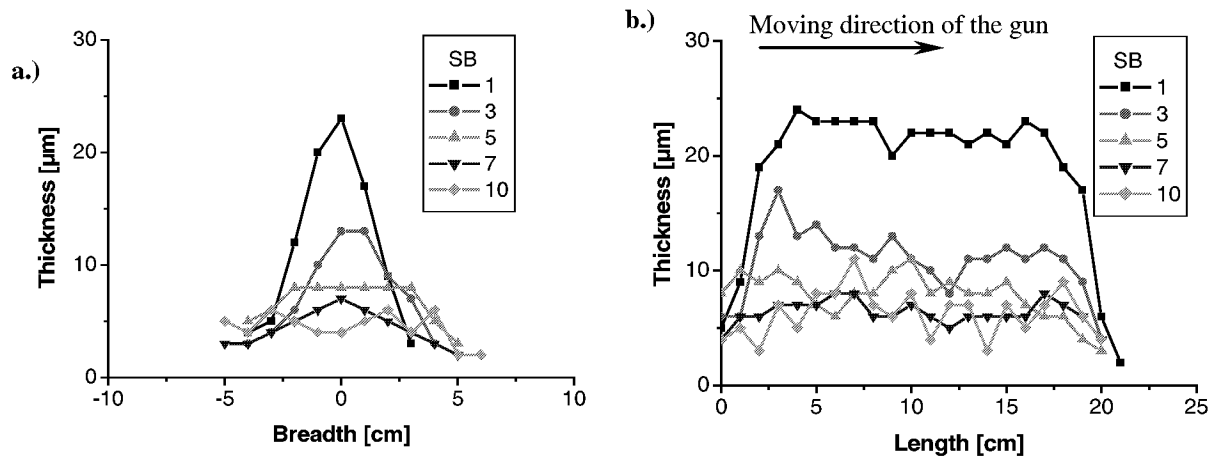

Fig. 4-12 Thickness distribution changing with spraying beam for **TiO_2** layers,

N=1.8, P=0.5, D=230, V=3500, SA=7

a.) in breadth direction (line 1 in Fig. 3-8); b.) in length direction (line 2 in Fig. 3-8)

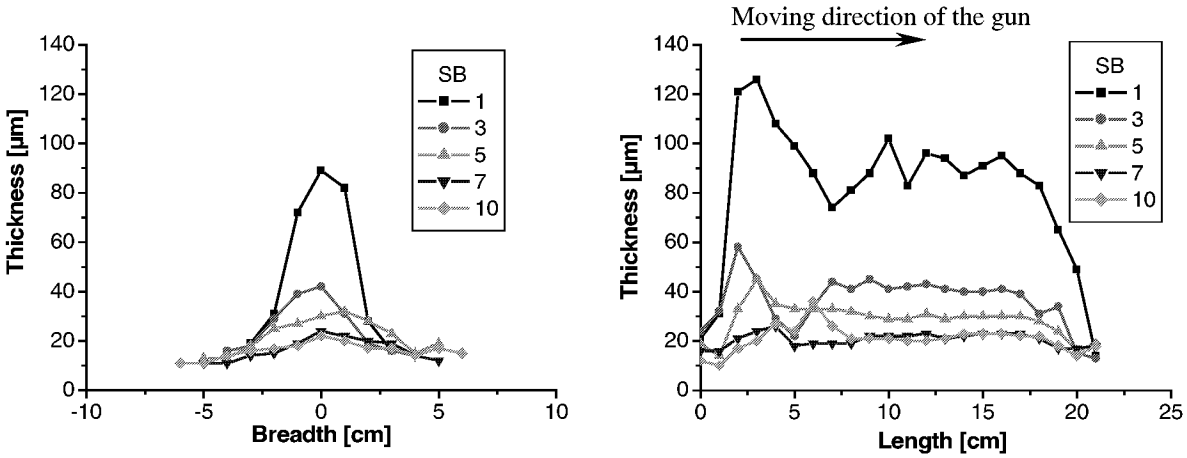

Fig. 4-13 Thickness distribution changing with spraying beam for **316L (particle size < 5 µm)** layers
N=1.8, P=1.5, D=230, V=3500, SA=10,
a.) in breadth direction (line 1 in Fig. 3-8), b.) in length direction (line 2 in Fig. 3-8)

It can be observed from the results clearly that there exists a Gaussian distribution of the sprayed layer thickness along the breath direction; although te scale of the spraying beam was adjusted over 10, the breadth of the layer stayed nearly unchanged (not shown in the diagram).

In order to avoid the uneven structure of the sprayed surface and get a homogeneous thickness distribution, for the planar samples, the scales of the spraying beam were defined as 5 for the all attempts.

Influence of the Feed Rate of Suspensions

The feed rate of the suspension of the gun is controlled by the opening of the aperture of the nozzle, controlled by the screw 2 (marked in Fig. 3-4 and Fig. 3-5). The photographs of different spraying surfaces by changing the scales of the screw 2 from 5 to 25 are shown in Fig. 4-14.

Subsequently, the influence of the nozzle's opening on the feed rate of suspensions has been investigated. The results of different suspensions are shown in Fig. 4-15 a.) TiO_2 suspension and b.) 316L (particle size < 5 µm) suspension.

It is obvious that with increasing the opening, the feed rate of suspensions can be enhanced. Using the same spraying parameter sets, the feed rate of tsuspensions changes similarly both for TiO_2 and for 316L (particle size < 5 µm). Comparing Fig. 4-14 with Fig. 4-10 it can be observed that the feed rate of the suspension has a greater influence on the breadth of the

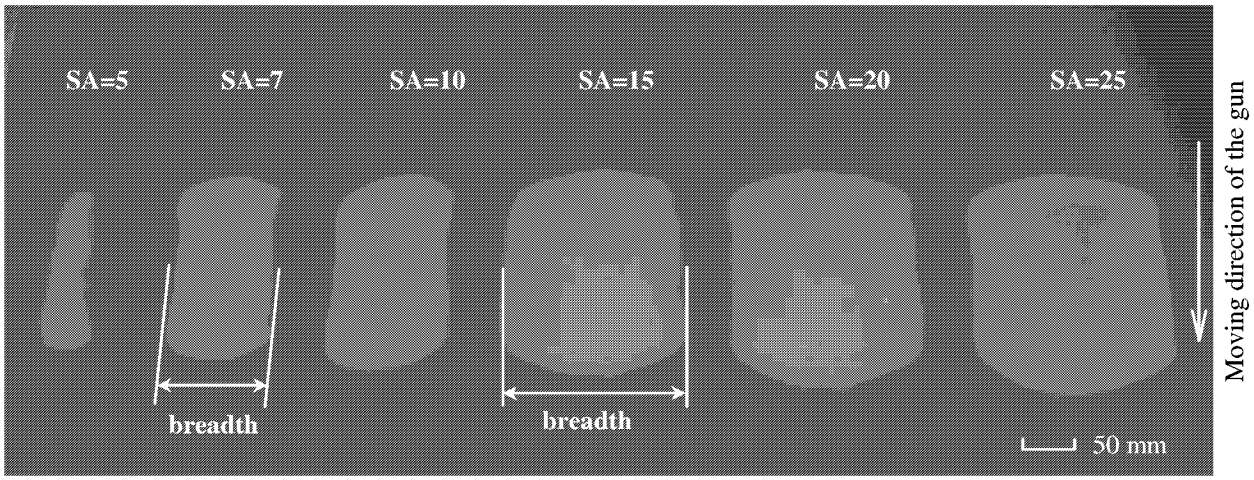

Fig. 4-14 Spraying surfaces of the 316L (particle size < 5 μm) suspension changing with the scales on the screw 2. N=1.8, P=1.5, D=230, V=3500, SB=5, the gun moves 210 mm in the arrow direction as shown on the picture.

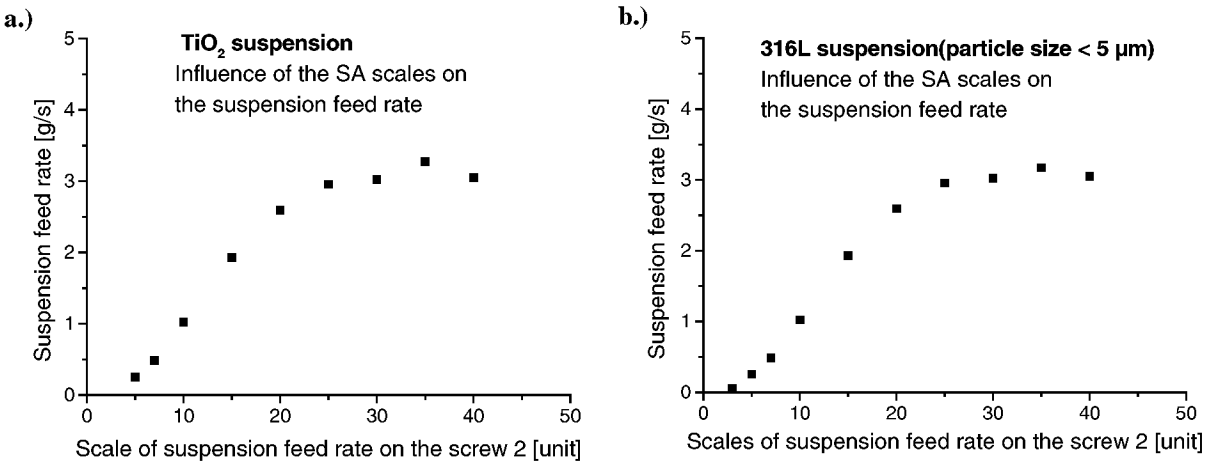

Fig. 4-15 Influence of the scales of the screw 2 on the feed rate of suspensions
N=1.8, P=1.5, D=230, V=3500, SB=5
a.) TiO_2 suspension; b.) 316L (particle size < 5 μm) suspension

sprayed layer. The higher the feed rate of suspensions is, the broader the breadth of the sprayed layer will be. When the scales are chosen greater than 30, there exists only tiny difference of feed rate of the suspension with the variation of the scales.

The thickness distribution of different sprayed layers as those shown in Fig. 4-14 was measured. The results are shown in Fig. 4-16 a.) to b.) for TiO_2 layers, Fig. 4-17 a.) and b.) for 316L (particle size < 5 μm) layers. Similarly there exist the same Gaussian distribution of the layer thickness along the breadth direction.

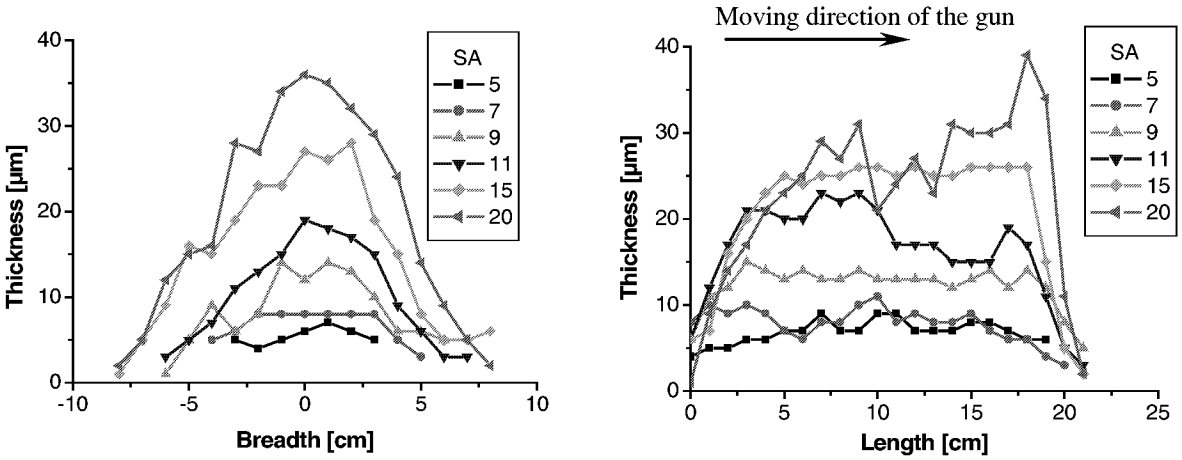

Fig. 4-16 Thickness distribution changing with the feed rate of the suspension for **TiO_2** layers,
N=1.8, P=0.5, D=230, V=3500, SB=5
a.) in breadth direction (line 1 in Fig. 3-8); b.) in length direction (line 2 in Fig. 3-8)

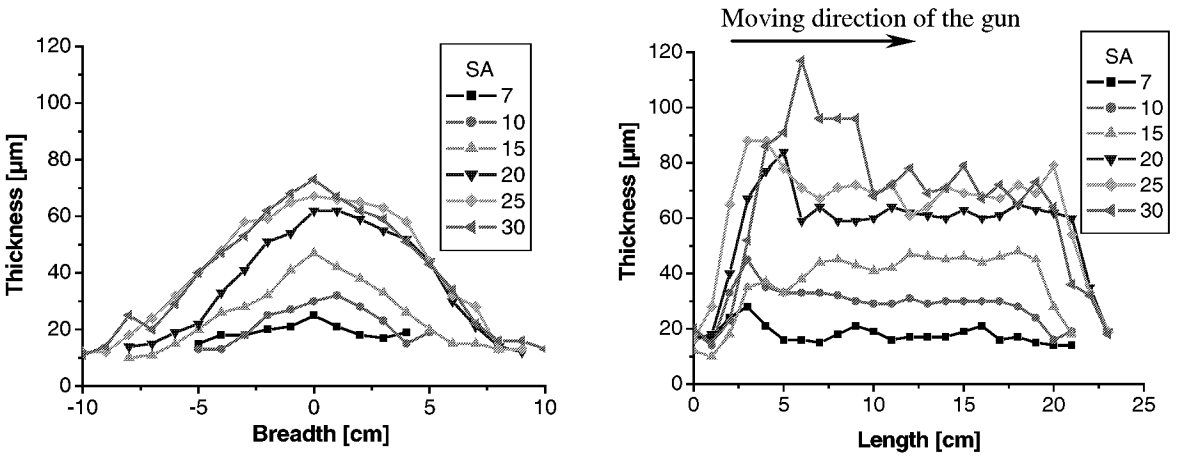

Fig. 4-17 Thickness distribution changing with the feed rate of the suspension for **316L (particle size < 5 µm)**
N=1.8, P=1.5, D=230, V=3500, SB=5,
a.) in breadth direction (line 1 in Fig. 3-8); b.) in length direction (line 2 in Fig. 3-8)

According to the results of the above investigations it is known that a homogeneous layer thickness can be reached by placing the samples in the middle of the spraying surface as possible, of course, the size of samples should be small enough in the range which can be covered by the spraying surface, otherwise, a meander spraying is recommended; also the gun should be kept for spraying in a quite long distance to get a stable layer thickness, to avoid the fluctuation at the beginning or the halting position of the spraying surface.

Basing the above experimental results it is obvious that the feed rate of suspensions has a great influence on the thickness distribution of the sprayed layer.

The function of the two intermediate layers is to cover the large pores in the substrate and to provide a homogeneous support for the applied thinner functional layer. So these two layers should be thick enough to lower the roughness of the substrate. Therefore, the scales of the feed rate for the 316L suspensions of particle size < 16 μm and of particle size < 5 μm were chosen 35 and 20 separately. For TiO_2 functional layer, as told at the beginning of this work, it should be as thin as possible and approximate 20 μm of our goal. Due to this consideration, the scales of the suspension feed rate should be used as 5 or 7 basing the above experiments.

Influence of the Spraying Pressure

The photographs of the spraying surfaces of TiO_2 suspension changing with the pressure are shown in Fig. 4-18. The ellipses of the sprayed surfaces are marked in the picture, which is the most effective part of the spraying surface; the part which is over the ellipse is defined as „over spray" here, which leads to the waste of the material and uneven surface structure and should be avoided during the spraying. It must be reminded here that the particles were

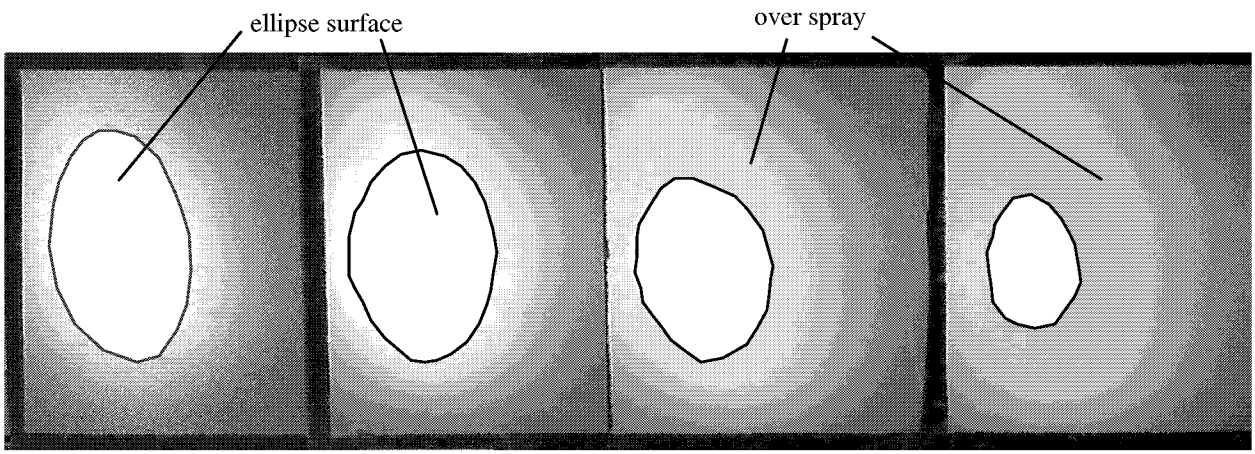

Fig. 4-18 Spraying surfaces changing with different pressures of TiO_2 suspension, N=1.8, D=230,V=0, SB=5, SA=7, the gun keeps spraying for 5 seconds in stillness.

nebulised at the edge of the spraying beam at a high pressure during the spraying. The higher the pressure is, the stronger the nebulae will be, and the smaller the effective surface is, which can be seen from Fig. 4-18. Furthermore, the surfaces were observed by optical microscope, when the pressure is larger than 1.0 bar, there are many agglomerates on the spraying surface. The relation between the suspension feed rate and the pressure is shown in Fig. 4-19.

From the diagram it is known that the feed rate of the suspension increases with the enhancement of the spraying pressure. From the above thickness measurement results, it can be deduced that the layer thickness is also increased by increasing the pressure.

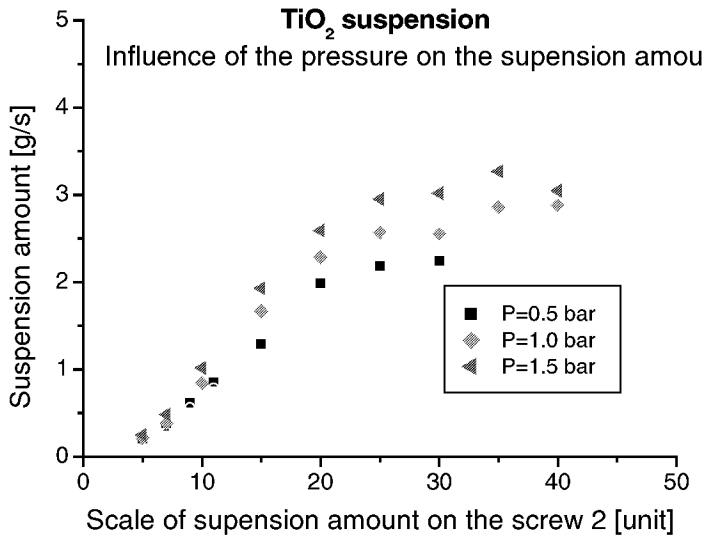

Fig. 4-19 Influence of the pressure on the suspension feed rate of the gun

N=1.8, D=230, V=3500, SB=5, SA=7

Based on the analyses of the above experiments for TiO_2 suspension the pressure of 0.5 bar was chosen as an optimal value, because there was less over-spray, less agglomerate and lower thickness than those by the other pressures. The latter leads to a flexibility to obtain an ideal thickness by multilayer spraying mode. For the 316L suspensions the same investigation was done and the spraying pressure was chosen 1.5 bar.

Influence of the Spraying Speed

The influence of the spraying speed on the layer thickness is shown in Fig. 4-20 a.) and b.). There exists such relation between these two parameters that higher spraying speed leads to a lower thickness of the sprayed layer.

If only one point on the middle of the layer surface was chosen to represent the layer thickness, a diagram can be obtained shown in Fig. 4-21, by which the relation between the spraying speed and the layer thickness can be seen clearly.

Fübi [66] put forward a similar relationship between the thickness and the spraying speed in his thesis, which was verified by this work to some extent.

According to the thickness distribution in Fig. 4-21, 3500 mm/min was chosen for all planar samples due to the appropriate thickness by this speed, while it is flexible to get a required layer thickness through multilayer spraying.

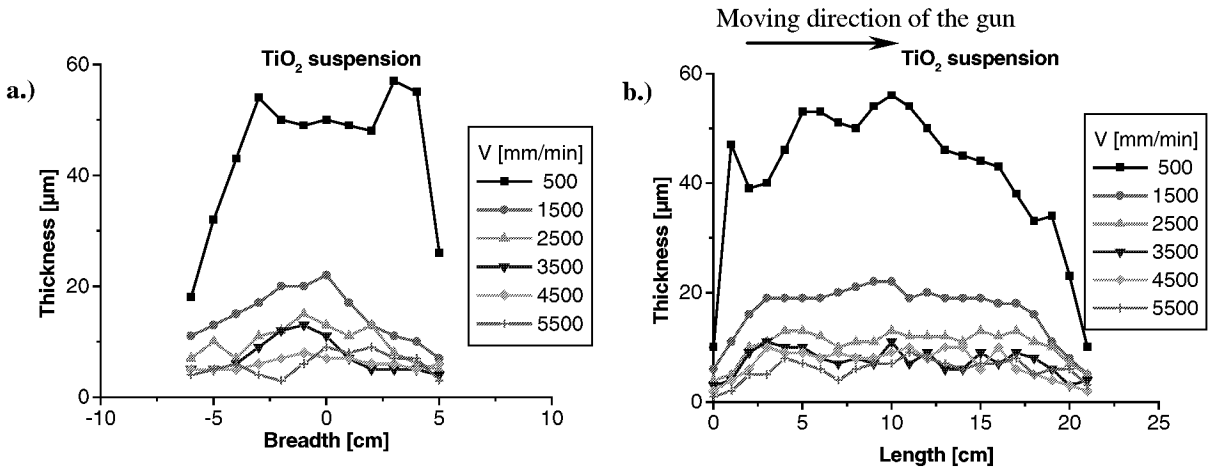

Fig. 4-20 Relationship between the spraying speed and layer thickness of **TiO_2 suspension**

N=1.8, P=0.5, D=230, SB=5, SA=7,

a.) in breadth direction (line 1 in Fig. 3-8); b.) in length direction (line 2 in Fig. 3-8)

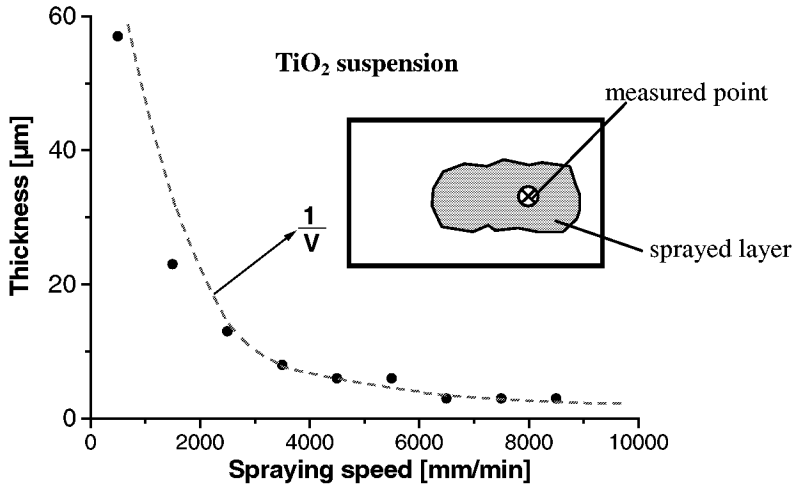

Fig. 4-21 Relation betwen the spraying speed and the layer thickness

N=1.8, P=0.5, D=230, SB=5, SA=7

Influence of the Spraying Distance

The spraying distance can be changed in a great range as shown in Fig. 4-22. With increasing the spraying distance (from the nozzle tip to the surface of samples) the thickness of the sprayed layer is decreased.

Of course, only by a fixed spraying distance the aforementioned parameter can be optimised.

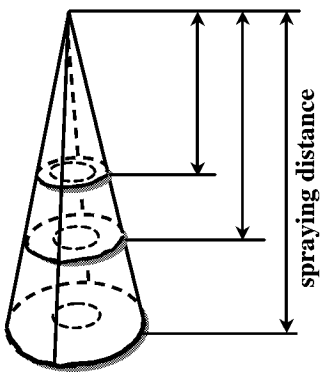

Fig. 4-22 Changing spraying distance

Also „over spray“ should be considered here. If the distance is adjusted too large, there forms a great range of over spray, which leads to a loss of the effective ellipse. For all planar samples the spraying distance was chosen as 230 mm.

Influence of the Meander Spraying

If the samples are so large that only one line layer can not cover the surface, a meander moving of the gun should be taken into account. That means, the application of meander spraying will be decided by the size of the samples.

For meander spraying in addition to the above investigated parameters the distance between the two meander lines is very important. Different coat surfaces were sprayed with changing the distance between two meandrous lines. The thickness of these layers were measured and shown in Fig. 4-23 a.) to c.). It is known from the diagrams clearly that the breadth of the sprayed layers is enlarged; with widening the distance between the two meanders, the thickness peak of the layer due to the overlapping of spraying lines is flatted.

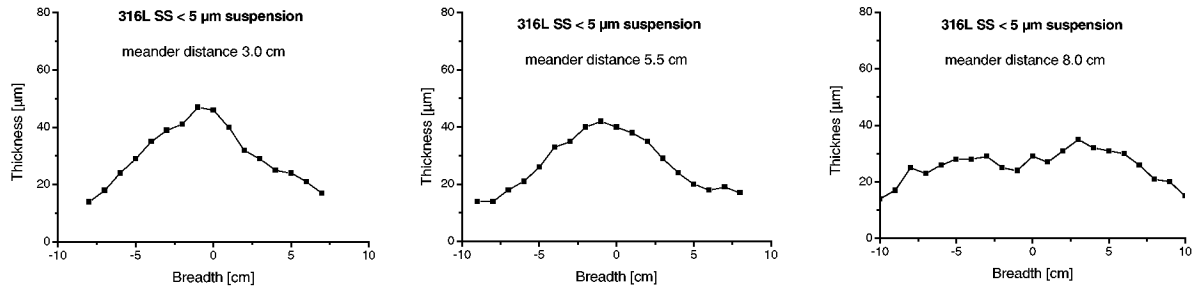

Fig. 4-23 Thickness distribution changing with the meander distance for 316L (particle size < 5 µm) suspension N=1.8, P=1.5, V=3500, D=230, SB=5, SA=10, in breadth direction (line 1 in Fig. 3-8)
a.) 3.0 cm; b.) 5.5 cm; c.) 8.0 cm

When using TiO_2 suspension to coat ϕ 93 mm planar samples, 4 meander lines and a meander distance of 40 mm were chosen to obtain a homogeneous thickness distribution over a big sample surface. For ϕ 25 mm samples one line spraying without meander was adopted.

For 316L suspensions, due to the fact that the spraying beam can be regulated large enough to cover the surface of the samples, one line spraying without meander was used.

Optimised Spraying Parameter Sets for Different Suspensions

Basing the above work on optimising the spraying parameters for the planar samples, Table 4-3 lists the optimised spraying parameter sets for different suspensions.

Table 4-3 Optimised spraying parameter sets for different suspensions

Suspensions	Nozzle [mm]	Spraying Pressure [bar]	Spraying Distance [mm]	Spraying Velocity [mm/min]	Spraying Beam [unit]	Suspension Feed Rate [unit]	Ellipse length and breadth [mm]	Meander	Multi-layer
316L SS < 16 µm	1.8	1.5	230	3500	5	35	110, 230	without	4
316L SS < 5 µm	1.8	1.5	230	3500	5	20	100, 220	without	2
TiO_2	1.8	0.5	230	3500	5	5 7	50, 120 60, 130	4 4	2 1

It must be mentioned here that the meander spraying is suitable for large-surface specimens, e.g. ϕ 93 mm; for ϕ 25 mm samples only one line spraying without meander can satisfy the requirement.

Comparing the experimental thickness distribution with the real filter layers

In order to verify if the experimental data of the thickness distribution measured on transparencies were in accordance with the real filter layer on a porous substrate, a comparison was done. Table 4-4 lists the experimental diagrams and the estimated layer thickness of one ϕ 56 mm sample.

Table 4-4 Estimation of the sprayed layer thickness of different suspensions*

Suspensions	Thickness distribution diagrams	Estimated thickness [µm]
316L (particle size < 16 µm) Parameter set: N=1.8 P=1.5 D=230 V=3500 SB=5 SA=35	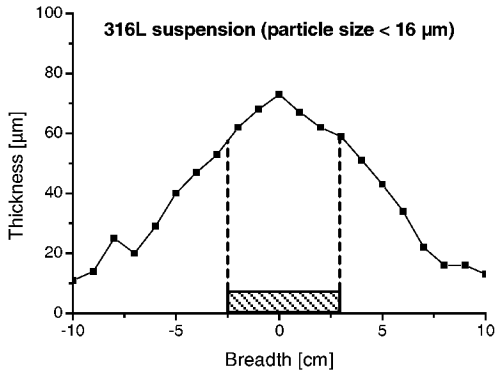	4 multi-layers 240 ~ 280

316L (particle size < 5 μm) Parameter set: N=1.8 P=1.5 D=230 V=3500 SB=5 SA=20	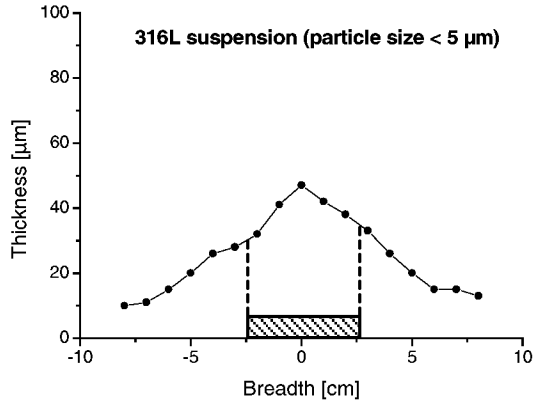	2 multi-layers 100 ~ 120
TiO_2 Parameter set: N=1.8 P=0.5 D=230 V=3500 SB=5 Meander=2 MD*=4 mm	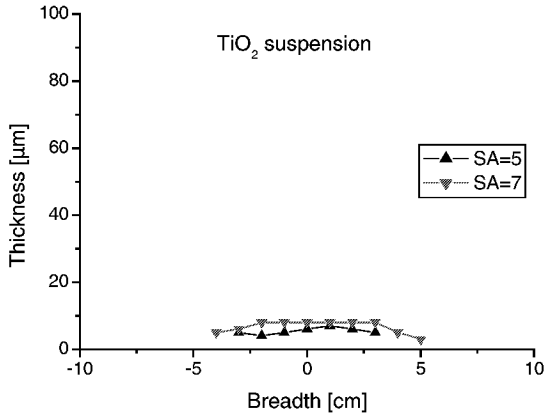	3 multi-layers 20 ~ 30

* The thickness in the diagrams was measured by 1 meander and 1 line; MD means meander distance.

Fig. 4-24 shows the cross section structure of the sample, on which the thickness of each layer is marked.

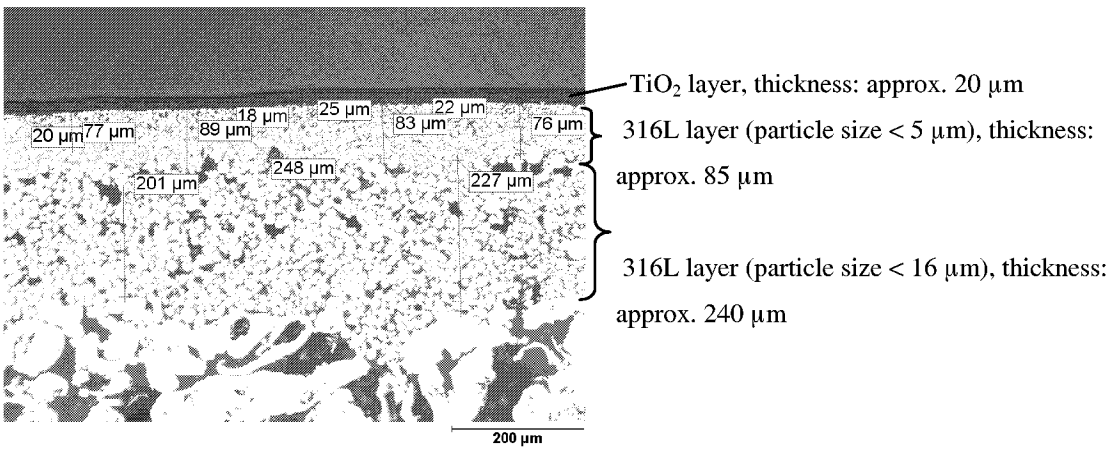

Fig. 4-24 Cross section of one ϕ 56 mm planar sample, the measured thickness of each layer is marked

Comparing the thickness listed in Table 4-4 and Fig. 4-24 it is known that there exist deviations between the estimated and measured values to some extent. There are two possible reasons except the measurement errors: one is the shrinkage of the layer during the sintering process, the other is due to the uneven surface of the support and the adsorption of particles from the support pores, which forms a interface between two layers as those shown in Fig. 4-25 a.) to c.).

Based on the above comparison and analyses it can be deduced that the thickness measurements onto transparencies are quite reliable, which can give a predict of the layer thickness even during the spraying process.

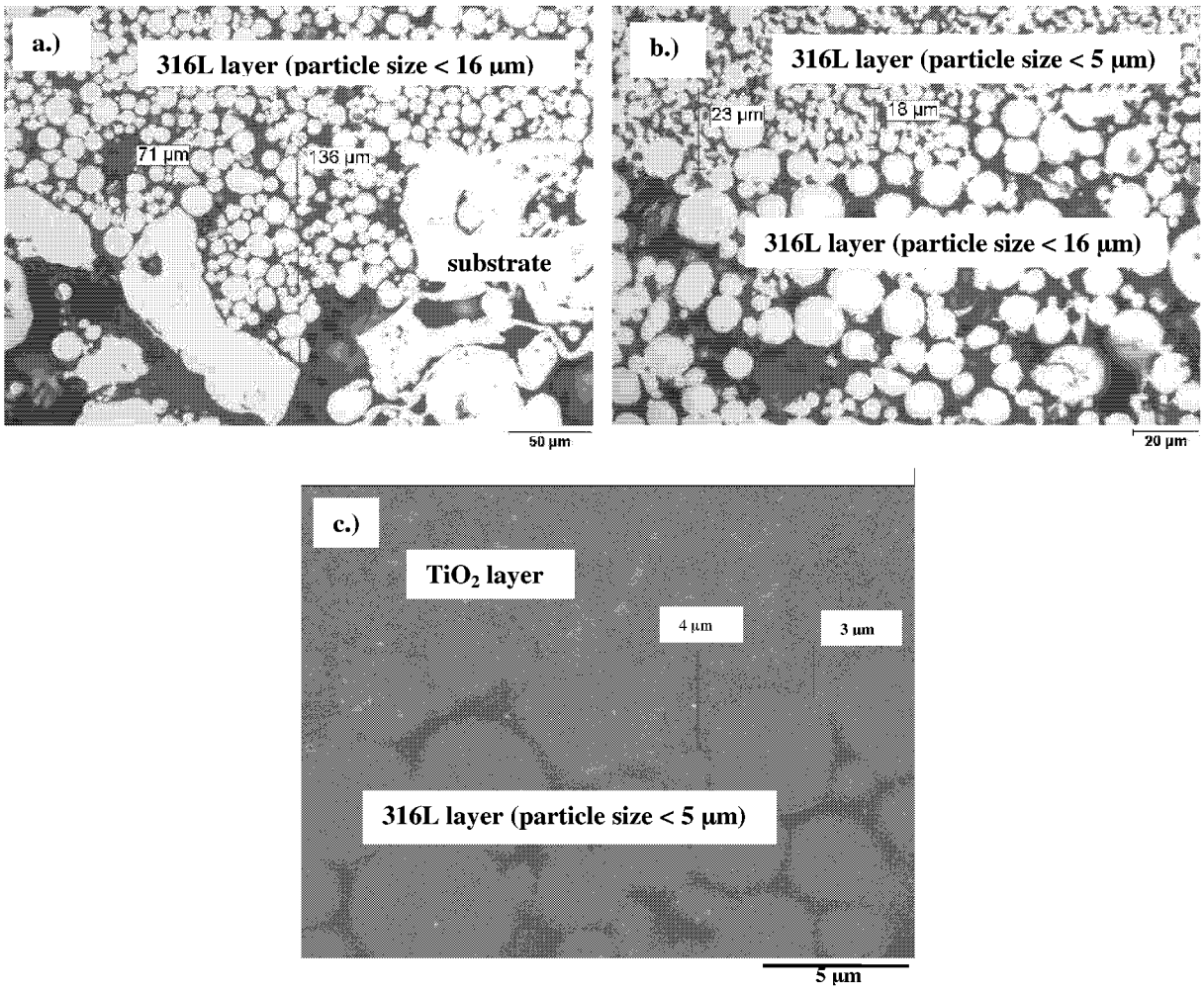

Fig. 4-25 Interlayers structure a.) Interlayer between the substrate and the 316L layer (particle size < 16 µm); b.) Interlayer between the 316L (particle size < 16 µm) and (particle size < 5µm) layers; c.) Interlayer between the 316L (particle size < 5 µm) and TiO_2 layers

4.2.2 Investigating the Influences on the Thickness of Tubular Application

As told in the experimental part, for tubular samples, the optimisation of the spraying parameters should be concentrated on how to match the spraying speed of the spraying gun and the rotation speed of the samples, then the stripes due to the unfitness of these two speeds can be avoided, which is also an important indication if a well-coated layer has been obtained or not.

According to the spraying experience acquired from planar specimens a correlation between the moving speed and the rotation speed was obtained. The optimal moving speed and rotation speed are listed in Table 4-5.

Table 4-5 Optimised spraying speed for tubular samples

Layer	Moving speed of the gun V_G [mm/min]	Rotation speed of the tubes ω_R [1/min]
316L (particle size < 16 μm)	480	120
316L (particle size < 5 μm)	750	110
TiO_2	1200	152

Because the outside diameter of the applied tube-substrate is quite small, meander is unnecessary in this case, only one line spraying is used; furthermore, a flexibility in controlling the thickness should be realised through a multi-layer spraying mode. Table 4-6 lists the optimised spraying parameters for tubular samples.

Table 4-6 Optimised spraying parameter sets for different layers of tubular samples

Layers	Nozzle [mm]	Spraying Pressure [bar]	Spraying Distance [mm]	Spraying Beam [unit]	Suspension Feed Rate [unit]	Ellipse length „W“ [mm]	Ellipse breadth [mm]
316L (particle size < 16 μm)	1.8	1.5	160	3	8	60	80
316L (particle size < 5 μm)	1.8	1.5	160	3	7	65	80
TiO_2	1.8	0.5	220	5	7	60	120

The next key factor is how many multi-layers should be. For tubular specimens the thickness can not be optimised on transparencies; a metallurgical method must be used. Fig. 4-26 a.) to c.) list the cross section structure of the samples with 3, 5 and 7 multi-layers of TiO_2. Due to the measurement results it can be calculated that the thickness of each spraying layer is approx. 7~8 μm. The required layer thickness should be in the range of 20 μm. So for TiO_2 3 layer numbers was adopted.

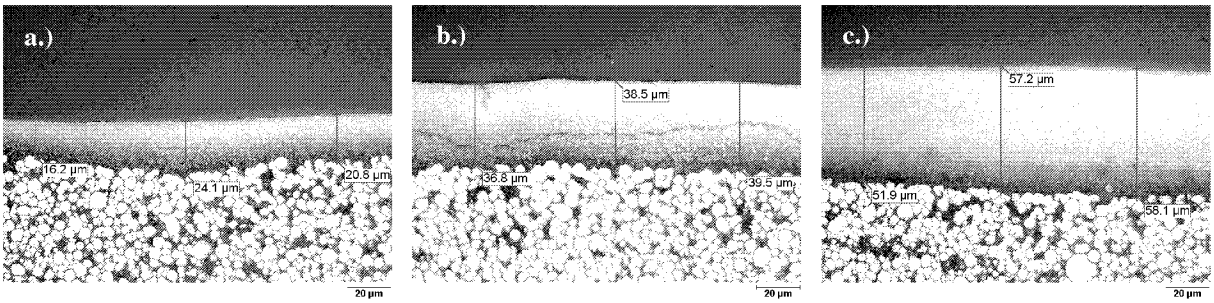

Fig. 4-26 Cross section structures of the sprayed TiO_2 layer of the tubular samples
a.) 3 multi-layers; b.) 5 multi-layers; c.) 7 multi-layers.

The same experiments of the 316L (particle size < 16 µm and particle size < 5 µm) layers were also done, the thickness of only one spraying line of each layer was 80 µm and 50 µm separately. Due to the high roughness of the substrate the 316L (particle size < 16 µm) layer should be sprayed at least 3 multi-layers to cover the rough surface. 2 multi-layers for 316L SS < 5µm layer were enough.

A surface structure of one sample coated with the optimised suspension and spraying parameters is shown in Fig. 4-27. Comparing with the sample shown in Fig. 4-1, the surface quality has been improved evidently.

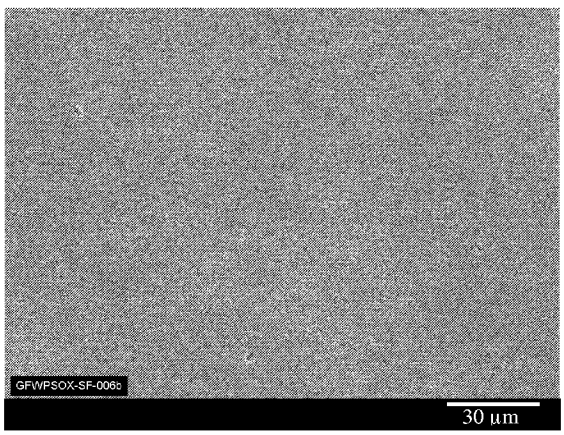

Nozzle:	1.8 mm
Pressure:	0.5 bar
Distance:	230 mm
Velocity:	3500 mm/min
Spraying Beam:	5 units
Suspension feed rate:	7 units
Meander:	1 line
Layers:	3

Fig. 4-27 SEM image of the surface structure of one planar sample with optimised suspension and spraying parameters, × 1000

4.3 Optimisation of the Sintering Process

The sintering temperature is very important for the filter membranes. The sintering necks between the particles form the pores of the filter media. Two cofiring routes were tested. For the route 1, the cofiring between the 316L (particle size < 5 µm) and TiO_2 layers was given up due to the poor surface quality — some parts of the TiO_2 layer flaked off after sintering. Then only cofiring between the two 316L intermediate layers was investigated in detail. Fig. 4-28 a.) to c.) and Fig. 4-29 a.) to d.) show the different surface structures of these two layers at different sintering temperatures.

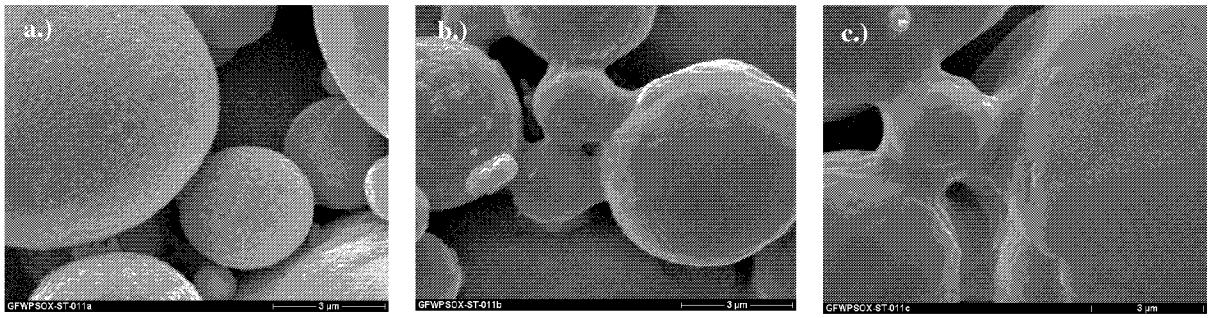

Fig. 4-28 Surface structure of the 316L (particle size < 16 μm) layer at different sintering temperatures
a.) 800°C; b.) 900°C; c.) 1000°C

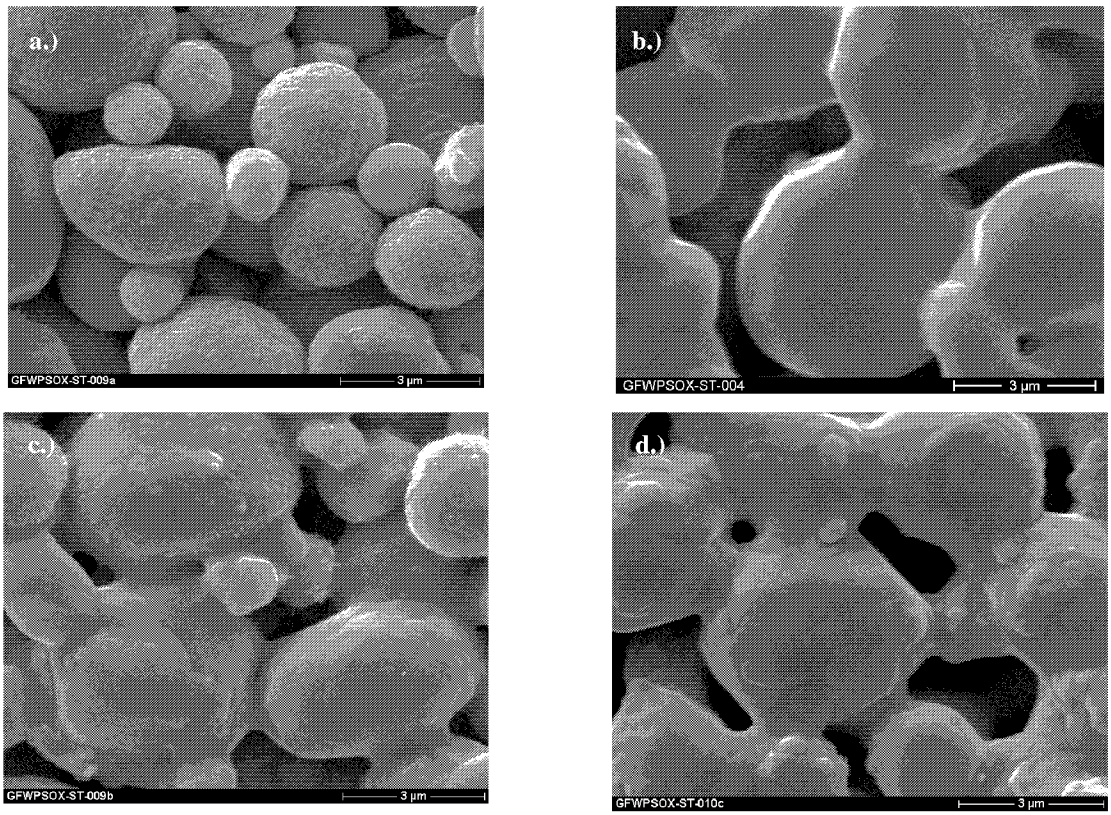

Fig. 4-29 Surface structure of the 316L (particle size < 5 μm) layer at different sintering temperatures
a.) 800°C; b.) 850°C; c.) 900°C; d.) 1000°C

It is obvious that at 800°C there are no sintering necks, the particles are separated without fusion, i.e. this temperature is too low for 316L stainless steel powders; at 850°C there appear the sintering necks between 316L particles; the bonding between particles is strengthened as the temperature is increased to 900°C for both the two powders; at 1000°C, a strong reduction of porosity can be observed for both steel powders from Fig. 4-28 c.) and Fig. 4-29 d.). Especially for 316L particle size < 5 μm layer the sintering temperature of 1000°C was found to be too high.

According to the SEM images shown in Fig. 4-28 and Fig. 4-29 an optimum sintering temperature for the steel powders can be obtained, for the powder with particle size < 16 μm

it should be in the range of 900~1000°C, and for the powder with the particle size < 5 μm it should be in the range of 850~900°C. Then the cofiring temperature was chosen as 900°C for these two layers.

The same analyses of the TiO_2 layer were also made. The different surfaces of the layer at different sintering temperatures from 800°C to 950°C are shown in Fig. 4-30 a.) to d.) at 50°C intervals. Basing these pictures the sintering temperature of the TiO_2 layer should be in the range of 900~950°C. 950°C were chosen for sintering the TiO_2 layer due to the consideration that a higher sintering temperature of the TiO_2 layer (900°C of interlayer), a post-sintering of the steel interlayer occurs, which leads to a compression stress exerting on TiO_2 layer. This is advantageous to avoid crack formation during sintering and enhance the adhesive strength of the TiO_2 layer.

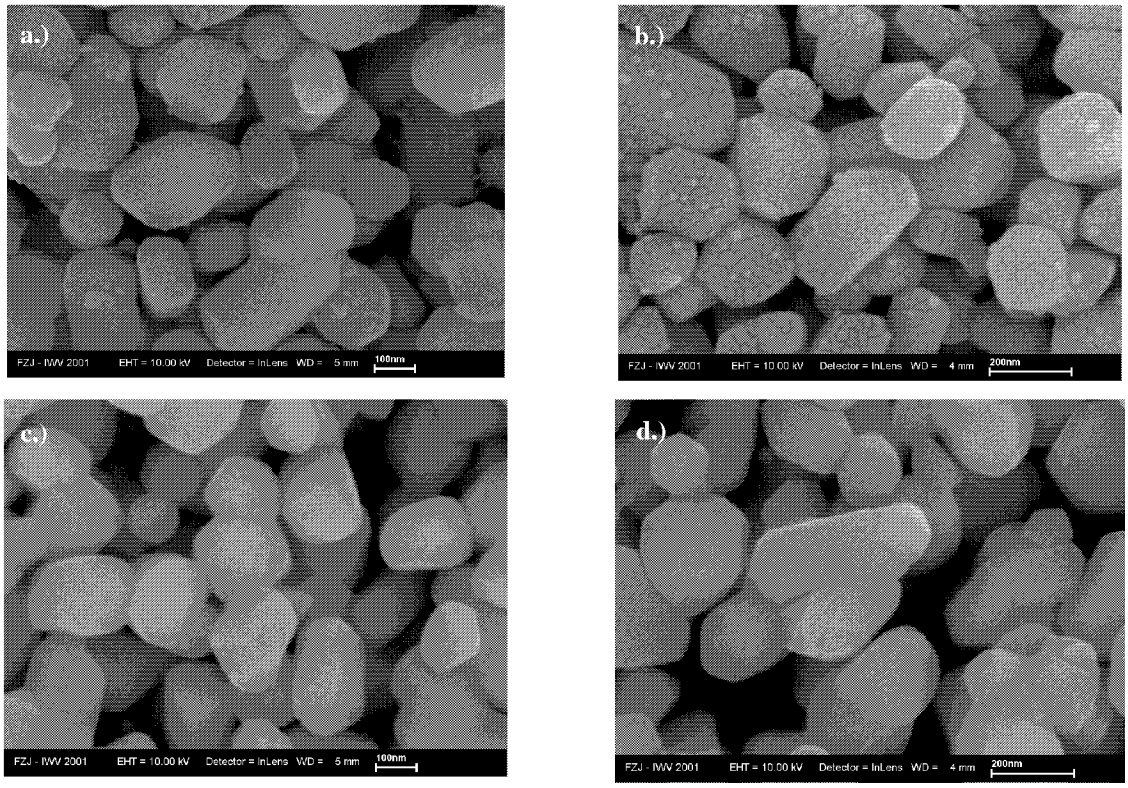

Fig. 4-30 Surface structure of the TiO_2 layer at different sintering temperatures
a.) 800°C; b.) 850°C; c.) 900°C; d.) 950°C

4.4 XRD Measurement

The samples, whose intermediate layers were cofired at 900°C, 1h and functional TiO_2 layer was sintered at different temperatures in the range of 800~950°C, were measured by XRD (X-ray diffraction). The measurement results are shown in Fig. 4-31.

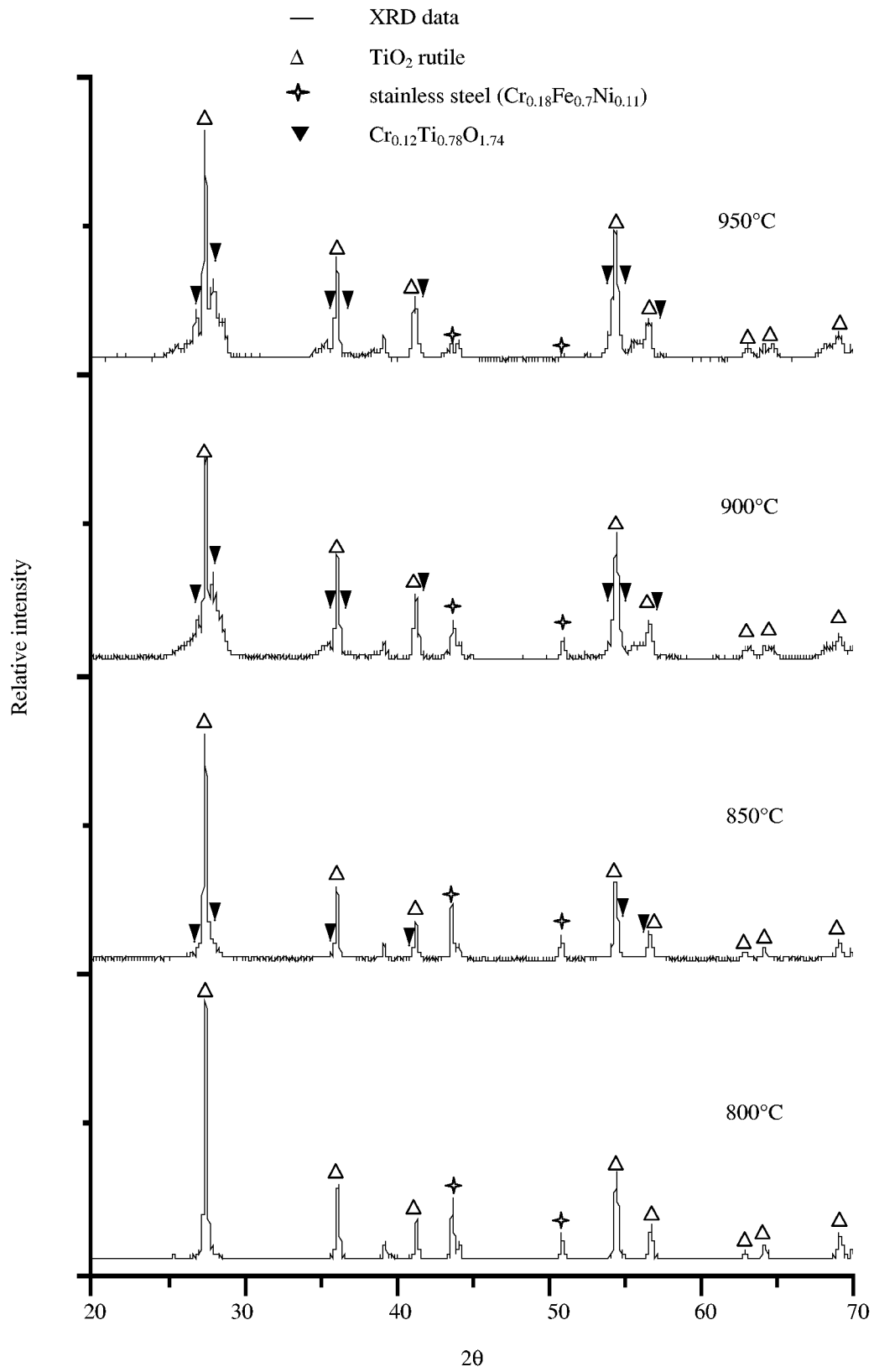

Fig. 4-31 XRD measurement results for the probes sintered at different temperatures

Comparing these four specimens it is obvious that at 800°C there is no reaction between the TiO_2 and the substrate material; at 850°C, through the formation of a new phase ($Cr_{0.12}Ti_{0.78}O_{1.74}$) at a quite low level, it indicates that the reaction between the TiO_2 layer and 316L stainless steel substrate starts slowly; with increasing the temperature to 900~950°C, the new phase appears intensively.

The colour of the 316L layers is grey, before and after sintering there is no great change. For TiO_2 layer, the colour of the green body is white, after sintering onto 316L support, the colour is changed to dark blue. The probable reason is the appearance of the new phase $Cr_{0.12}Ti_{0.78}O_{1.74}$.

4.5 Characterisation of the Graded Filter Structure

4.5.1 Pore Size Distribution

The bubble-point test was used to measure the pore size distribution of the samples.

Fig. 4-32 a.) to c.) show the pore size distribution of the intermediate layers (in fact, the pore size distribution of the 316L (particle size < 5 μm) layer) with the variation of the sintering temperatures. MFP is the average pore size in the measurement. The overlapping lines in the diagrams represent the measurement results of different probes.

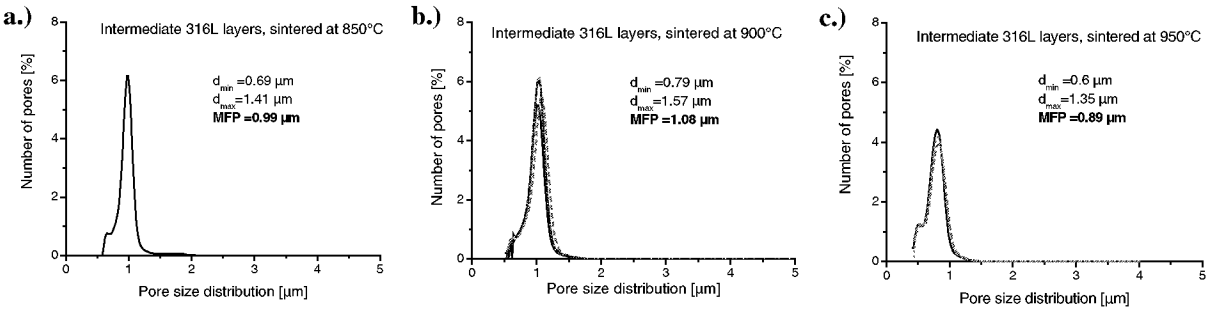

Fig. 4-32 Pore size distribution of the intermediate layers changing with the sintering temperature
a.) 850°C, 1h; b.) 900°C, 1h; c.) 950°C, 1h

With varying the sintering temperature the average pore size (MFP) value is changed. It is known from the results that at 900°C, the average pore size of the cofired intermediate layers is 1.08 μm, which is a little bit greater than that of the layer sintered by 850°C (0.99 μm) and 950°C (0.89 μm). This unexpected result can be probably explained by the experimental deviation of the bubble-point equipment and needs further investigation.

More samples were produced and the pore sizes were measured, the average pore size (MFP) of samples with different sintering temperatures showed another tendency — MFP by 900°C

(0.72 µm) < MFP by 850°C (0.75 µm) < MFP by 950°C (0.84 µm). The probable reason for the deviation then can be deduced that the tiny difference can not be detected by this measuring method.

The correlation between the pore size distribution and the sintering temperature of the TiO_2 layer is shown in Fig. 4-33 a.) and b.). With increasing the sintering temperature of 50°C the

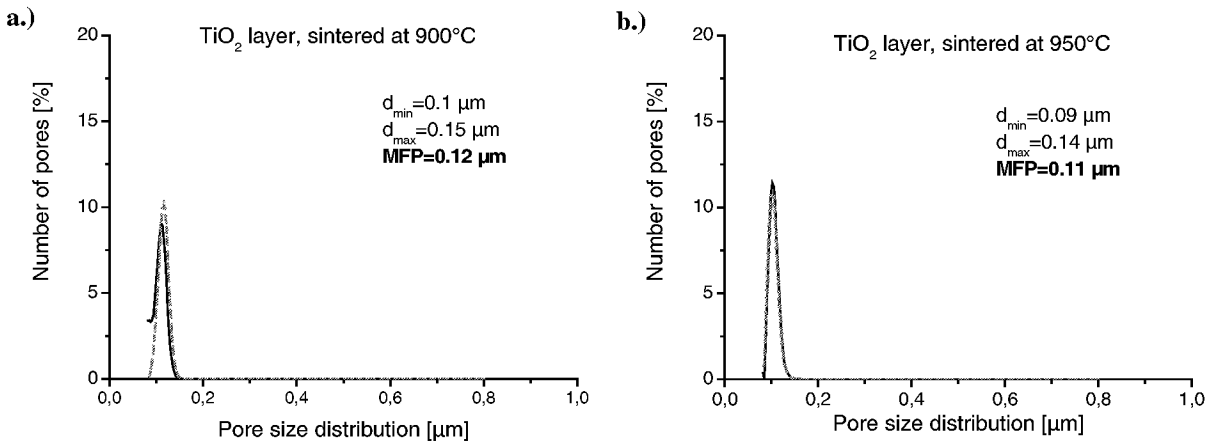

Fig. 4-33 Pore size distribution of TiO_2 layer changing with the sintering temperature
a.) 900°C, 1h; b.) 950°C, 1h

average pore size (MFP) is decreased 0.01 µm. For the further attempts a sintering temperature of 950°C, 1h was chosen for the TiO_2 layer.

4.5.2 Permeability

The flow rate of different filter structures was measured to evaluate the permeability of it. Fig. 4-34 a.), c.) and e.) show the cross section of planar samples with increasing gradual layers, whose flow rate measurement results by air (20°C, 1 atm) are given in the diagrams in Fig. 4-34 b.), d.) and f.) separately. Due to the technical complexity for water test the produced samples were measured mostly by air.

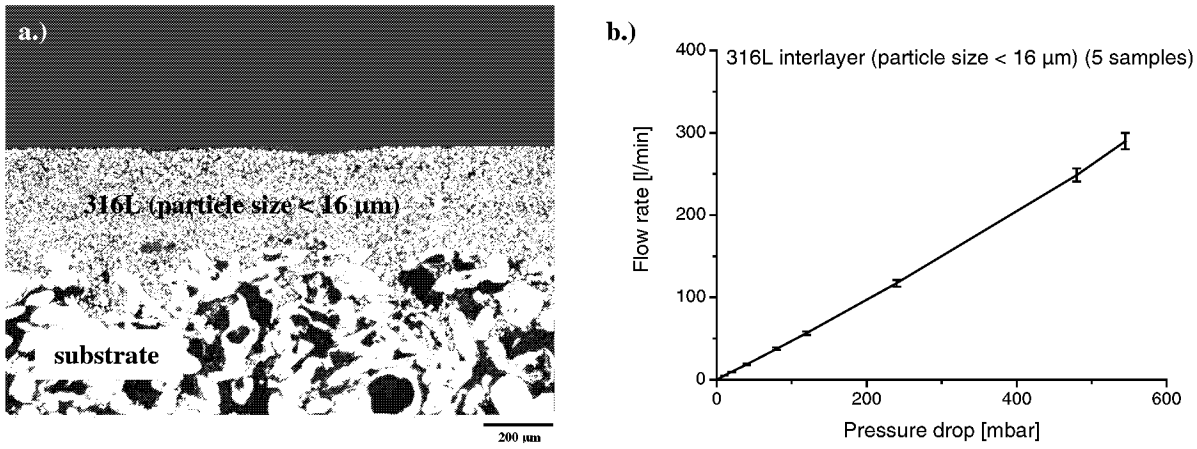

a.) Microstructure of the sample with 316L interlayer (particle size < 16 µm); b.) Flow rate measurement results

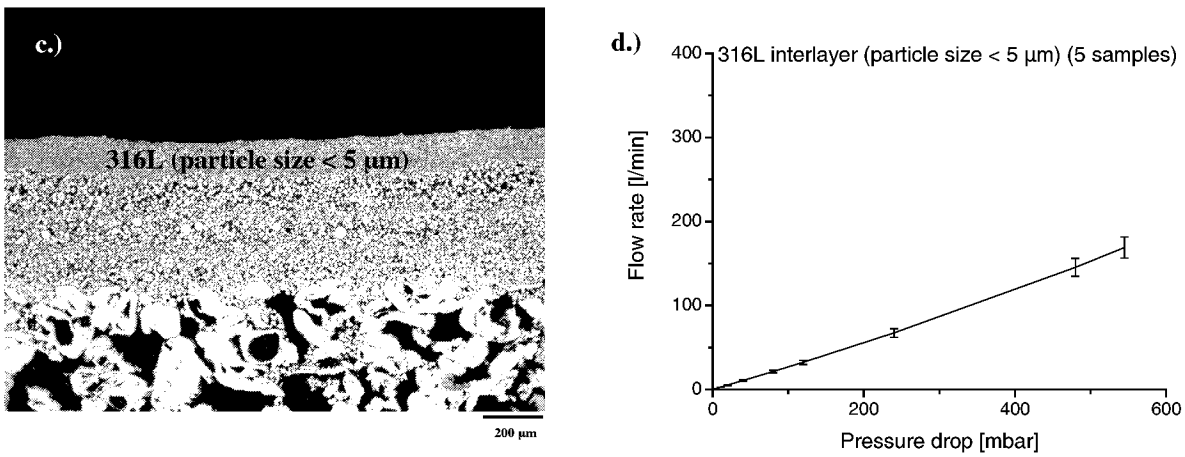

c.) Microstructure of the sample with 316L interlayer (particle size < 5 µm); d.) Flow rate measurement results

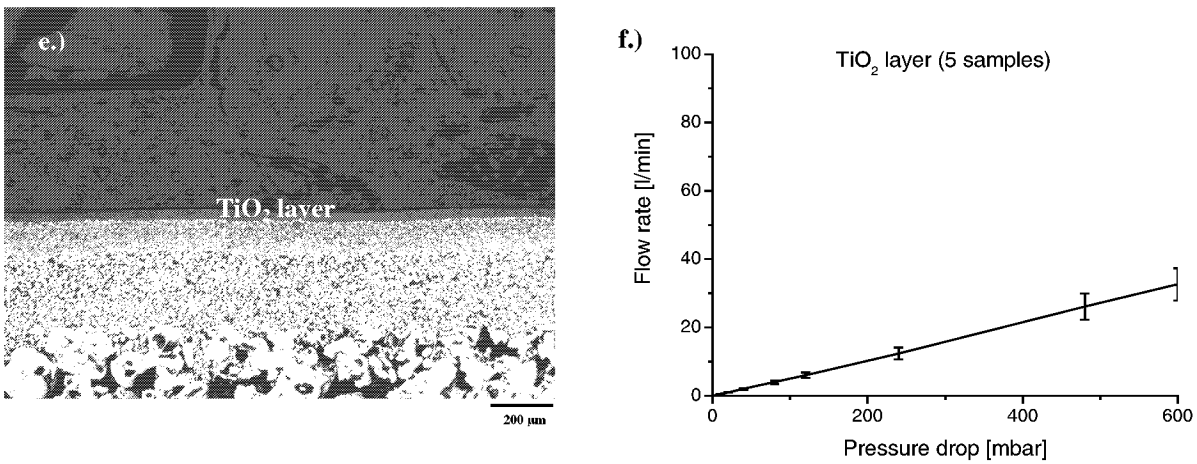

e.) Microstructure of the sample with TiO_2 layer; f.) Flow rate measurement results

Fig. 4-34 Cross section of planar samples and flow rate measurement results of the graded samples
Thickness of different layers: TiO_2 layer — 30 µm, 316L layer (particle size < 5µm) — 90 µm, 316L layer (particle size < 16 µm) — 300 µm, substrate — 3mm;
measured by air at 20°C, 1 atm, measured area: 5153 mm^2

It has been found in the experiments that the thickness of the measured layer has a great influence on the flow rate of the filters. With decreasing the thickness of the measured layer the flow rate of the graded structure can be increased. These results are shown in Fig. 4-35 a.) for TiO_2 layer and b.) for 316L (particle size < 5 μm) layer.

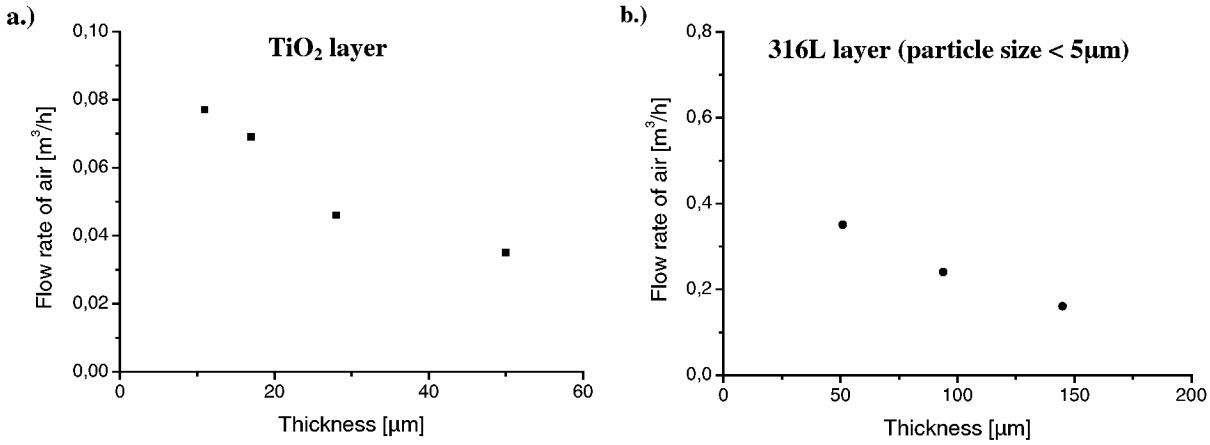

Fig. 4-35 Correlation between the flow rate and thickness of the functional layer
a.) TiO_2 layer; b.) 316L (particle size < 5 μm) layer
measured by air at 20°C, 1 atm, ΔP= 600 mbar, measured area 177 mm^2 (ϕ 15 mm) onto ϕ 25 mm samples

So the thickness of the functional layer should be kept as low as possible considering that a sufficient quality and strength exists.

A comparison between TAMI commercial products and the filter membrane produced in FZJ was done due to the fact that the TAMI composite filter membranes with nominal pore sizes of 0.14 μm and 0.20 μm have a similar design — a TiO_2 layer (particle size in the range of 0.3 μm) onto a porous Al_2O_3 substrate. The results are listed in Table 4-7. The experiments were carried out on ϕ 25 mm samples, by air at 20°C, 1 atm, and the pressure drop was 600 mbar.

Table 4-7 Comparison between TAMI products and the samples produced in FZJ

Samples	Smallest pore [μm]	MFP [μm]	Largest pore [μm]	Thickness [μm]	Flow rate of air [l/min]
TAMI 0.14 μm	0.0487	**0.0681**	0.1456	**4**	**1.0**
TAMI 0.20 μm	0.0465	**0.0524**	0.0975	**7**	**0.83**
TAMI 0.45 μm	0.0639	**0.1338**	0.3902	**31**	**1.09**
TAMI 0.80 μm	0.0639	**0.1639**	0.4808	**18**	**1.34**
FZJ TiO_2	0.094	**0.117**	0.147	**25**	**1.17**
FZJ 316L < 5μm	0.763	**1.075**	1.607	**90**	**5.88**

The thickness in Table 4-7 is pointed to the thickness of the functional layer. It is obvious that the FZJ membranes has a higher flow rate than the TAMI 0.14 μm and 0.20 μm membranes even the thickness of it is quite higher that of TAMI's products. With regards to the lower pore size of the TiO_2 layer of TAMI products it can be deduced that the higher sintering temperature is adopted by TAMI.

4.5.3 Mechanical Stability

5 pieces ϕ 93 mm samples took the strength test. Except the deformation of the samples as shown in Fig. 4-36 there observed no flake-off of the coated TiO_2 layer by naked eyes. The reason of the curvature is because of the low E-module of the coarse structure.

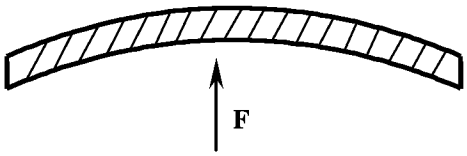

Fig. 4-36 Deformation of the samples by the stability test

All samples could withstand the test for more than 30000 cycles. A bubble-point test was done to detect failures of the samples after the stability test. There found crack formation on one sample, which was exerted over 50000 cycles during the stability test. The SEM images of the fracture are shown in Fig. 4-37 a.) to b.). A subsequent test on a second sample shows that the samples can withstand for more than 1 million cycles without failure.

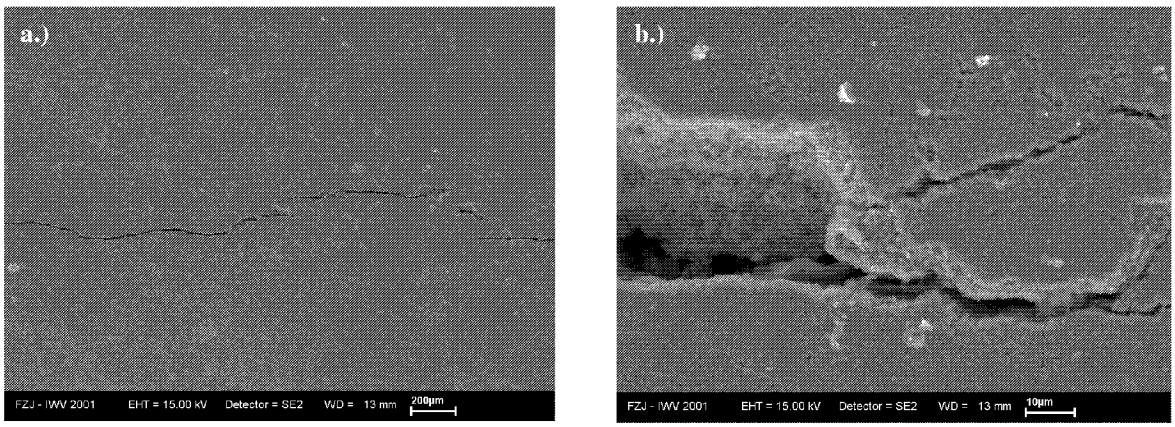

Fig. 4-37 Surface structure of the crack detected by the bubble-point test

4.5.4 Chemical Resistance

During the steam sterilisation experiment the specimens were wrapped with a aluminium foil. After the test, some grey adhesion on the surface was observed, which was investigated by EDX analysis and proved as aluminium shown in Fig. 4-38. It can be inferred that the adhesion was the residue of the aluminium foil onto the surface. No obvious damage of the TiO_2 layer can be detected even there occurred a corrosion attack on the steel substrate. One

reason for the loss of the corrosion resistance of the substrate could be a Cr-depletion during the vacuum sintering process.

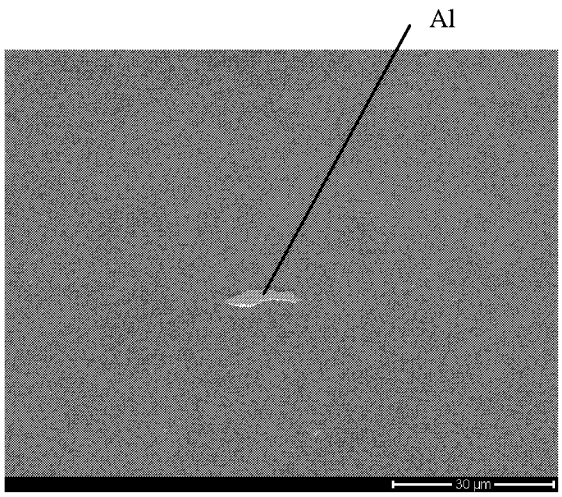

Fig. 4-38 Residue of the aluminium foil onto the layer surface

4.6 Failures and measures to avoid them

4.6.1 Description of the Problems

Except the agglomerates talked above, the „Spherical pores" shown in Fig. 4-39 a.) and b.) are typical problems observed in the graded structure both for planar and tubular specimens. Normally this failure exists only in the intermediate layers. When these spherical pores emerge on the surface of the 316L (particle size < 5 µm) layer, they lead to coating failures in

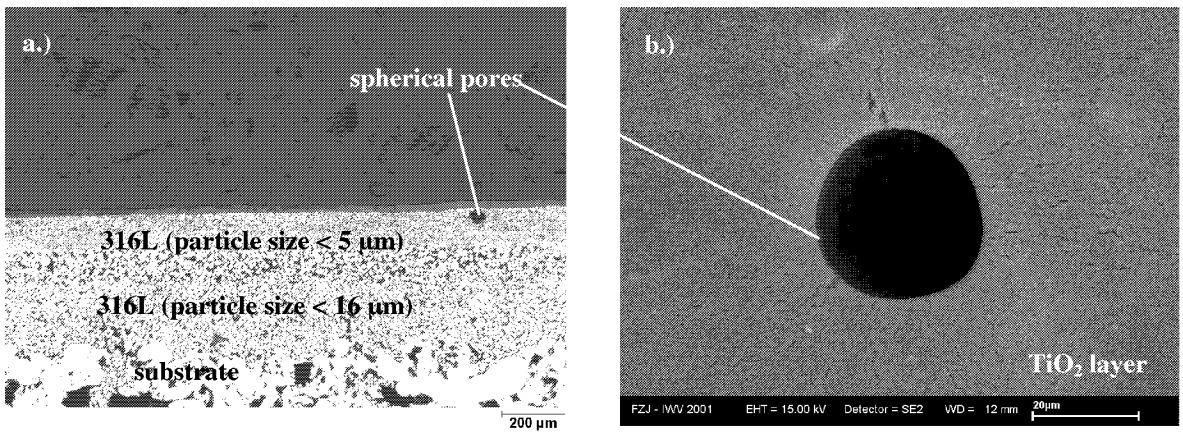

Fig. 4-39 Spherical pores a.) cross section structure; b.) surface structure

the applied TiO_2 layer, because the tiny TiO_2 particles and the thinner layer can not cover these imperfections from the support. The uncovered big pores (by some literatures, called „pinholes") in the TiO_2 layer can be detected by the bubble-point test as told in the section 3.5.

4.6.2 Some Theoretical Explanation

Due to the characteristics of the porous media most of them are capillary systems. In the case of a capillary systems, mechanical equilibrium is determined not only by the hydrostatic pressure and gravitational attraction but also by forces associated with surface tension [59, 87]. During the coating process capillary action plays an important role in the formation of the layers. In order to look for the source of the failures of the coatings an investigation of capillary phenomena was done.

Capillary Equilibrium in Three-Phase Systems

Capillary systems in porous media always involve a solid phase and at least two fluid phases (liquid-liquid or gas-liquid). Considering that a drop of liquid placed on a smooth, plain solid surface as shown in Fig. 4-40 [122].

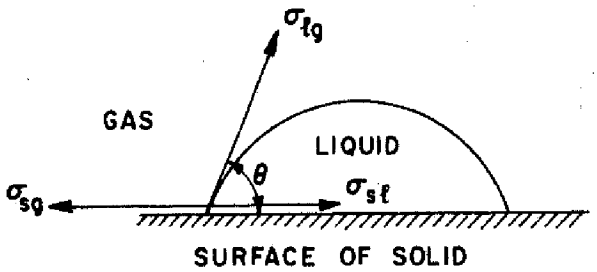

Fig. 4-40 Equilibrium at a line of contact [122]

Depending on the conditions that will be discussed below, liquid may remain a drop displaying a finite angle of contact θ between the two boundaries: liquid/gas and solid/liquid. The contact angle θ is defined as the angle subtended by the tangent to the liquid/gas boundary constructed at a point on the three-phase line of contact and the tangent to the solid/liquid boundary constructed at the same point. Due to the law of Neumann's triangle, for the force components parallel to the solid surface one obtains

$$\sigma_{lg} \cos\theta = \sigma_{sg} - \sigma_{sl} \tag{4.6.1}$$

where σ_{lg} and σ_{sg} are the surface tensions of liquid and solid, respectively, and σ_{sl} is the interfacial tension between the liquid and the solid. This equation was first given by Young for a liquid drop resting on a solid surface in air and relates the contact angle with the surface tensions of three interfaces.

After reaching mechanical equilibrium, the liquid through which $0° \leq \theta < 90°$ is usually referred to as the (preferentially) wetting liquid and the other one, through which $90° \leq \theta < 180°$, as the nonwetting liquid. Logically, the special case $\theta = 90°$ would correspond to

„intermediate or neutral wettability". In the case of two liquids in contact with a solid surface, there are also instances when one of the liquids spreads on the solid and denies the other liquid any access to the solid.

For a rough surface, Wenzel [123, 124] has suggested a modified form of Young's equation.

$$\sigma_{lg} \cos\theta_a = r(\sigma_{sg} - \sigma_{sl}) \tag{4.6.2}$$

where θ_a is the average „apparent" contact angle and r is the ratio of the true-to-apparent area of the solid. The observed angle between the liquid-gas surface and the apparent surface of the solid will then vary with the position of the line of contact as shown schematically in Fig. 4-41 [125].

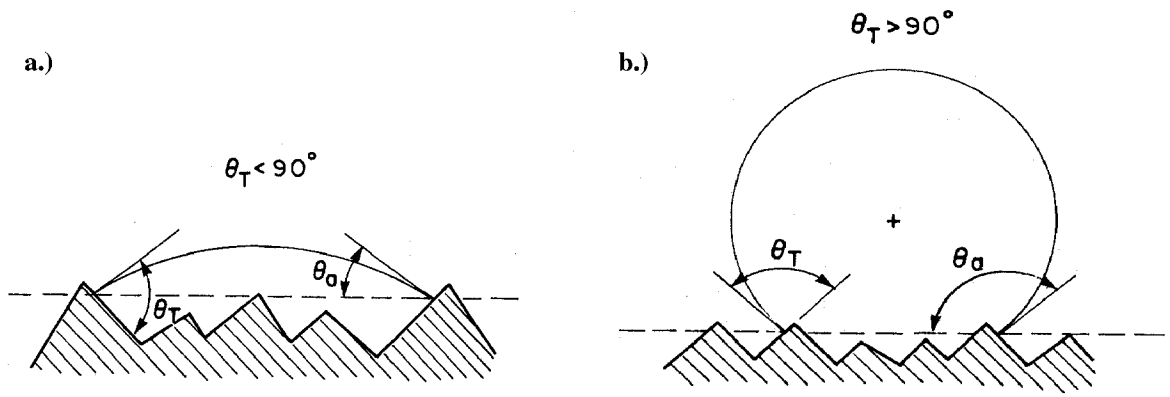

Fig. 4-41 Effects of surface roughness on apparent contact angle θ_a. θ_T is the contact angle measured on a smooth, flat surface. a.) The droplet is the preferentially wetting fluid, so $\theta_T < 90°$; b.) The droplet is the nonwetting fluid, so $\theta_T > 90°$ [125].

Capillary Pressure

Capillary pressure is a basic parameter in the study of the behaviour of porous media containing two or more immiscible fluid phases. It relates the pressures in the two fluid phases.

Considering a single circular capillary (pore) with variations in its cross section as shown in Fig. 4-42, the capillary was filled with wetting fluid (′, for example water) and subsequently it

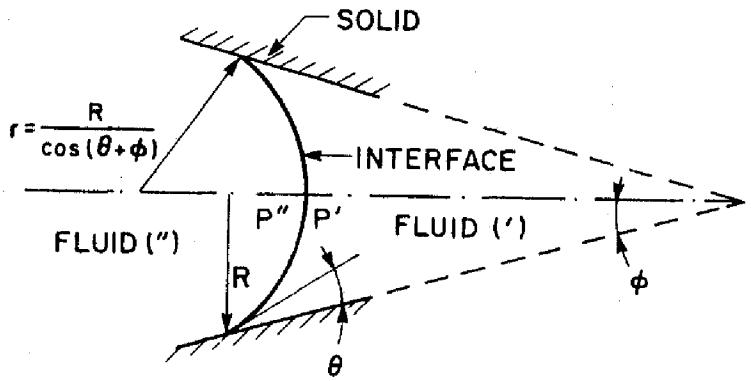

Fig. 4-42 Meniscus in a conical capillary

was connected to a nonwetting fluid (″, for example air) at atmospheric pressure. Assuming that the pressure inside the wetting liquid is also atmospheric, the nonwetting fluid will not spontaneously penetrate and displace the wetting fluid. In order to achieve any penetration, the pressure in the nonwetting fluid has to be increased above atmospheric pressure to a value defined by the following deformed Laplace's equation:

$$P_c = P'' - P' = (2\sigma / R)\left|\cos(\theta + \phi)\right| \qquad (4.6.3)$$

the geometry of the meniscus is shown in Fig. 4-41. $r=R/\left|cos(\theta+\phi)\right|$ is the mean radius of curvature of the meniscus. The effect of the orientation of the solid surfaces, expressed by the angle ϕ, on the radius of curvature $R/\left|cos(\theta+\phi)\right|$ may be visualised by imaging that the solid boundary lines are tilted over a wide range of values of ϕ. The penetration of a nonwetting phase takes place in the direction of decreasing pore diameter.The pressure difference between the concave and the convex sides of the meniscus is synonymous with the pressure difference between the nonwetting phase and the wetting phase, which is defined as the capillary pressure.

It also follows from Fig. 4-42 that for $\theta + \phi > 90°$ the direction of curvature of the meniscus will change. Logically, whenever the direction of curvature of meniscus changes there is also an exchange of roles of the two fluids as regards preferential wettability, which is thus seen to depend also on the orientation of the surface, as well as the intrinsic contact angle.

Wetting and De-wetting

From Fig. 4-42 it is apparent that as the applied capillary pressure is gradually increased, further penetration of the nonwettting phase into the capillary is achieved until the local minimum pore radius, that is, the pore throat, has been reached. There is a finite net force present throughout, which drives the wetting phase out. Nonequilibrium penetration will continue until the meniscus reaches a throat that is narrower than that last one. At that point the applied capillary pressure must be increased further in order to penetrate this throat, and so forth. The process in which the nonwetting phase displaces the wetting phase is usually called „drainage", „desaturation", or „de-wetting".

If the displacement process is to be carried out in the reverse direction where now the wetting phase is displacing the nonwetting phase, then the capillary pressure P_c must be decreased. With decreasing capillary pressure the meniscus will move to the left until the locally widest pore cross section, that is, the one with the greatest mean radium R, has been reached. As a result, this portion will be empty of the nonwetting phase in a nonequilibrium manner and the meniscus will keep moving to the left until an even wider pore cross section is reached.

Further occupying of the pore will take place only if the pressure applied on the nonwetting phase P_c is further reduced. This process is usually called „spontaneous imbibition" or „wetting". As shown in Fig. 4-42 the effective wettability is determined by both the contact angle θ and the orientation of the solid surface at various points of the three-phase line of contact, represented schematically by the angle ϕ.

Effect of Pore Structure on Relative Permeabilities

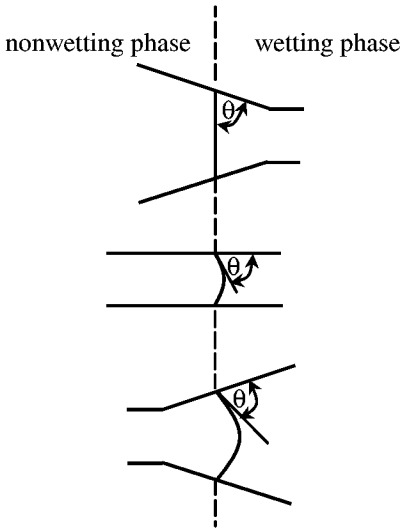

Fig. 4-43 Effect of position of meniscus in a convergent-divergent capillary tube on the value of capillary pressure

As pointed out by Melrose [126], among others, the most likely reason for the lack of spontaneous imbibition of a „wetting phase", as observed, for example, by McCaffery and Bennion [127], is the fact that the size of the cross-sectional area varies along the axis of the capillary and the surface is uneven, rough. When the contact angle in the „wetting" phase is greater than a certain critical value, the curvature of the meniscus may become zero (or negative) in a divergent capillary segment (see Fig. 4-43). The value of the critical angle is determined by pore geometry. At such a point where meniscus has zero curvature, the capillary suction becomes zero and the imbibition comes to a halt.

Applying the Capillary Theory to Our Case

Analysing the spraying process of our case: the suspension drops are sprayed onto the rough porous support. The initial process is very fast and the dry support sucks the suspension to form the interlayer. In each irregular pore of the support (original pore), there exist two fluids ‚nonwetting phase – air" and „wetting phase – carrier of the suspension", also the particles of the applied layer, which form the new smaller pores inside the original one after the evaporation of the carrier. With the control of capillary pressure there exists a pistonlike dynamical equilibrium between the wetting phase and the nonwetting phase. Influenced by the contact angle θ, the orientation of the pore surface (ϕ) and the pore diameter (R), there exist some places, in which the nonwetting phase domains the process and can not be displaced by the wetting phase, in such circumstance, the „spherical pores" come into being. This process is shown in Fig. 4-44 schematically. It should be mentioned here that this theory can explain preferentially those pores with sizes in the range of the particle diameters,

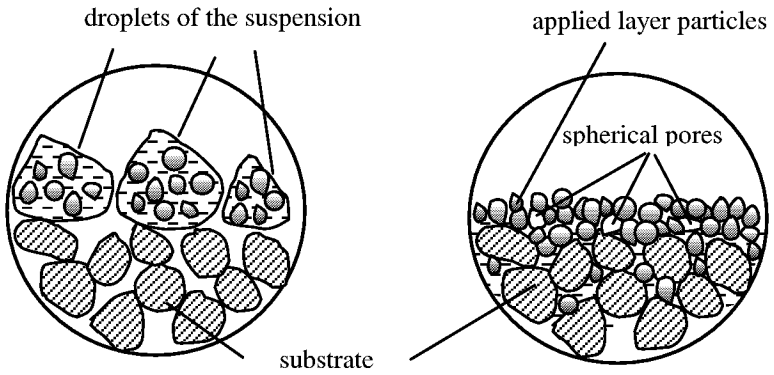

Fig. 4-44 Schematic description of the formation of the „spherical pores"

whereas, the reason for the occurrence of big failures („pinholes") in the range of 30~50 μm could not be definitely found. So the most important factors for the layer formation are the suspensions' viscosity, depending on the solid concentration, the pore size of the support, the pore size distribution of the support and the wettability of the support. According to these analyses, in the following attempts a series of measures were taken to improve the surface properties of the support and to eliminate the imperfections in the layers.

Keizer [54] gave an empirical value for coating porous ceramic membranes using sol-gel method that the initial capillary pressure should be at least 300 kPa (for water systems) to obtain a homogeneous layer. For our system, such quantitative parameter was not investigated.

Afterwards, some analyses could be put forward to explain some phenomena observed in the experiments and some measures taken to improve the quality of the coatings.

4.6.3 Measures to Avoid the Failures

Wetting the support with ethanol before spraying TiO_2 layer

According to the above theoretical analyses, for the agglomerates onto the TiO_2 layer surface (shown in Fig. 4-1) a further explanation can be drawn, i.e., the capillary driving force extracts liquid from the coating suspension into the pores of the porous support coupling with inhomogeneous layer formation.

The extraction of liquid from the coating suspension by the pores of the support can be decreased by filling the pores of the support material with a liquid, that shows a small difference in surface tension with respect to that of the carrier solvent of the suspension. Ethanol was chosen to wet the 316L interlayer before spraying TiO_2 layer. The wetting process has been standardised procedurally in the production. The spraying parameters for ethanol are listed in Table 4-8.

Table 4-8 Spraying parameters used in wetting process

Different samples	Nozzle [mm]	Spraying Pressure [bar]	Spraying Distance [mm]	Spraying Velocity [mm/min]	Rotation Velocity [1/min]	Spraying Beam [unit]	Suspension Amount [unit]	Meander	Multi-layer
planar	1.8	1.5	230	3500	-	5	15	without	2
tubular	1.8	1.5	220	1500	230	5	10	without	2

Using Ultrasonic Wave during the Spraying

There are several „spherical pores“ shown in Fig. 4-45. Observing the structure of these big pores there exists a common characteristic that big particles located on the top side of the pores. Based on the above theoretical analyses it can be estimated here that during the imbibition, because of the irregularity of the particle size, the solvent moving channel was blocked by the big particles and this can not be overcome by the gravity. Therefore, there comes such a scheme that an outside force should be exerted on the system to loose the blockage. An ultrasonic table is expected to bring such a function.

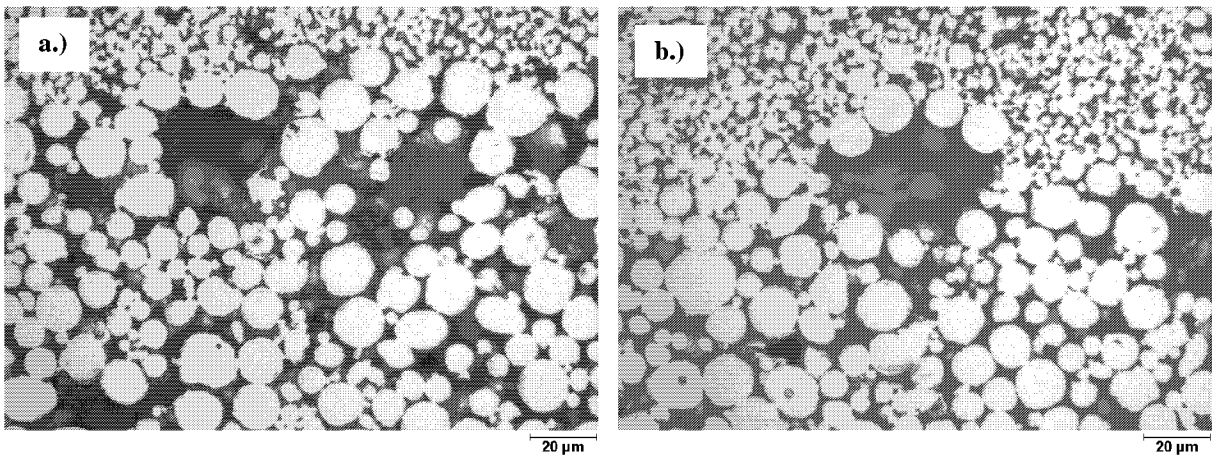

Fig. 4-45 a.); b.) spherical pores observed in the 316L (particle size < 16 µm) layer

The equipment is so designed — 2 mm thick steel plate is fixed onto an ultrasonic source, and the samples are placed onto the plate to be coated.

For ϕ 93 mm planar samples, through using an ultrasonic table, it can be observed by the bubble-point test that the failures in the TiO_2 layer caused by spherical pores in the interlayer have been decreased obviously. For the first attempt three different frequencies were tried, i. e. 1000 Hz, 10000 Hz and 25000 Hz. The different spraying surfaces are shown in Fig. 4-46 with increasing frequency. It can be seen that there exists an enhanced „neck effect“ with the increase of the frequency (Fig. 4-46 b.) to d.)).

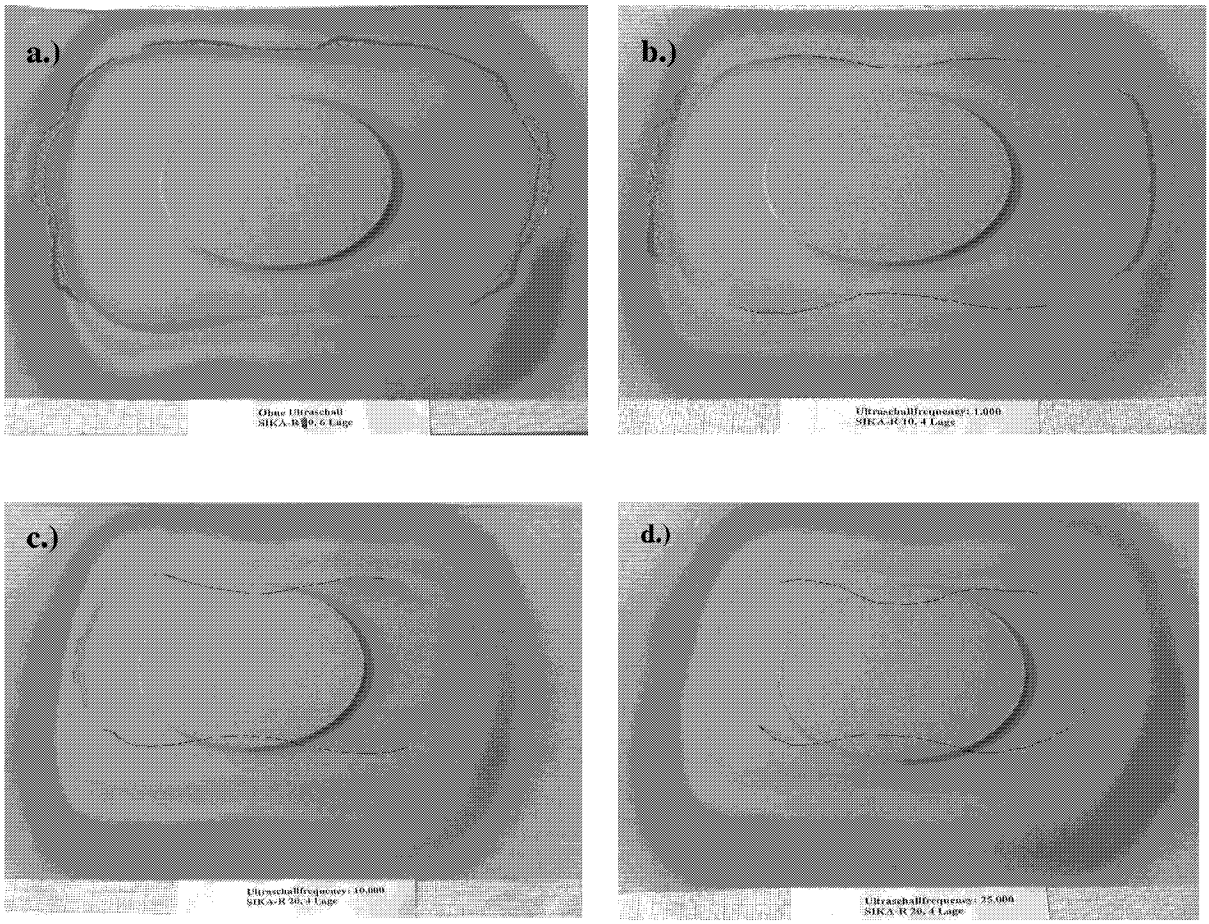

Fig. 4-46 Influence of the ultrasonic wave on the spraying surface of 316L layer (particle size < 16 μm) onto planar substrates a.) without ultrasonic; b.) with f = 1000 Hz; c.) with f = 10000 Hz; d.) with f = 25000 Hz

In the acting field of the effect on the spraying surface, an the uneven layer-thickness and coating defects probably appear. Although, it is deserved to take such measure to avoid the aforementioned defect, in respect that the advantage has been proved by bubble-point test when using 10000 Hz frequency, and the good result can be also repeated.

The bubble-point test was carried out in the pressure range of 0~2 bar. Table 4-9 gives a statistic investigation of the defects of different samples which were produced normally and with ultrasonic waves.

Table 4-9 Comparison of defects in bubble-point test
with and without ultrasonic waves

Probes	Ultrasonic frequency [Hz]	Number of the defects by different pressure [bar]				
		0.4	0.6	0.8	1.0	1.6
G3d-R2093-Kf-01b	-	20	10	*	*	*
G3d-R2093-Kf-01c	-	20	10	*	*	*
G3d-R1093-Kf-06c	-	12	6	*	*	*
G3d-R1093-Kf-06d	-	8	3	*	*	*
G3d-R2093-Ul-01	25000	6	2	2	-	-
G3d-R2093-Ul-02	10000	3	2	-	-	1
G3d-R2093-Ul-04a	10000	3	3	5	-	-
G3d-R2093-Ul-04b	10000	4	1	-	2	-
G3d-R2093-Ul-04c	10000	3	5	5	-	-

* bubbles appear steadily

For the normally produced samples, a number of bubbles can be observed at a very low pressure drop of 0.4 bar, and by 0.8~1.0 bar a regular occurrance of the bubbles appeared. That means, in the top TiO_2 layer, there exists amount of defects, whose size is much greater than the average pore size of this layer (approximate 0.1 μm). Even the ultrasonic frequency 10000 brought a quite good quality of the sample by the test, which has been reproduced by the following experiments, a complete elimination of the imperfection in TiO_2 layer was not realised.

Grinding the Surface of the Intermediate Layers

As discussed above roughness of the support surface is also a very important impact factor for the quality of the applied layer. The maximal roughness of the tubular substrates reaches even 250 μm; if the thickness of the coated layer is not greater than this value, the defects must come into being in the coated layer. Grinding the surface of substrates and interlayer was taken as an effective measure to decrease the roughness of the supports. This can be observed in Fig. 4-47: a.) shows a 316L (particle size < 16 μm) layer onto an unground substrate and b.) onto a ground substrate. The surfaces look so different due to the contrary treatments of the substrate. Grinding for substrates was done on a lathe, for two interlayer (in green state) it was done directly in the WPS equipment on the rotating samples.

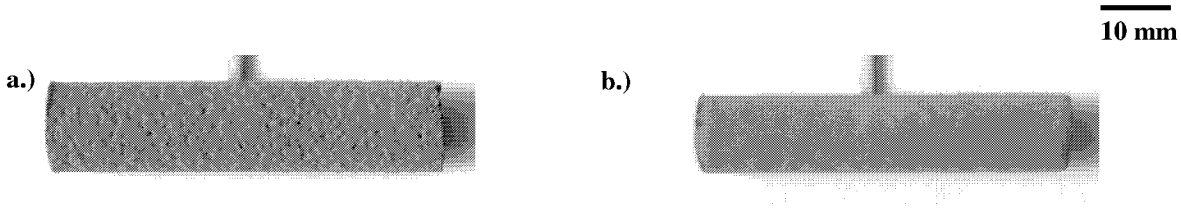

Fig. 4-47 Photographs for the probes after coating with the 316L (particle size < 16 μm) layer a.) onto unground substrate; b.) onto ground substrate

Also the grinding depth of 316L (particle size < 16 μm) layer has an influence on the applied 316L (particle size < 5 μm) layer. Fig. 4-48 a.) shows the surface of a ground 316L (particle size < 16 μm) layer, which was ground till the metallic part of the substrate can be seen; then the 316L (particle size < 5 μm) layer was coated onto this surface, whose surface structure is photographed in Fig. 4-48 b.). Obviously many failures were observed, which were brought about by the rough surface of the support, i.e., the strong extraction of capillary force from the pores of the substrate exerted on the coated suspension. So grinding of the interlayer down to the substrate should be avoided. For the two intermediate layers, an appropriate rubdown of the surface is sufficient.

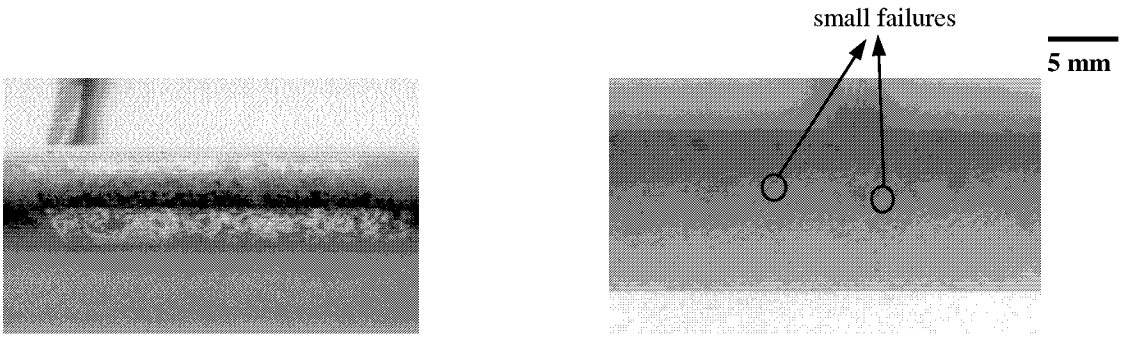

Fig. 4-48 a.) A ground 316L (particle size < 16 μm) layer; b.) A coated 316L (particle size < 5 μm) layer onto the support of a.)

Roughness was taken as a measure to control the grinding process. The different surfaces, which were ground and coated with different layers, are shown in Fig. 4-49 a.) to g.). The pertaining roughness measurement results are listed in Table 4-10.

a.) initial state of SIA-R 15 IS substrate

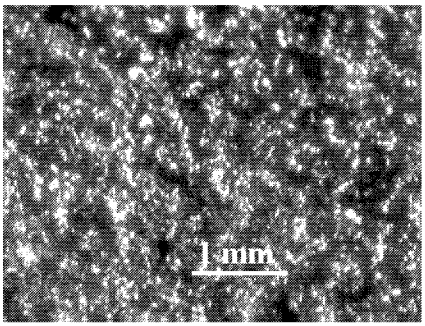

b.) surface of a gound substrate

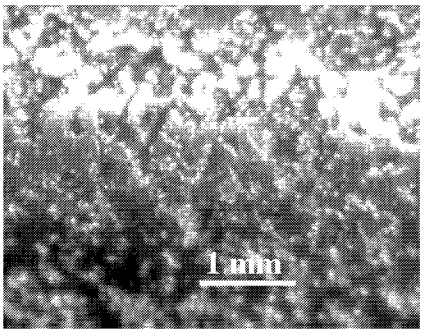

c.) a coated 316L (particle size < 16 μm) layer onto the ground substrat

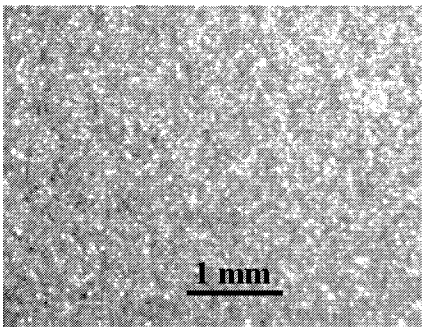

d.) surface of a ground 316L (particle size < 16 μm) layer

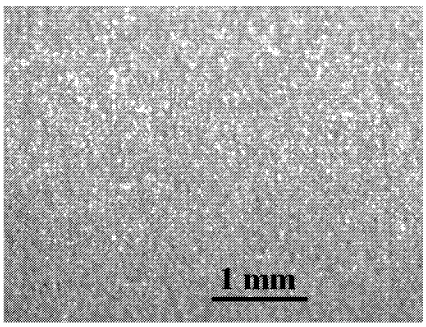

e.) a coated 316L (particle size < 5 μm) layer onto the ground < 16 μm layer

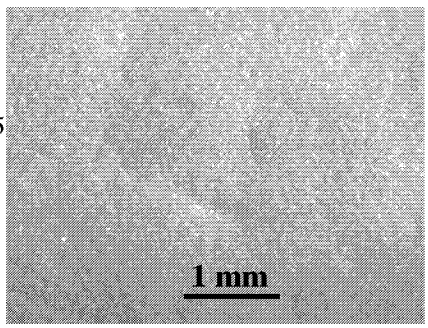

f.) surface of a ground 316L (particle size < 5 μm) layer

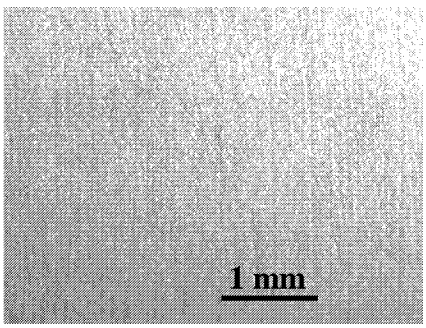

g.) a coated TiO_2 layer

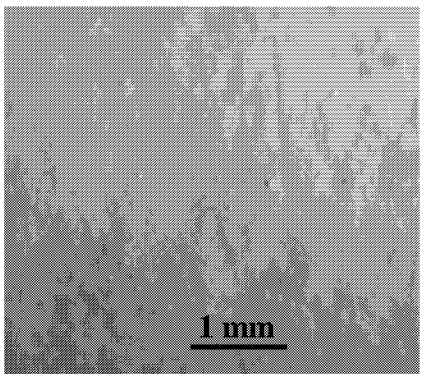

Fig. 4-49 Surface structure of different layers

Table 4-10 Surface roughness of different layers before and after grinding for tubular samples

	Treatment (size of grinding paper)	Layer thickness [μm]	R_m [μm]	R_a [μm]
Substrate Sika R 15 IS	initial state	2100	250	40
	grinding (P150, P280)	*	145	15
316L SS < 16 μm layer	as coated	~ 210	62.4	7.8
	grinding (P400, P800)	*	38.7	4.4
316L SS < 5 μm layer	as coated	~ 150	27.3	4.3
	grinding (P800, P1200)	*	21.1	1.6
TiO_2 layer	as coated	25~30	13.7	1.9

* undefined. The grinding amount should be decided by the roughness of the ground surface.

It is known from the results clearly that with coating and grinding the roughness of the surfaces is gradually decreased. By bubble-point test, even few bubbles can be also observed at a low pressure of 0.4 bar, the layer quality is quite good.

For planar substrates the same grinding process was managed to carry out on two intermediate layers. That is, after coating and completely drying, the specimens were placed onto a rotating grinding paper (316L (particle size < 16 μm) layer (P800), 316L (particle size < 5 μm) layer (P1200)), then the surface was ground. The surface roughness measurement results are listed in Table 4-11. Because the same size grinding paper was used in the last grinding step, the surface roughness of different layers keeps quite consistent both for planar and tubular probes. The reproducibility of grinding method used in planar samples is not so good as that of ultrasonic wave method. By some samples it was observed that the cavernous spherical pores were laid open after grinding.

So in the following know-how transfer, grinding was adopted for tubular samples, ultrasonic wave was used for planar samples. A photograph of samples in different geometry is shown in Fig. 4-50.

Table 4-11 Surface roughness of different layers before and after grinding for planar samples

	Treatment (size of grinding paper)	Layer thickness [μm]	R_m [μm]	R_a [μm]
Sika R 20 AX	initial state	3000	110	10
Sika R 10 AX	initial state	3000	100	10
316L particle size < 16 μm layer	as coated	~ 240	63.3	7.6
	grinding (P800)	~190	38.0	4.4
316L particle size < 5 μm layer	as coated	~ 150	33.0	5.1
	grinding (P1200)	~100	23.0	2.2
TiO_2 layer	as coated	25~30	18.4	2.1

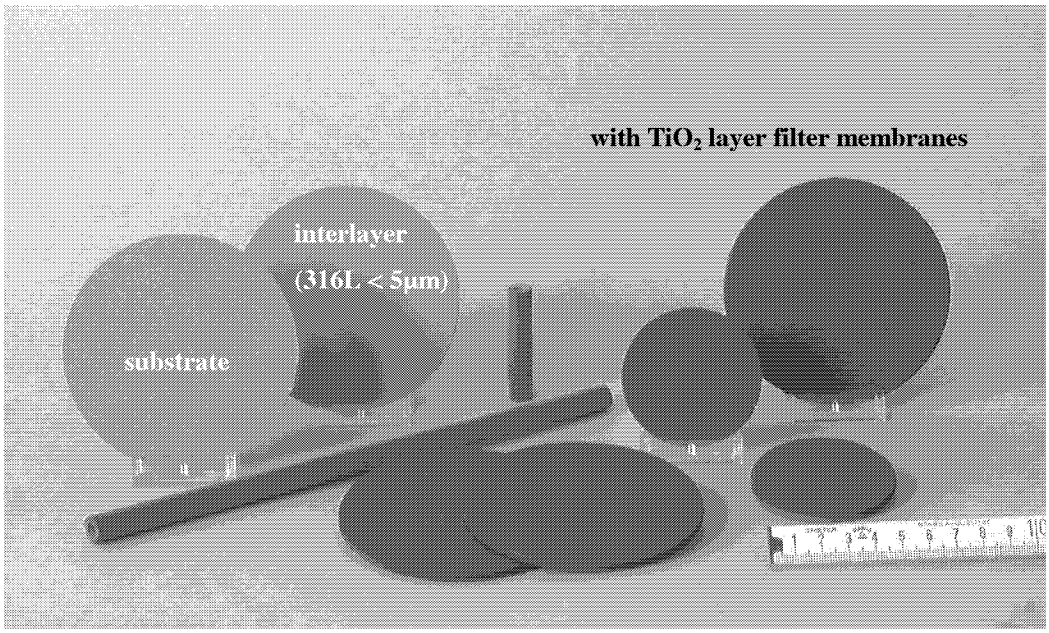

Fig. 4-50 Overview of the products

4.7 Simulation Results

4.7.1 Parameter Studies

For the graded filter membrane the two most important parameters are the pore diameter and the thickness of different layers. A parameter study was done in order to investigate how these two parameters influence the flow rate of this structure. It is assumed that the graded structure was coated onto ϕ 93 mm Sika R10 AX planar substrate. Table 4-12 shows the standard parameters of different layers. The atmospheric condition is taken the same as that of experiments, by air 20°C, 1 atm.

According to the standard parameters listed in Table 4-12, a series parameter studies were carried out. Each time only one parameter in the table was changed and the other kept the same.

Table 4-12 Standard parameters of different layers

Different layers	Pore diameter [μm]	Thickness [μm]
TiO_2	0.1	20
Interlayer 316L (particle size < 5 μm)	1.0	150
Interlayer 316L (particle size < 16 μm)	2.5	250
Substrate Sika R 10 AX	17	3000

Fig. 4-51 and Fig. 4-52 show the simulation results. It can be observed from the diagrams clearly that the thickness and the pore diameter of the TiO_2 layer have a definitive greater influence on the flow rate of the structure than the two intermediate layers. With decreasing the thickness of the layers, the flow rate can be increased; also with increasing the pore

diameter of the layers, the enhancement of the flow rate can be realised. The same tendency has been obtained by the experiments also shown in Fig. 4-35 a.) and b.).

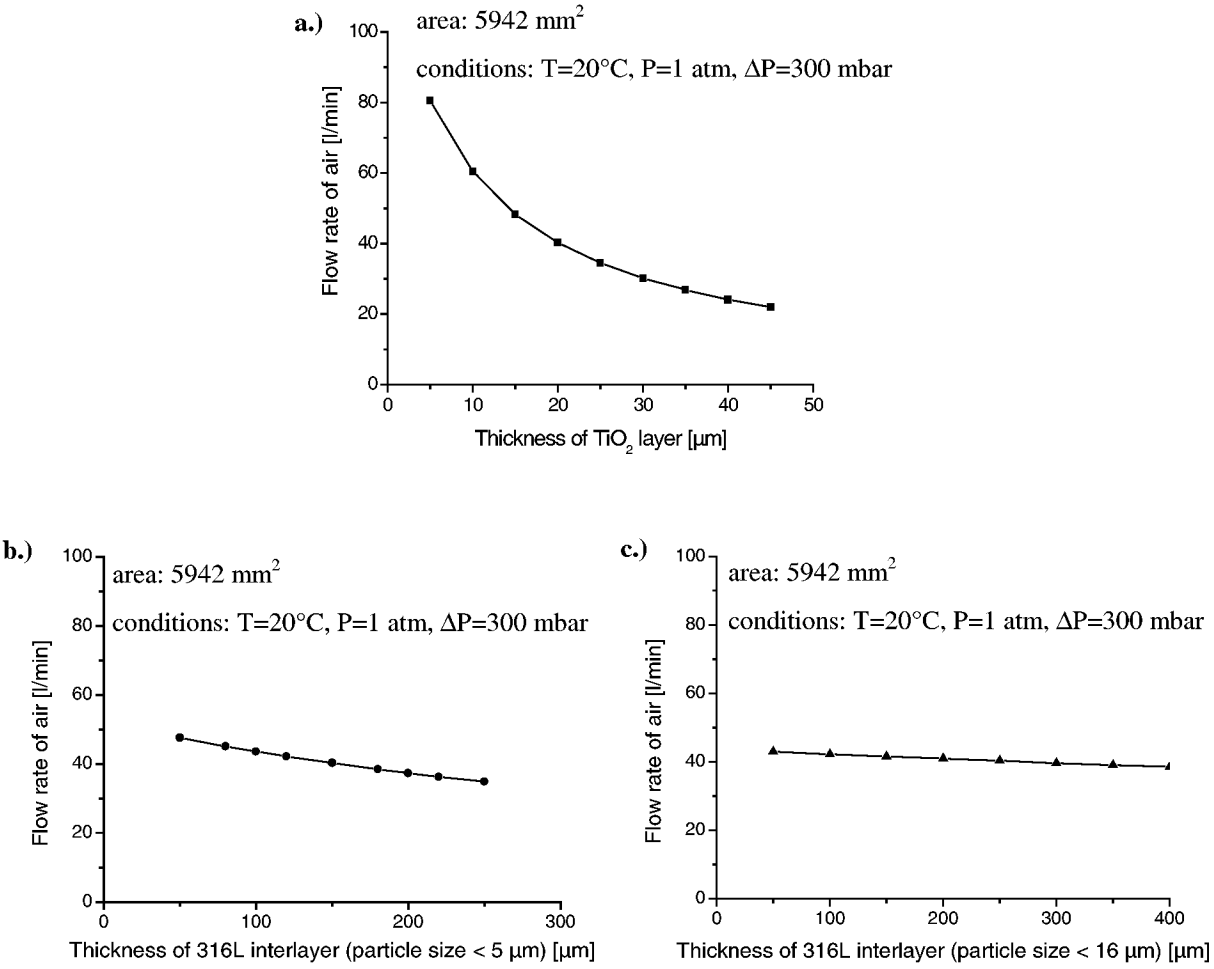

Fig. 4-51 Flow rate changing with the thickness of different layers
a.) TiO_2 layer; b.) Intermediate layer 316L (particle size < 5 µm);
c.) Intermediate layer 316L (particle size < 16 µm)

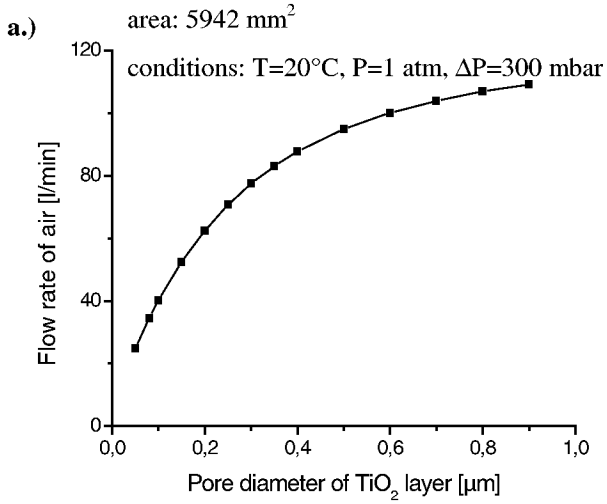

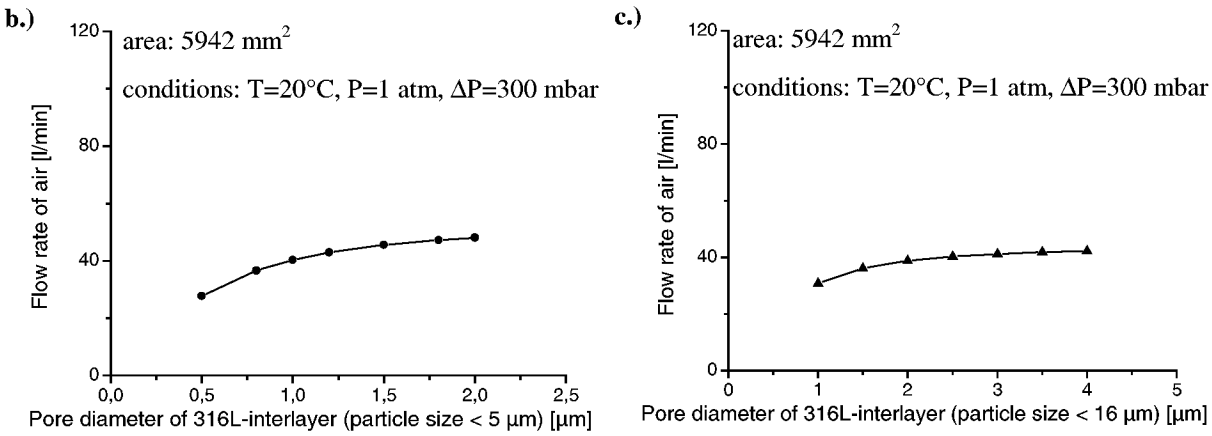

Fig. 4-52 Flow rate changing with the pore diameter of the different layers
a.) TiO_2 layer; b.) intermediate layer 316L (particle size < 5 µm);
c.) intermediate layer 316L (particle size < 16 µm)

It is very important to know from the calculation that the thickness of the two intermediate layers have only a slight influence on the flow rate of the structure comparing with that of TiO_2 active layer. Increasing the thickness of the interlayer 316L (particle size < 5 µm) from 100 µm to 200 µm, the flow rate is decreased from 43.6 l/min to 37.3 l/min (approximately 14%); for 316L < 16 µm layer, even the thickness is increased from 50 µm to 400 µm, the flow rate only changes from 42.9 l/min to 38.5 l/min; but if the thickness of the TiO_2 layer is changed only 5 µm, for example, from 20 µm to 25 µm, the flow rate will be decreased from 40.3 l/min to 34.5 l/min (approximately 14%), which gives a significant instruction for the manufacturing process.

As talked above, due to the rough surface of the substrate, the two interlayer must be coated thick enough to cover the unevenness of the substrate. Also some measures — e.g. grinding (a hand-made process) was taken to improve the surface quality of the based layer, so that the applied TiO_2 layer can be coated very well, which led to the undetermined thickness change during the grinding process. According to the above calculation and analysis it is obvious that these measures can be carried out continuously in the industrial fabrication without a great influence on the flow rate of the products. Also referencing the correlation between the pore diameter and the flow rate, it is helpful to make a decision how to choose the suitable starting powders of the active layer and the interlayer combining the consideration of the sintering temperature.

Basing the input data in Table 4-12, the flow rate of different layers was calculated. Fig. 4-53 a.) and b.) show the calculated results. Logically, the flow rate decreases gradually with coating a finer layer.

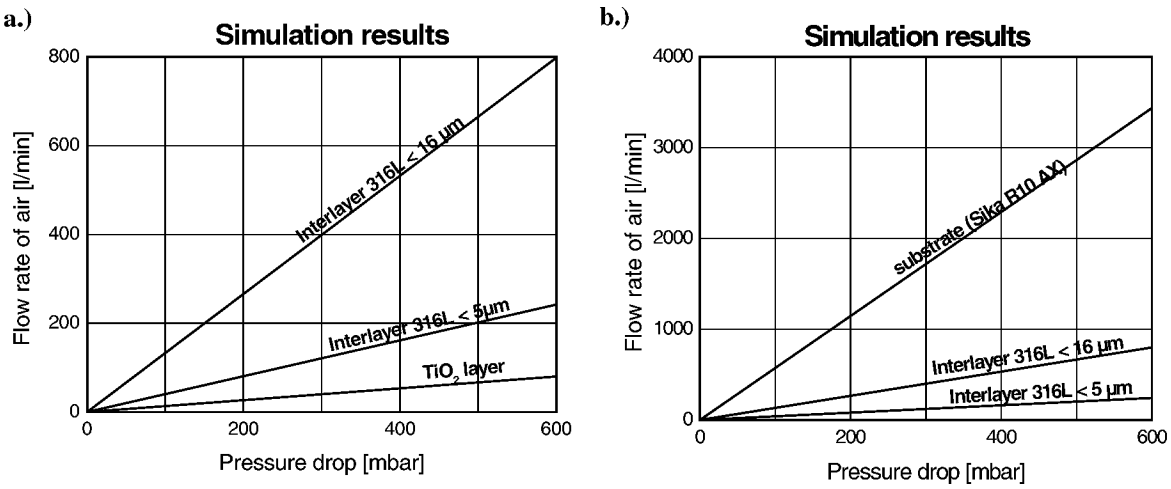

Fig. 4-53 Comparing the flow rate of different layers a.) TiO_2 layer and interlayer; b.) Substrate and interlayer, by air, 20°C, 1 atm, calculated area: 5942 mm^2

4.7.2 Modification of the Models

The important step for the simulation is to compare the simulation results with the experiment results, then the reliability of the models can be verified; furthermore, basing the experimental data, a modification can be done to improve the models. For our case, a series experimental data were obtained from GKN catalog. Table 4-13 shows the details of different specimens. The measurement was done both by air at 20°C, 1 atm and by water at 20°C; the filter surface is 5540 mm^2, and the thickness of the probes is 3 mm. Some diagrams (water as flow medium) measured by GKN and simulated by the model are shown in Fig. 4-54 a.) to d.).

Table 4-13 Properties of the products of GKN catalog

Products	Porosity [%]	Average pore diameter [µm]	Particle size distribution [µm]
Sika R0,5 AX	21	3.2	14~84
Sika R1 AX	21	3.5	70~100
Sika R3 AX	31	6	75~100
Sika R5 AX	31	1.0	100~200
Sika R10 AX	43	17	100~200
Sika R15 AX	40	19	200~300
Sika R20 AX	43	20	200~300
Sika R30 AX	43	28	300~500
Sika R40 AX	46	32	300~500
Sika R50 AX	47	42	500~700

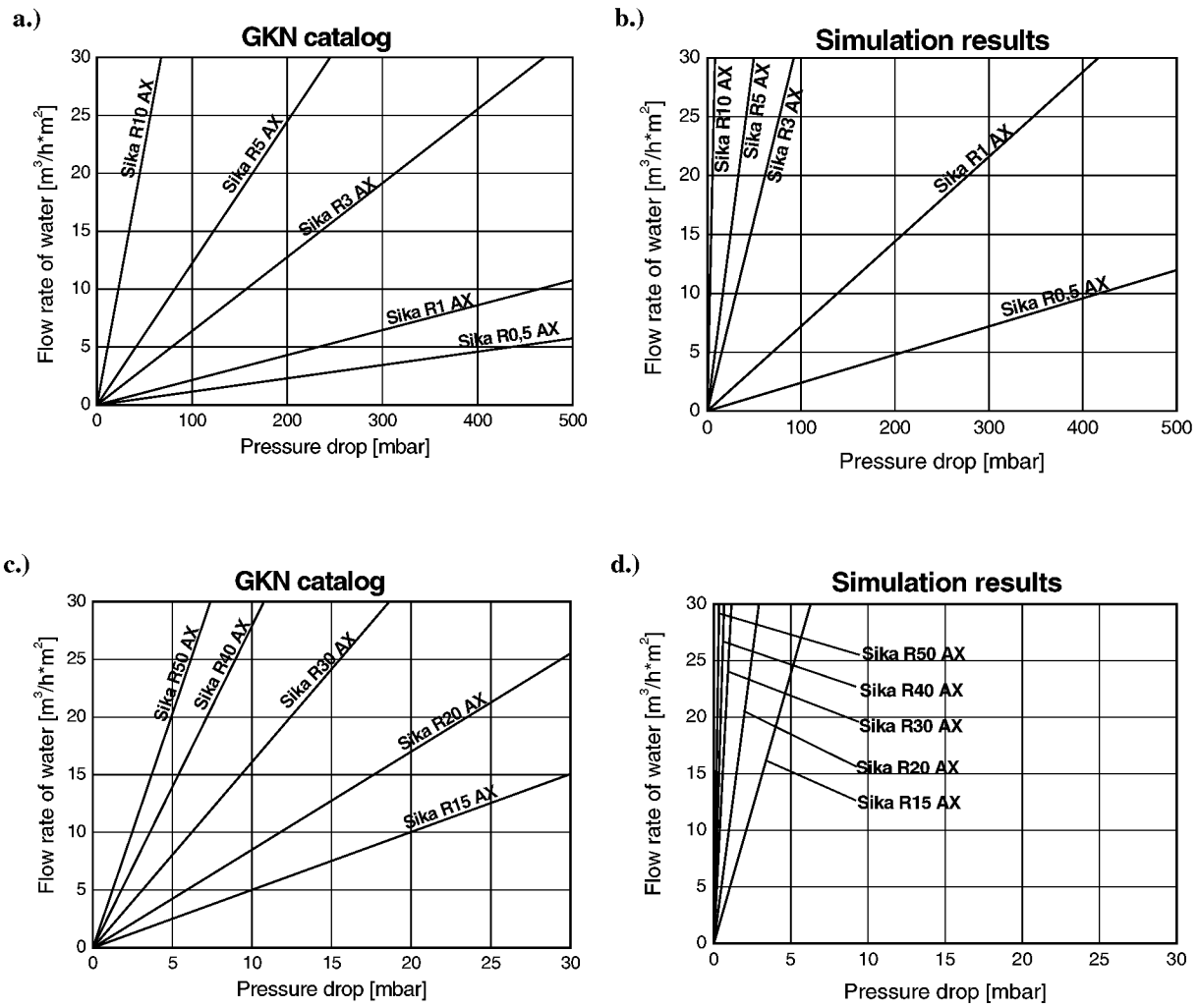

Fig. 4-54 Correlation between the flow rate and the pressure drop by water

a.) GKN catalog for Sika R1 AX to Sika R10 AX, b.) Simulation results for Sika R1 AX to Sika R10 AX

c.) GKN catalog for Sika R15 AX to Sika R50 AX, d.) Simulation results for Sika R15 AX to Sika R50 AX

It is obvious from the diagrams that the flow rate calculated by the model is higher than that of the experimental data. Of course, some experimental deviation must be anticipated also in this case, for example, Fig. 4-55 a.) and b.) show the irregularity of the experimental data of the probe Sika R3 AX.

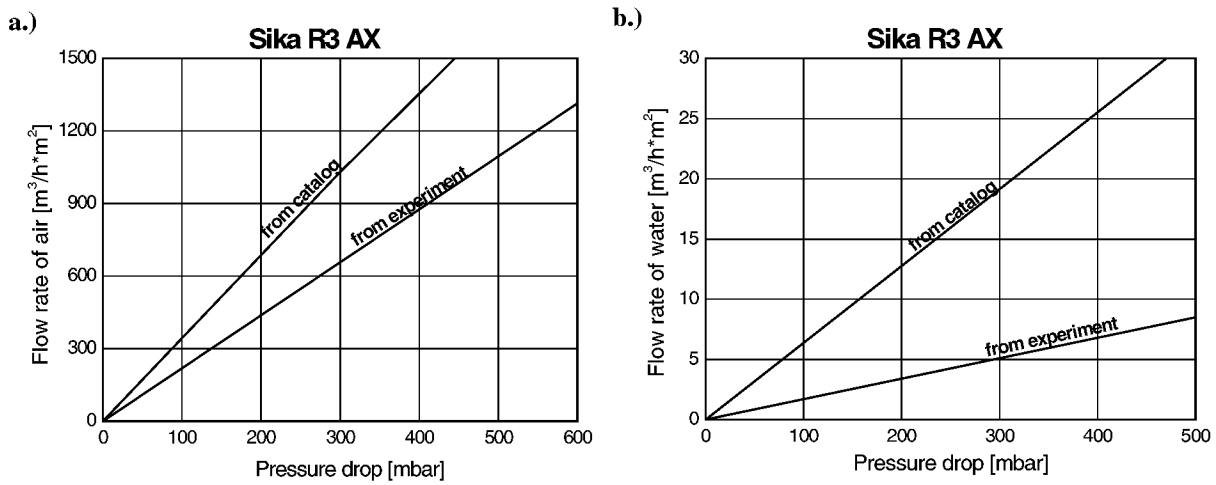

Fig. 4-55 Correlation between the flow rate and the pressure drop of Sika R3 AX
a.) by air, 20°C, 1 atm, b.) by water, 20°C

In order to find out the reason why the simulated flow rate is not well consistent with the experimental data, a reconsideration about the definition of the permeability of the structure has been done. As described in the section 3.6.1, Eq. (3.6.9) is the basic form of all capillary models, differing only in the method of calculating the mean square diameter and in the value used for $k'=k_0(L_e/L)^2$, which is a function of pore geometry. According to the Carman-Kozeny theory, the best value of the combined factor k' to fit most experimental data on packed beds is equal to 5, which is so-called Kozeny constant.

Considering the manufacture process and the starting-powder properties of the Sika R®...AX series — the irregular-shape particles are pressed uniaxially and sintered — the effective pore length of such kind of samples probably are different from that of the packed beds of spherical particles defined by Kozeny.

Due to the primary simulation results it is known that this length is higher than that in Kozeny model. Then a modification of the model was done, i.e., through a number of testing calculations, the ratio of L_e/L was increased 3 times. The permeability calculated in Eq. (3.6.12) was changed to:

$$k_{CKm} = \frac{\overline{D}_{p2}^2}{Z*180} \cdot \frac{\phi^3}{(1-\phi)^2} \tag{4.7.1}$$

where Z (Z=9) is the modification factor of the Sika R®...AX substrates to the permeability k_{CKm}. The same modification was also done for the gas flow model, where the flow length of the gas was increased also three times. Fig. 4-56 c.), d.), g.) and h.) show the calculation results after the modification. Comparing with the data of GKN catalog (Fig. 4-56 a.), b.) e.)

a.)

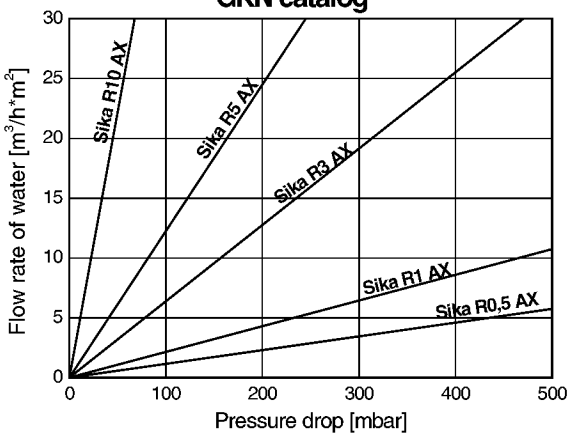
GKN catalog
Flow rate of water [m³/h*m²]
Pressure drop [mbar]
Sika R10 AX
Sika R5 AX
Sika R3 AX
Sika R1 AX
Sika R0,5 AX
0
5
10
15
20
25
30
0
100
200
300
400
500

c.)

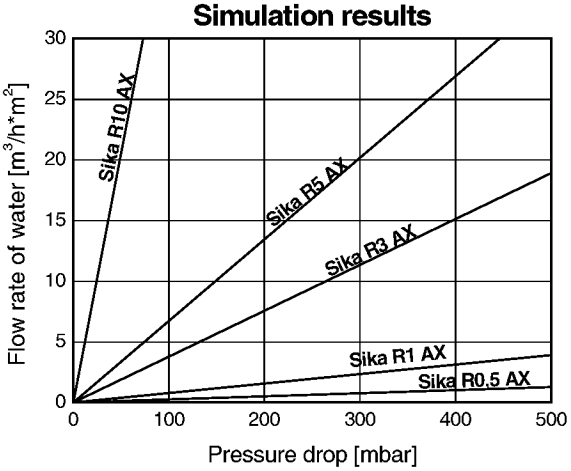
Simulation results
Flow rate of water [m³/h*m²]
Pressure drop [mbar]
Sika R10 AX
Sika R5 AX
Sika R3 AX
Sika R1 AX
Sika R0,5 AX
0
5
10
15
20
25
30
0
100
200
300
400
500

b.)

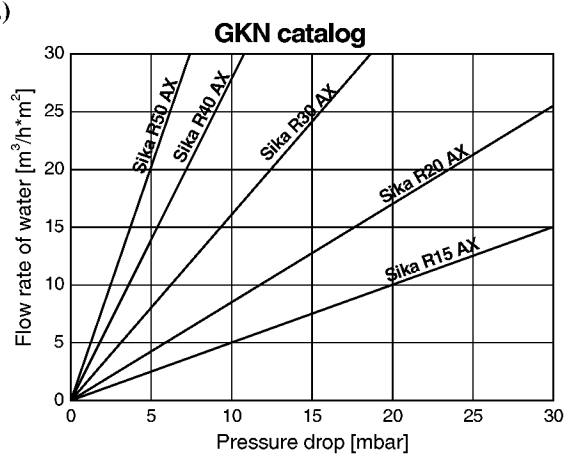
GKN catalog
Flow rate of water [m³/h*m²]
Pressure drop [mbar]
Sika R50 AX
Sika R40 AX
Sika R30 AX
Sika R20 AX
Sika R15 AX
0
5
10
15
20
25
30

d.)

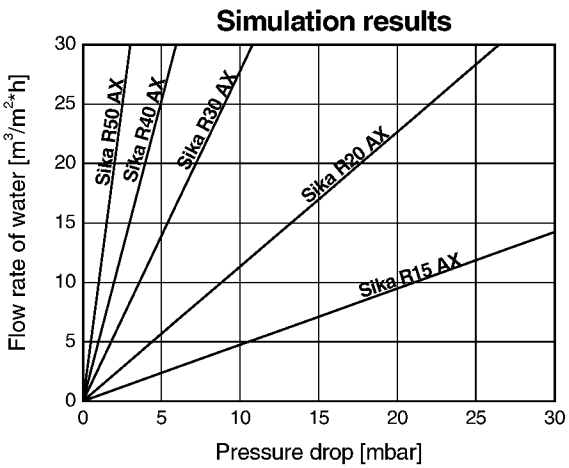
Simulation results
Flow rate of water [m³/m²*h]
Pressure drop [mbar]
Sika R50 AX
Sika R40 AX
Sika R30 AX
Sika R20 AX
Sika R15 AX
0
5
10
15
20
25
30

e.)

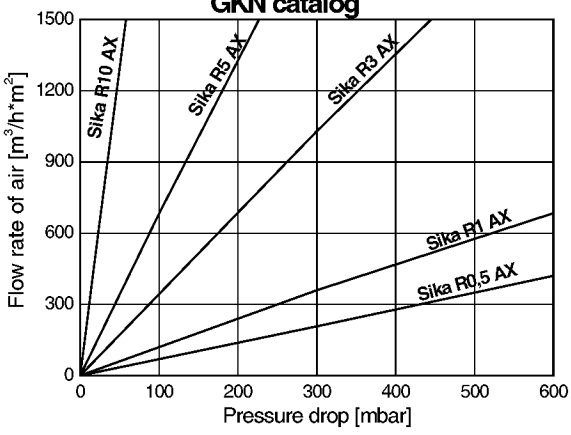
GKN catalog
Flow rate of air [m³/h*m²]
Pressure drop [mbar]
Sika R10 AX
Sika R5 AX
Sika R3 AX
Sika R1 AX
Sika R0,5 AX
0
300
600
900
1200
1500
0
100
200
300
400
500
600

g.)

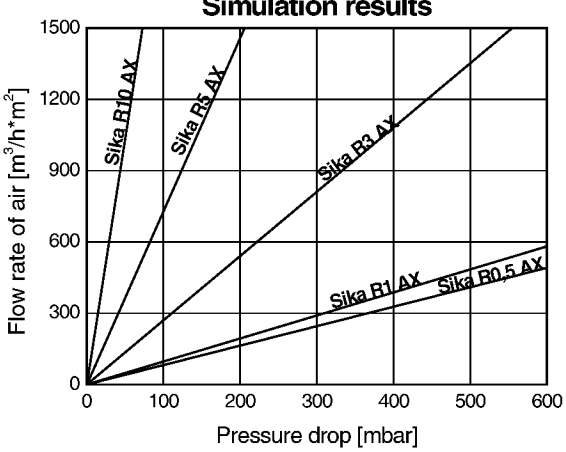
Simulation results
Flow rate of air [m³/h*m²]
Pressure drop [mbar]
Sika R10 AX
Sika R5 AX
Sika R3 AX
Sika R1 AX
Sika R0,5 AX
0
300
600
900
1200
1500
0
100
200
300
400
500
600

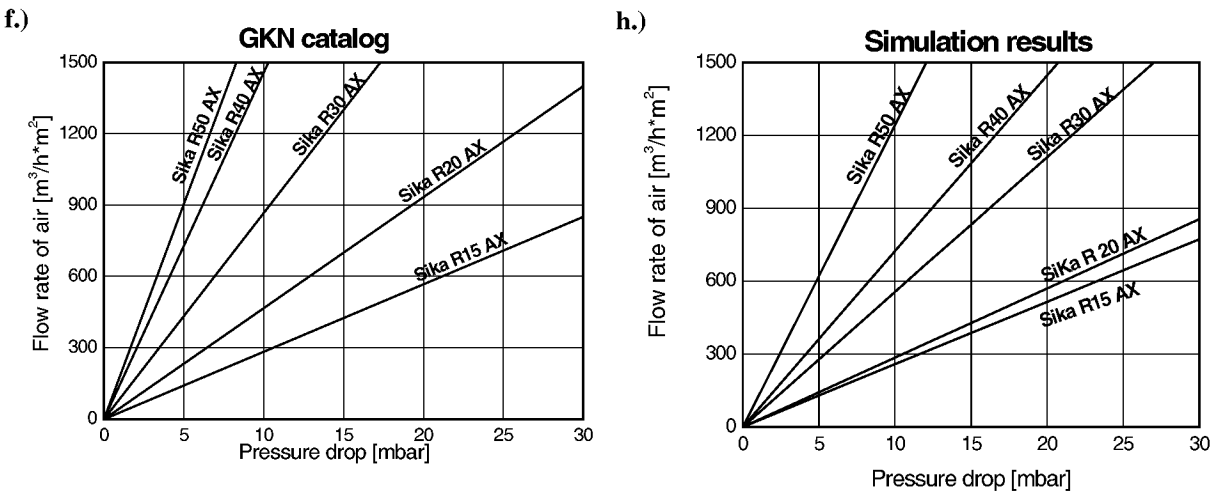

Fig. 4-56 Flow rate changing with the pressure drop by flow media water and air

a.), b.) GKN catalog for the products Sika R1 AX to Sika R50 AX, measured by water

c.), d.) Simulation results for the products Sika R1 AX to Sika R50 AX by water

e.), f.) GKN catalog for the products Sika R1 AX to Sika R50 AX, measured by air

g.), h.) Simulation results for the products Sika R1 AX to Sika R50 AX by air

and f.)), it is known that there still exists deviation between the calculation results and the experimental data, but the modelling results give at least a quite good forecast for the flow rate varying with the pressure drop as a modification factor $Z=9$ was adopted; although the modification work is considerably time consuming.

4.7.3 Comparing the Simulation Results with the Experimental Data

The same modification was done also to the 316L (particle size < 16 μm) and < 5 μm layers and TiO_2 layer by the Eq. (4.7.1). The experimental data in Fig. 4-34 and 4-35 were calculated by the modified model, whose results are shown in Fig. 4-57 a.), b.) c.) and 4-58 a.), b.) separately. Two more points were calculated and shown in Fig. 4-58 a. and b.), which present the flow rate of the support without the applied layer. Even there exist some deviations of some points between the calculation and the experiment data, the coincident tendency appears quite clearly.

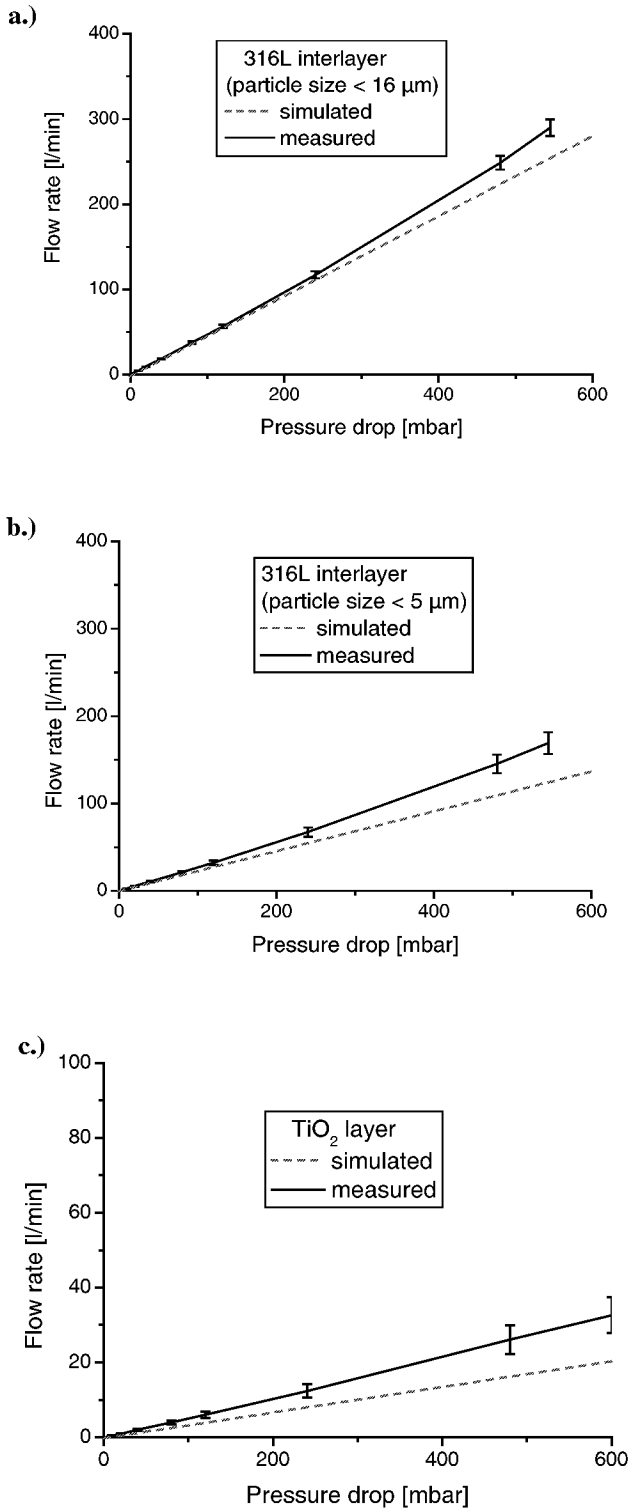

Fig. 4-57 Flow rate comparison between the measured and calculated results of a graded structure a.) with 316L interlayer (particle size < 16 µm); b.) with 316L interlayer (particle size < 5 µm); c.) with TiO_2 layer, measured and calculated by air at 20°C, 1 atm, measured area: 5153 mm^2

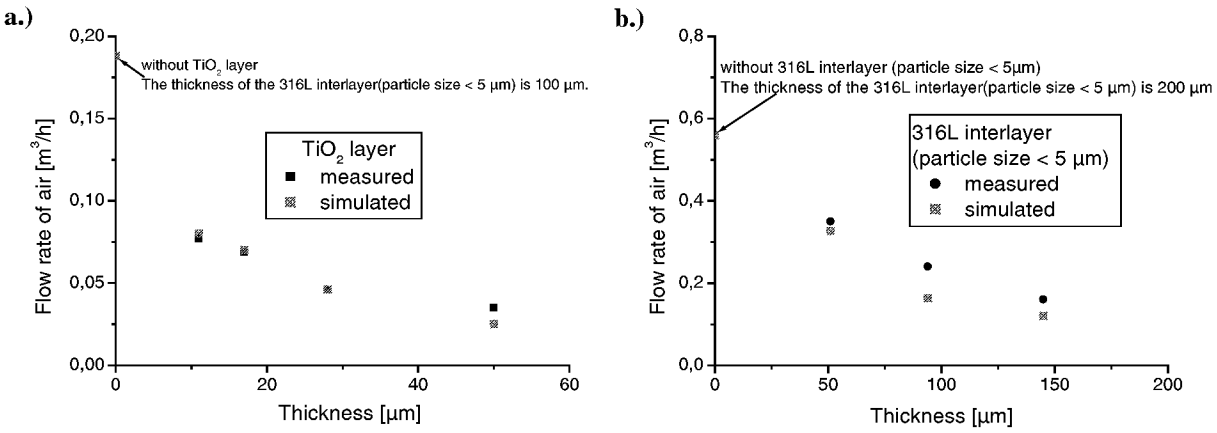

Fig. 4-58 Corelation between the flow rate and thickness of the functional layer

a.) TiO_2 layer; b.) 316L (particle size < 5 µm) layer

measured and calculated by air at 20°C, 1 atm, ΔP= 600 mbar, measured area 177 mm^2

According the above simulation results and the comparison between the measured and the calculated results it is reasonable to deduce that the models developed for calculating the flow rate of the graded structure are quite credible. Moreover, the program was coincident with Darcy's law quite well in calculating a one-layer structure, which proves that the programming code is proper.

5 Conclusions

Within the scope of this work it can be concluded that with the Wet Powder Spraying (WPS) process composite graded filter membranes (both for through-flow and cross-flow) made of functional TiO_2 layers onto gradual 316L stainless steel supports can be manufactured successfully. The average pore size of the functional TiO_2 layer is approximate 0.1 μm and the thickness of this layer lies in the range of 20~30 μm, which satisfy the requirements put forward at the beginning of this work.

An optimisation of the TiO_2 suspension was done basing the components taken over from a conventional ceramic suspension used in the WPS process, which was composed of powder, ethanol and a binder (PEI). The solvent — ethanol, was substituted by a mixture of ethanol and terpineol through a series evaporation-rate tests, which proved that this compound improved the drying speed of the suspension during spraying. An addition of acetic acid (HAc) contributed to shift the operational pH scale of the suspension far away from its isoelectric point pH^*_{iep} so that an electrostatic equilibrium can be realised. According to the obtained spraying experience it is known that the viscosity of the suspensions has a dominant influence on the performance of the spraying gun and the coating quality, an optimum value of the TiO_2 suspension should be smaller than 7 mPas. The viscosity of the suspension can be also controlled by the additive amount of the binder. 1.5% PEI reached the trough of the viscosity curve and was used in the suspension. Afterwards, an ageing test pertaining to the zeta-potential, pH value, particle size distribution and viscosity of the suspension was investigated in a fixed period, which demonstrated that the optimised suspension was quite stable. Through milling the suspension in different intervals and measuring the particle size distribution and the specific surface area contemporarily, an optimum milling duration of the suspension (20 hours) was acquired in order to avoid the unnecessary exhaust of the energy.

Due to the different geometry of through-flow and cross-flow membranes the spraying parameter sets of the WPS method were distinguished from for planar and for tubular separately. For the WPS technique the influence of each spraying parameter (the nozzle size of the gun, the spraying pressure, the spraying distance between the nozzle tip and samples, the moving speed of the gun, the spraying beam and the amount of suspensions) on the properties (mainly thickness) of the layer was investigated. Later on, the adaptation of the spraying parameters on the substrate geometry was preferential done by adjusting the suspension amount and the shape of the spraying beam. Also the distance between the meander lines becomes important, if the sample size is too large and a meander spraying

mode is used. When spraying onto a tubular specimen, the rotation speed of it must be taken into consideration, which combines the moving speed of the spraying gun exerting a great influence on the coating quality of the tubular specimens.

Considering that the thickness of the functional layer plays a significant role in the filtration performance, the correlation between the above spraying parameters and the thickness was investigated in detail for the whole spraying process. An important experience obtained from the process is that a multi-layer spraying mode coupling with the optimised other spraying parameters enables a desired thickness to be obtained easily. Then the optimised spraying parameter sets both for planar and for tubular were acquired basing this concept. Furthermore, a comparison was done for the thickness obtained by the green-layer-measuring method and by metallographical method, which proved that the former had a quite good coincident tendency with the latter and can be relied on to estimate the coating thickness.

Applying the optimised suspension and the improved spraying parameters a quite homogeneous TiO_2 layer can be realised.

Except the particle size of the starting powder, the sintering temperature determines the pore size of the porous media. Well grown sintering necks ensure a higher fluid permeability of the porous structure. Through sintering the samples at different temperatures and analysing the surface structure by means of the SEM the optimised sintering temperature ranges for the two intermediate layers (900°C) and the TiO_2 layer (950°C) were gained. The enhanced sintering temperature of the TiO_2 layer led to a post-sintering of the intermediate layers, which contributed to the occurrence of compression stress in the TiO_2 layer avoiding the cracks formation. At the same time, a cofiring process was implanted into the sintering process for the two intermediate layers due to the consideration of economy, which was verified by the following experiments an effective measure.

XRD measurements reveal that during sintering of the TiO_2 layer a reaction with the steel substrate takes place, which leads to the formation of the new phase $Cr_{0.12}Ti_{0.78}O_{1.74}$. Probably this formation causes the colour change of the TiO_2 layer from white to dark blue.

Flow rate measurement of different layers showed that the thickness of the functional layer has a great influence on this property. The thicker the layer is, the lower the flow rate will be. Under the circumstances that the strength and quality could be ensured the functional layer should be coated as thin as possible. Comparing the coated TiO_2 membrane of FZJ with TAMI commercial products in flow rate it is found that the FZJ samples are quite competitive.

The endurance during the shear strength and the chemical resistance tests proved the stability of the FZJ products further.

With the help of the capillary theory a systematic analysis about the imperfections (spherical pores) lying in the intermediate layers was done. Due to this theory a series measures were taken to avoid the failures, e.g. wetting the support surface before spraying TiO_2 layer to prevent from the quick disappearance of the solvent, then a homogeneous surface can be obtained; grinding the surface of the supports in order to minimise the influence of the roughness from the supports on the quality of the applied layers, which has been adopted standard for tubular samples; Using ultrasonic wave table as a support for planar samples, by means of the bubble-point test it shows a definite decrease of the imperfections.

Basing the above work a batch of products were produced and the know-how has been transferred to the company GKN.

Finally, mathematical models basing Carman-Kozeny theory was developed to simulate the flow process inside the graded structure both for fluid and gas — predicting the flow rate of such structure, vice versa, when a desired flow rate is given, the thickness of the functional layer of the graded structure can be calculated also. According to the parameter studies it can be concluded that the thickness and pore size of the functional TiO_2 layer has a much greater influence on the flow rate of the graded composite filter than that of the interlayer. Thereunto the thickness influence of the functional layer has been found in the experiments already and proved again here.

With these models, the flow process inside the graded structure can be better understood. A puzzle of the thickness change caused by grinding the two intermediate layers was explained very well and can be kept on applying industrially — for a slight change of the thickness of the two intermediate layers acts almost no influence on the flow rate of the structure.

Through comparing the calculated results with the measured results a modification of the models was carried out and testified — the simulation results are quite credible and can be taken as a beneficial tool to forecast the flow rate of the graded structure.

6 Literature

[1] Gutman R. G.: *Membrane Filtration: the technology of pressure-driven crossflow processes*, Adam Hilger, Bristol, 1987.

[2] Cheryan M.: *Ultrafiltration and microfiltration handbook*, Technomic Publishing AG, Basel, Switzerland, 1998.

[3] Porter J. J., Gomes A. C.: *The rejection of anionic dyes and salt from water solutions using a polypropylene microfilter*, Desalination, 2000, 128, p.81.

[4] Trzebibatowska M., Szaniawska D.: *Inorganic membranes in food processing*, Environment Protection Engineering, 1998, 24(1), p.65.

[5] Kraus K. A., Johnson J. S.: *Colloidal hydrous oxide hyperfiltration membrane*, U.S. Patent 3,413,219, 1966.

[6] Marcinkowsky A. E., Johnson J. S., Kraus K. A.: *Hyperfiltration method of removing organic solute from aqueous solution*, U.S. Patent 3, 537,988, 1968

[7] Bhave R. R.: Inorganic Membrane: synthesis, characteristics and applications, Gillot J.: *1. The developing of inorganic membranes: A historical perspective*, Van Nostrand Reinhold, New Jork, 1991.

[8] Ishizaki K., Komarneni S., Nanko M.: *porous material — Process technology and applications*, Kuwer Academic Publishers, 1998.

[9] P. Neumann: *Mat. Wiss. u. Werkstofftechn.*, 2000, 31, p.422.

[10] Rantala P., Kuula-Väisänen P.: *Polishing filtration with ceramic membranes*, Filtration + Separation, 2000, Jan./Feb., p.32.

[11] Rushton A., Ward A. S., Holdich R. G.: *Solid-liquid filtration and separation technology*, VCH mbH, Weinheim, Germany, 1996.

[12] Dowson G.: *Powder Metallurgy — The process and its products*, Adam Hilger, Bristol and New York, 1990.

[13] Dokras S.: *Metallic filters —A review*, Metallurgical Engineer, 1981, p.21.

[14] Morgan V. T.: *Sintered metal filters*, Hydraulic Pneumatic Power, 1974, Sep., p.323.

[15] Shojai F., Mäntylä T.: *Monoclinic zirconia microfiltration membranes: Preparation and characterization*, Journal of Porous Materials, 2001, 8, p.129.

[16] Shojai F., Mäntylä T.: *Effect of sintering temperature and holding time on the properties of 3Y-ZrO_2 microfiltration membranes*, Journal of Materials Science, 2001, 36, p.3437.

[17] Shojai F., Mäntylä T.: *Structural stability of yttria doped zirconia membranes in acid and basic aqueous solutions*, Journal of European Ceramic Society, 2001, 21, p.37.

[18] Shojai F., Pettersson A. B. A., Mäntylä T.: *Surface energy components and contact angle of pure and yttria-doped zirconia membranes*, Key Engineering Materials, 1997, 132-136, p. 1742.

[19] Gillot J.: *New inorganic ultrafiltration membranes: Titania and zirconia membranes*, J. Am. Ceram. Soc., 1989, 72(2), p.257.

[20] Kim J., Lin Y. S.: *Synthesis and characterization of suspension-derived, porous ion-conducting ceramic membranes*, J. Am. Ceram. Soc., 1999, 82(10), p. 2641.

[21] Kim J., Lin Y. S.: *Sol-gel synthesis and characterization of yttria stabilized zirconia membranes*, Journal of Membrane Science, 1998, 139, p.75.

[22] Okubo T., Takahashi T., Sadakata M., etc.: *Crack-free porous YSZ membrane via controlled synthesis of zirconia sol*, Journal of Membrane Science, 1996, 118, p. 151.

[23] Siewert C., Richter H., Piorra A.: *Development of ceramic nanofiltration membranes*, Industrial Ceramics, 2000, 20(1), p.31.

[24] Chang C. H., Gopalan R., Lin Y. S.: *A comparative study on thermal and hydrothermal stability of alumina, titania and zirconia membranes*, Journal of Membrane Science, 1994, 91, p.27.

[25] Lin Y. S., Burggraaf A. J.: *Experimental studies on pore size change of porous ceramic membranes after modification*, Journal of Membrane Science, 1993, 79, p.65.

[26] Wang P., Xu N. P., Shi J.: *A pilot study of the treatment of waste rolling emulsion using zirconia microfiltration membranes*, Journal of Membrane Science, 2000, 173, p.159.

[27] Yang C., Zhang G. S., Xu N. P., etc.: *Preparation and application in oil-water separation of ZrO_2/α-Al_2O_3 MF membrane*, Journal of Membrane Science, 1998, 142, p.235.

[28] Darcovich K., Roussel D., Toll F. N.: *Sintering effects related to filtration properties of porous continuously gradient ceramic structures*, Journal of Membrane Science, 2001, 183, p.293.

[29] Darcovich K., Cloutier C. R.: *Processing of functionally gradient ceramic membrane substrates for enhanced porosity*, J. Am. Ceram. Soc., 1999, 82(8), p.2073.

[30] Darcovich K., Price M. E.: *Preparation of functionally gradient ceramic membrane substrates*, Journal of the Canadian Ceramic Society, 1997, 66(2), p.146.

[31] Vercauteren S., Keizer K., Vansant E. F.: *Porous ceramic membranes: Preparation, transport properties and applications*, Journal of Porous Materials, 1998, 5, p.241.

[32] Sánchez-Herencia A. J., Morinaga K., Moya J. S.: *Al_2O_3/Y-TZP continuous functionally graded ceramics by filtration-sedimentation*, Journal of the European Ceramic Society, 1997, 17, p.1551.

[33] Hsieh H. P., Bhave R. R., Fleming H. L.: *Microporous alumina membranes*, Journal of Membrane Science, 1988, 39, p.221.

[34] Stech M., Reynders P., Rödel J.: *Constrained film sintering of nanocrystalline TiO_2*, J. Am. Ceram. Soc., 2000, 83(8), p.1889.

[35] Palacio L., Prádanos P., Calvo J. I., etc.: *Fouling, structure and charges of a composite inorganic microfiltration membrane*, Colloids and Surfaces, 1998, 138, p.291.

[36] Porter J. J., Zhuang S.: *Microfiltration of sodium nitrate and direct red 2 dye using asymmetric titanium dioxide membranes on porous ceramic tubes*, Journal of Membrane Science, 1996, 110, p.119.

[37] Porter J. J., Porter R. S.: *Filtration studies of selected anionic dyes using asymmetric titanium dioxide membranes on porous stainless-steel tubes*, Journal of Membrane Science, 1995, 101, p.67

[38] Szaniawski A. R., Spencer H. G.: *Microfiltration of pectin solutions by a titanium dioxide membrane*, Key Engineering Materials, 1991, 61&62, p.243.

[39] Fujii T., Yano T., Nakamura K., etc.: *The sol-gel preparation and characterization of nanoporous silica membrane with controlled pore size*, Journal of Membrane Science, 2001, 187, p.171

[40] Castro R. P., Monbonquette H. G., Cohen Y.: *Shear-induced permeability changes in a polymer grafted silica membrane*, Journal of Membrane science, 2000, 179, p.207.

[41] Chu L., Anderson M. A.: *Microporous silica membranes deposited on porous supports by filtration*, Journal of Membrane Science, 1996, 110, p.141.

[42] Guizard C., Larbot A., and Cot L.: *Ceramic thin layers from the sol-gel process*, Vide, 1985, 227, p.277.

[43] Larbot A., Fabre J. P., Guizard C.: *Inorganic Membranes obtained by sol-gel techniques*, Journal of Membrane Science, 1988, 39, p.203.

[44] Wang H. T., Liu X. Q., Zheng H.: *Gelcasting of $La_{0.6}Sr_{0.4}Co_{0.8}Fe_{0.2}O_{3-\delta}$ from oxide and carbonate powders*, Ceramics International, 1999, 25, p.177.

[45] Fübi M., Buchkremer H. P., Stöver D.: *Wet Powder Spraying (WPS) — a new PM-route for processing fiber reinforced MMC's*, Proc. of PM' 94, Paris France, 1994, p.483.

[46] Prinz D., Arnhold V., Buchkremer H. P.: *Graded high-porous microfilters by powder metallurgical coating techniques*, VW-Berichte, Dresden, 1998.

[47] Buchkremer H. P., Stöver D., Neumann P., Arnhold V.: *Processing and characteristic parameters of filter parts with asymmetric porosity*, Proc. of PM' 98, Granada Spain, 1998.

[48] Zhao L., Bram M., Buchkremer H. P., Stöver D., Li Z.: *Development of a graded porous metallic filter for microfiltration using the wet powder spraying technique*, Proc. of PM' 2001, Nice France, 2001, p.335.

[49] Chan K. K., Browstein A. M.: *Ceramic Membranes — Growth prospects and opportunities*, Ceramic Bulletin, 1991, 70(4), p.703.

[50] Beyer F., Günther R., Hapke J.: *Status Quo — Überblick über den Stand der Technik bei Membrantrennverfahren im Umweltschutz*, Chem. Techn., 1996, 25, p.64.

[51] Bhave R. R.: Inorganic Membrane: synthesis, characteristics and applications, Burggraaf A. J., Keizer K.: *2. Synthesis of Inorganic Membranes*, Van Nostrand Reinhold, New Jork, 1991.

[52] Bram M., Buchkremer H. P., Stöver D., Neumann P.: *Development of Graded Porous Structures for Filtering Applications*, Proc. of Materials Week' 2000, Munich Germany, 2000.

[53] Messing M., Fuller G. E., Hausner H., eds: *Ceramic Powder Processing*, Westerville, OH. Am. Ceram. Soc. Inc., 1988.

[54] Keizer K., Burggraaf A. J.: *Porous Ceramic Materials in Membrane Applications*, Sci. Ceram., 1988, 14, p.83.

[55] SRI Consulting, *Microporous Inorganic Membrane Overview*, Consulting Report, 2000.

[56] Trulson O. C., Litz L. M.: *Ultrafiltration apparatus and process for the treatment of liquids*, U.S. Patent 3,977,967, 1973.

[57] Manjikian S.: *Production of semipermeable membranes directly on the surfaces of permeable support bodies*, U.S. Patent 3,544,358, 1966.

[58] Bhave R. R.: Inorganic Membrane: synthesis, characteristics and applications, Hsieh H. P.: *3. General Characteristics of Inorganic Membranes*, Van Nostrand Reinhold, New Jork, 1991.

[59] Dullien F.A.L.: *Porous Media – Fluid Transport and Pore Structure*, San Diego, Calif.: Academic Press, 1992.

[60] Collins R. E.: *Flow of fluids through porous materials*, Von Nostrand-Reinhold, Princeton, New Jersey, 1961.

[61] Scheigegger A. E.: *The physics of flow through porous media*, 3rd ed. Univ. of Toronto Press, Toronto, 1974.

[62] Glaves C. L., Davis P. J., Moore K. A.: *Pore structure characterization of composite membranes*, J. Colloid and Interface Sci., 1989, 133(2), p.377.

[63] ASTM E 1294.

[64] Metals Handbook, *Properties and Selection of Metals*, Vol. 1. 8th edition, American Society for metals, 1961.

[65] Fübi M., Buchkremer H. P., Stöver D.: *Nasspulverspritzen (Wet Powder Spraying WPS) – Verfahrensbeschreibung*, Forschungszentrum Jülich GmbH, 1994.

[66] Fübi M.: *Herstellung von Metall-Matrix-Verbund-Werkstoffen mittels der Verfahren Naßpulverspritzen und Naßpulvergießen*, Dissertation (RWTH-Aachen), Forschungszentrum Jülich, Sep. 1995.

[67] Prinz D., Arnhold V., Buchkremer H. P., Kuhstoss A., Neumann P., Stöver D.: *Graded High Porous Microfilters by Powder Metallurgical Coating Techniques*, Materials Science Forum, Trans Tech Publications, Switzerland, 1999, 308-311, p.59.

[68] Vaßen R., Stöver D.: *Processing and properties of nanophase ceramics*, J. Materials Processing Technology, 1999, 92-93, p.77.

[69] Schüller E.: *Entwicklung von Submikro-Pulver-Suspensionen zur Herstellung dünner Elektrolytschichten für Hochtemperaturbrennstoffzellen*, Dissertation (Uni Bochum), Forschungszentrum Jülich, Feb. 2002.

[70] Hashiba M., Okamoto H., Nurishi Y., Hiramatsu K.: *The zeta-potential measurement for concentrated aqueous suspension by improved electrophoretic mass transport apparatus – application to Al_2O_3, ZrO_3 and SiC suspensions*, Journal of Materials Science, 1988, 23, p.2893.

[71] Cesarano III J., Aksay I. A., Bleier A.: *Stability of aqueous α-Al_2O_3 suspensions with poly(methacrylic acid) polyelectrolyte*, J. Am. Ceram. Soc., 1988, 71(4), p.250.

[72] Baklouti S., Pagnoux C., Chartier T., Baumard J. F.: *Processing of aqueous α-Al_2O_3, α-SiO_2 and α-SiC suspensions with polyelectrolytes*, J. Europ. Ceram. Soc., 1997, 17, p.1387.

[73] Guo L. C., Zhang Y., Uchida N., Uematsu K.: *Adsorption effects on the rheological properties of aqueous alumina suspensions with polyelectrolyte*, J. Am. Ceram. Soc., 1998, 81(3), p.549.

[74] Schilling C. H., García V. J., Smith R. M.: *Ultrasonic and mechanical behavior of green and partially sintered alumina: Effects of slurry consolidation chemistry*, J. Am. Ceram. Soc., 1998, 81(10), p.2629.

[75] Heijman S. G. J., Stein H. N.: *Electrostatic and sterical stabilizaition of TiO_2 dispersions*, Langmuir, 1995, 11, p.422.

[76] Van der Hoeven Ph. C., Lykelma J.: *Electrostatic stabilization in non-aqueous media*, Adv. Colloid Interface Sci., 1992, 42, p.205.

[77] Widegren J., Bergström L.: *The effect of acids and bases on the dispersion and stabilization of ceramic particles in ethanol*, J. Euro. Ceram. Soc., 2000, 20, p.659.

[78] Wang G. H., Sarkar P., Nicholson P. S.: *Influence of acidity on the electrostatic stability of alumina suspensions in ethanol*, J. Am. Ceram. Soc., 1997, 80(4), p.965.

[79] Morris G. E., Skiner W. A., Self P. G., Smart R. St. C.: *Surface chemistry and rheological behaviour of titania pigment suspensions*, Colloids and Surfaces A: Physicochemical and Engineering Aspects, 1999, 155, p.27.

[80] Shojai F., Pettersson A. B. A., Mäntylä T., Rosenholm J. B.*: Electrostatic and electrosteric stabilization of aqueous slips of 3Y-ZrO_2 powder*, J. Euro. Ceram. Soc., 2000, 20, p.277.

[81] Fernández-Nieves A., de las Nieves F. J.: *The role of ζ potential in the colloidal stability of different TiO_2/electrolyte solution interfaces*, Colloids and Surfaces A: Physicochemical and Engineering Aspects, 1999, 148, p.231.

[82] Terayama H., Okumura K., Sakai K, etc.*: Aqueous dispersion behavior of drug particles by addition of surfactant and polymer*, Colloids and Surfaces B: Biointerfaces, 2001, 20, p.73.

[83] Wernet J., Feke D. L.: *Effects of solids loading and dispersion schedule on the state of aqueous alumina/zirconia dispersions*, J. Am. Ceram. Soc., 1994, 77(10), p.2693.

[84] Zupančič A., Lapasin R., Kristoffersson A.: *Rheological properties of aqueous αAl_2O_3 suspensions: Influence of dispersant concentration*, The Canadian Journal of Chemical Engineering, 1999, 77(8), p.627.

[85] Tari G., Ferreira J. M. F., Lyckfeldt O.: *Influence of the stabilising mechanism and solid loading on slip casting of alumina*, J. Europ. Ceram. Soc., 1998, 18, p. 479.

[86] Lenk R., Richter H. J., Adler J.: *Kostengünstige keramische Flachmembranen*, GIT Labor-Fachzeitschrift, 1999, 9, p.936.

[87] Dullien F.A.L.: *Porous Media – Fluid Transport and Pore Stucture*, New York: Academic Press, 1979.

[88] Carman P.C.: *Fluid Flow through Granular Beds*, Trans. Inst. Chem. Eng., London 1937, 15, p.150.

[89] Carman P.C.: *Determination of the specific surface of powders*, J. Soc. Chem. Ind. 1938, 57, p.225.

[90] Carman P.C.: *Flow of gases through porous media*, Butterworths, London, 1956.

[91] Kozeny J.: Royal Academy of Science, Vienna, Proc. Class I, 1927, 136, p.271.

[92] Dullien F.A.L.: In proceedings „ Physics of Granular Media", February 20th – March 1st, Les Houches, France, 1990.

[93] Chatzis I., Ph.D. Thesis, University of Waterloo, Ontario, Canada, 1980.

[94] Childs E.C, Collis-George N.: *The permeability of porous materials*, Proc. R. Soc. London Ser. 1950, A 210, p.392.

[95] Marshall T.J.: *A relation between permeability and size distribution of pores*, J. Soil. Sci., 1958, 9(1), p.1.

[96] Millington R.J., Quirk J.P.: *Permeability of porous solids*, Tran. Faraday Soc. 1961, 57, p.1200.

[97] Brutsaert W.: *The permeability of a porous medium determined from certain probability laws for pore size distribution*, Water Resource Res., 1968, 4, p.425.

[98] Haring R.E., Greenkorn R.A.: *A statistical model of a porous medium with nonuniform pores*, AIChE J., 1970, 16, p.477.

[99] Rumpf H., Gupte A.R.: *Einflüsse der Porosität und Korngrößenverteilung im Widerstandsgesetz der Porenströmung*, Chem. Ing. Tech. 1971, 43, p.367.

[100] Bird R. B., Stewart W.E., Lightfoot E. N.: *Transport Phenomena*, Wiley, New York, 1971.

[101] Scheidegger A.E.: *The physics of flow through porous media*, 3rd ed., University of Toronto Press, Toronto, 1960.

[102] Ergun S.: *Fluid flow through packed columns*, Chem. Eng. Prog., 1952, 48(2), p.89.

[103] Forchheimer: *Wasserbewegung durch Boden*, Z. Ver. Deutsch. Ing., 1901, 45, p.1781.

[104] Polubarinova-Kochina P.YA.: *Teoriya dvizheniya gruntovykh*, vod. Gosudarstv, Izdat. Tekh. –Teoret. Lit., Moscow, 1952 [English transl.: R. deWiest, Theory of Groundwater Movement, Princeton Univ. Press. Princeton, New Jersey, 1962].

[105] Irmay s.: *On the theoretical derivation of Darcy and Forchheimer formulas*, Trans. Am. Geophys. Un., 1959,39(4), p.702.

[106] Ahmed N., Sunada D.K.: *Nonlinear flow in porous media*, J. Hyd. Div. Proc. ASCE, 1969, 95(HY6), p. 1847.

[107] Geertsma J.: *Estimating the coefficient of inertial resistance in fluid flow through porous media*, Soc. Pet. Eng. J., 1974, 14, p.445.

[108] Macdonald I.F., El-Sayd M.S., Mow K., and Dullien F.A.L.: *Flow through porous media —the Ergun equation revisited*, Ind. Eng. Chem. Fundam., 1979, 18(3), p.199.

[109] Chatzis I., Dullien F.A.L., J. Can. Pet. Technol. 1977, 16, p.97.

[110] Koplik J.: *Creeping flow in two-dimensional networks*, J. Fluid Mech., 1982(119), p.219.

[111] Andrade J.S. Jr., Street D.A., Shinohara T., Shibusa Y., Arai Y.*: Percolation disorder in viscous and nonviscous flow through porous media*, Phys. Rev. E, 1995, 51(6), p. 5725.

[112] Andrade J.S. Jr., Costa U.M.S., Almeida M.P., Makse H.A., Stanley H.E.: *Inertial effects on fluid flow through disordered porous media*, Phys. Rev. Lett., 1999, 82(26), p. 5249.

[113] Andrade J.S. Jr., Buldyrev S.V., Dokholyan N.V., Havlin S., King P.R., Lee Y., Paul G., Stanley H.E.: *Flow between two sites on a percolation Cluster*, Phys, Rev. E, 2000, 62(6), p.8270.

[114] Wang X. H., Liu Z. F., Wu Q. S., Li B.: *Statistical properties for two-dimensional fluid flow in percolation porous media*, Phy. A, 2002, 311(3-4), p.320.

[115] Klinkenberg L. J.: *The permeability of porous media to liquids and gases*, Prod. Pract., 1941, p.200.

[116] Knudsen M.: *Die Gesetze der Molekularströmung und der inneren Reibungsströmung der Gase durch Röhren*, Ann. Physik, 1909, 28, p.75.

[117] Scott D.S., Dullien F.A.L.: *The flow of rarefied gases*, AIChE J., 1962, 8, p.293.

[118] Tiller F. M., Hsyung N. B.: *Theory of filtration of ceramics: II, slip casting on radial surfaces*, J. Am. Ceram. Soc., 1991, 74 (1), p.210.

[119] Gu Y., Meng G.: *A model for ceramic membrane formation by dip-coating*, J. Europ. Ceram. Soc., 1999, 19, p.1961.

[120] Elmaleh S., Jaafari K., Julbe A., and Cot L.: *Increasing permeability of a composite inorganic membrane*, K. Eng. Mat., 1991, 61&62, p.131.

[121] Chemikalien Reagenzien, Merk KgaA.

[122] Craig F. F. Jr., *The Reservoir Engineering Aspects of Water-flooding*, Society of Petroleum Engineers of AIME, Monograph, Dallas, Texas, 1971, 3.

[123] Wenzel R. N., Ind. Eng. Chem, 1936, 28, p.988.

[124] Wenzel R. N., J. Phys. Coll. Chem, 1949, 53, p.1466.

[125] Popiel W. J.: *Introduction to Colloid Science*, New York, Exposition Press, Hicksville, 1978.

[126] Melrose J.C., Soc. Petr. Eng. J., 1965, 5, p.259.

[127] McCaffery F. G., Bennion D. W., J. Can. Pet. Technol., 1974, 13, p.42.

[128] DE 4120706

[129] EP 0525325

7 Appendix

7.1 Calculation the Surface Area of Tubular Samples

For the hollow cylinder the wall thickness L and the measurement surface A yield the following correlation:

$$L = \frac{D \cdot (\ln \gamma)^2}{2(\gamma - 1)} \tag{A.1}$$

$$A = \frac{\pi \cdot D \cdot L_t \cdot \ln \gamma}{\gamma - 1} \tag{A.2}$$

where D is the outside diameter of the tube, d is the inside diameter, L_t is the length of the tube, and $\gamma$is defined as:

$$\gamma = \frac{D}{d} \tag{A.3}$$

If the wall thickness $\frac{D-d}{2}$ is very small comparing with the inside diameter of the tube d, for example smaller than 0.1d, then L and A can be approximated by:

$$L = \frac{D-d}{2} \tag{A.4}$$

$$A = \frac{\pi \cdot L_t \cdot (D+d)}{2} \tag{A.5}$$

7.2 Programming Code for Fluid Flow

Input File

INPUT1.DAT

```
==========================================================================
 Input data: calculating the flow rate by water
==========================================================================
Viscosity of the fluid [Pa.s], VMIU
1.005D-03
Thickness of different layers [m], AL(I), I=1,4
20.0D-06, 150.0D-06, 250.0D-06, 3000.0D-06
Pore diameters of different layers [m], DH(I), I=1,4
1.0D-07, 1.0D-06, 2.5D-06, 17.0D-06
Average particle size of different layers [m], DP2(I), I=1,4
1.5D-06, 2.94D-06, 8.79D-06, 100.0D-06
Porosity of different layers [%], FAI(I), I=1,4
9.0D-02, 20.0D-02, 22.5D-02, 43.0D-02
Pressure drop [mbar], DELTP
300.0
Measured area [PAI*DI*L-tube, m2], A
5940.0D-06
```

INPUT2.DAT

```
==========================================================================
 Input data: calculating the thickness of TiO2 layer
==========================================================================
Viscosity of the fluid [Pa.s], VMIU
1.005D-03
Thickness of different layers [m], AL(I), I=2,4
180.0D-06, 250.0D-06, 2100.0D-06
Pore diameters of different layers [m], DH(I), I=1,4
1,0D-07, 0.8D-06, 2.0D-06, 19.0D-06
Average particle size of different layers [m], DP2(I), I=1,4
1.5D-06, 2.94D-06, 8.79D-06, 50.0D-06
Porosity of different layers [%], FAI(I), I=1,4
9.0D-02, 20.0D-02, 22.5D-02, 36.0D-02
A given flow rate [m3/s], Q
1.0D-08
Pressure drop [mbar], DELTP
300.0
Measured area [m2], A
4553.0D-06
```

Main Program

```
PROGRAM FlUIDFLOW
C!
C!*************************************************************************
C!    Version of 05.02.2003                                                !
C!-----------------------------------------------------------------------------------------------!
C!    Calculation of the flow rate of a graded filter membrane             !
C!    The test medium is fluid (water).                                    !
C!    The program can be also used to calculate the thickness of          !
C!    the active TiO2 layer.                                               !
C!*************************************************************************
C
      IMPLICIT INTEGER (I-N), DOUBLEPRECISION (A-H, O-Z)
      CHARACTER DATE1*70, WORT*70
      DIMENSION AL(4),DH(4),DP2(4),ODELTP(4),CHDELTP(3),FAI(4),PERK(4)
C
C-------10--------20--------30--------40--------50--------60--------70
C2345678901234567890123456789012345678901234567890123456789012345678901234567890
C
C*** Initialisation of the program
C
      OPEN (1, FILE = 'DEFINE.DAT', STATUS='OLD')
      OPEN (2, FILE = 'INPUT1.DAT', STATUS='OLD')
      OPEN (3, FILE = 'INPUT2.DAT', STATUS='OLD')
      OPEN (4, FILE = 'OUTPUTF1.DAT')
      OPEN (5, FILE = 'OUTPUTF2.DAT')
      OPEN (6, FILE = 'OUTPUTT3.DAT')
C
```

```
      READ (1,100) DATE1
      READ (1,200) WORT
      READ (1,100) DATE1
      READ (1,*)   M
C
      IF (M.EQ.1) THEN
C
C!*****************************************************************************
C!    Input the data from the file "INPUT1.DAT" to calculate                    !
C!    the flow rate
C!*****************************************************************************
C
      READ (2,100) DATE1
      READ (2,200) WORT
      READ (2,100) DATE1
      READ (2,200) WORT
C
      READ (2,*) VMIU
C
      READ (2,200) WORT
      READ (2,*) (AL(I), I=1,4)
C
      READ (2,200) WORT
      READ (2,*) (DH(I), I=1,4)
C
     READ (2,200) WORT
     READ (2,*) (DP2(I), I=1,4)
C
     READ (2,200) WORT
     READ (2,*) (FAI(I), I=1,4)
C
     READ (2,200) WORT
     READ (2,*) DELTP
     DELTP=DELTP*1.013D+02
C
     READ (2,200) WORT
     READ (2,*) A
C
C!*****************************************************************************
C!     Calculating the flow rate                                                !
C!*****************************************************************************
C
       ODELTP(1)=100.0
       U0=0
       CALL PERMEAR(DP2,FAI,PERK)
C
C    WRITE (4,300)
C
  10   U0=(ODELTP(1)/AL(1))*(PERK(1)/VMIU)
C
       DO I=1,3
       CALL PERMEAR(DP2,FAI,PERK)
       ODELTP(I+1)=AL(I+1)*U0*VMIU/PERK(I+1)
       ENDDO
C
       DELTPC1=SUM(ODELTP)
       DIFP=DELTP-DELTPC1
C
        IF (DIFP.GE.1.0) THEN
        ODELTP(1)=ODELTP(1)+10.0
C
       DELTPC1=DELTPC1/1.013D+02
       U=U0
       Q=U*3600.0
C
       WRITE (4,500) DELTPC1, Q
C
        GOTO 10
        ELSE
        DELTPC1=DELTPC1/1.013D+02
        U=U0
        Q=U*3600.0
C
        WRITE (5,400)
        WRITE (5,600) DELTPC1, Q
C
        ENDIF
```

```
C
     ELSEIF (M.EQ.2) THEN
C
C!*****************************************************************************
C!    Input the data from the file "INPUT2.DAT" to calculate                    !
C!    the thickness of TiO2 layer
C!*****************************************************************************
C
        READ (3,100) DATE1
        READ (3,200) WORT
        READ (3,100) DATE1
        READ (3,200) WORT
C
        READ (3,*) VMIU
C
       READ (3,200) WORT
       READ (3,*) (AL(I), I=2,4)
C
       READ (3,200) WORT
       READ (3,*) (DH(I), I=1,4)
C
       READ (3,200) WORT
       READ (3,*) (DP2(I), I=1,4)
C
       READ (3,200) WORT
       READ (3,*) (FAI(I), I=1,4)
C
       READ (3,200) WORT
       READ (3,*) Q
C
       READ (3,200) WORT
       READ (3,*) DELTP
       DELTP=DELTP*1.013D+02
C
      READ (3,200) WORT
      READ (3,*) A
C
C!*****************************************************************************
C!     Calculating the thickness of the TiO2 layer                              !
C!*****************************************************************************
C
     U=Q/A
C
     DO I=2,4
     CALL PERMEAR(DP2, FAI,PERK)
     ODELTP(I)=AL(I)*U*VMIU/PERK(I)
     CHDELTP(I)=ODELTP(I)
     ENDDO
C
     DELTPC2=SUM(CHDELTP)
     ODELTP(1)=DELTP-DELTPC2
C
     IF ((ODELTP(1)).LT.0.0) THEN
     WRITE (6,400)
     WRITE (6,900)
C
     ELSE
C
     CALL PERMEAR(DP2, FAI,PERK)
     AL(1)=(ODELTP(1)/U)*(PERK(1)/VMIU)
     AL(1)=AL(1)*1.0D+06
     WRITE (6,400)
     WRITE (6,700) Q,AL(1)
C
     ENDIF
C
    ENDIF
C
 100 FORMAT(A70)
 200 FORMAT(A70)
 300 FORMAT(3X,'Pressure drop [mbar]',10X,'Flow rate [m3/s]',/)
 400 FORMAT(1X,70('*'),/,20X,'O T P U T F I L E',/,
   &10X,' F L O W - R A T E - S I M U L A T I O N - by water',
   &/,1X,70('*'),/)
 500 FORMAT(10X,E12.6,10X,E12.6)
 600 FORMAT(10X,'Pressure drop [mbar]',5X,'Flow rate [m3/h*m2]',/,
   &     15X,E12.6,10X,E12.6)
```

```
 700 FORMAT(10X,'Flow rate [m3/s]',5X,'Thickness of TiO2 layer [μm]',
    &     /,10X,E12.6,10X,E12.6)
 900 FORMAT(5X,'The flow rate has surpassed the calculation range.')
C
     END
C
C
     SUBROUTINE PERMEAR(DP2,FAI,PERK)
C
C!*********************************************************************
C!    Calculating the permeability of different layer                  !
C!*********************************************************************
C
       IMPLICIT INTEGER(I-N), DOUBLEPRECISION (A-H,O-Z)
       DIMENSION DP2(4),FAI(4),PERK(4)
C!
       PERK=(DP2**2/180)*(FAI**3/(1-FAI)**2)
C!*********************************************************************
C!    Modification of the permeability by a coefficient                !
C!*********************************************************************
        PERK=PERK/9.0
C!
       RETURN
     END
```

7.3 Programming Code for Gas Flow

Input File

INPUT3.DAT

```
================================================================================
 Input data: calculating the flow rate by air
================================================================================
Atmosphere pressure [Pa], P
1.013E+05
Atmosphere temperature [K], T
293.0
Gas constant [J/(kmole.K)], R
8.31D+03
Molecular weight of air [kg/kmol], AM
28.964
Viscosity of air [Pa.s], YITA
1.82E-05
Mean free path of air [m], ALAMDA
6.08E-08
Pressure drop [mbar], DELTP
600.0
Thickness of different layers [m], AL(I), I=1,4
28.0E-06, 70.0E-06, 272.0E-06, 3000.0E-06
Pore diameters of different layers [m], DH(I), I=1,4
1.1E-07, 1.1E-06, 2.5E-06, 20.0E-06
Measured area (PAI*DI*L-tube) [m2], A
177.0E-06
```

Main Program

```
PROGRAM GASFLOW
C!
C!*****************************************************************************
C!    Version of 05.02.2003                                                    !
C!---------------------------------------------------------------------------------------------------!
C!    Calculation of the flow rate of a graded filter membrane                 !
C!    The test medium is gas (air).                                            !
C!*****************************************************************************
C
    IMPLICIT INTEGER (I-N), DOUBLEPRECISION (A-H, O-Z)
          CHARACTER DATE1*70, WORT*70
          DIMENSION AL(4),DH(4),RA(4),ODELTP(4),PERKD(4)
          DATA STVOL/22.4136/
C
C-------10--------20--------30--------40--------50--------60--------70
C2345678901234567890123456789012345678901234567890123456789012345678901234567890
C
C*** Initialisation of the program
C
    OPEN (1, FILE = 'INPUT3.DAT', STATUS='OLD')
          OPEN (2, FILE = 'OUTPUTG1.DAT')
          OPEN (3, FILE = 'OUTPUTG2.DAT')
C
C!*****************************************************************************
C!    Input the data from the file "INPUT3.DAT" to calculate                   !
C!    the flow rate                                                            !
C!*****************************************************************************
C
          READ (1,100) DATE1
          READ (1,200) WORT
          READ (1,100) DATE1
C
          READ (1,200) WORT
          READ (1,*) P
C
          READ (1,200) WORT
          READ (1,*) T
C
          READ (1,200) WORT
          READ (1,*) R
C
          READ (1,200) WORT
          READ (1,*) AM
```

```
C
            READ (1,200) WORT
            READ (1,*) YITA
C
            READ (1,200) WORT
            READ (1,*) ALAMDA
C
            READ (1,200) WORT
            READ (1,*) DELTP
            DELTP=DELTP*1.013D+02
C
            READ (1,200) WORT
            READ (1,*) (AL(I), I=1,4)
C!*************************************************************************
C!     Modification of the effective length                                !
C!*************************************************************************
C
            DO I=1,4
              AL(I)=AL(I)*3.0
            ENDDO
C
            READ (1,200) WORT
            READ (1,*) (DH(I), I=1,4)
C
            READ (1,200) WORT
            READ (1,*) A
C
C!*************************************************************************
C!     Calculating the flow rate                                           !
C!*************************************************************************
C
    ODELTP(1)=100.0
    UG0=0
C
            DO I=1,4
              RA(I)=DH(I)/2.0
            ENDDO
C
            PM=P+ODELTP(1)/2.0
C
    CALL PERMEARG(PM,R,T,AM,YITA,ALAMDA,RA,PERKD)
C
C           WRITE (2,300)
C
 10  UG0=(ODELTP(1)/AL(1))*(PERKD(1)/PM)
C
      DO I=1,3
            CALL PERMEARG(PM,R,T,AM,YITA,ALAMDA,RA,PERKD)
      ODELTP(I+1)=AL(I+1)*UG0*PM/PERKD(I+1)
      ENDDO
C
      DELTPC2=SUM(ODELTP)
              DIFP=DELTP-DELTPC2
C
       IF (DIFP.GE.1.0) THEN
       ODELTP(1)=ODELTP(1)+1.0
C
                DELTPC2=DELTPC2/1.013D+02
                UG=UG0
                G=STVOL*P*UG/(R*T)*A*3600.0
C
                WRITE (2,500) DELTPC2, G
C
       GOTO 10
                ELSE
                DELTPC2=DELTPC2/1.013D+02
       UG=UG0
       G=STVOL*P*UG/(R*T)*A*3600.0
C
       WRITE (3,400)
                WRITE (3,600) DELTPC2,G
C
    ENDIF
C
 100        FORMAT(A70)
 200        FORMAT(A70)
 400        FORMAT(1X,70('*'),/,20X,'O U T P U T F I L E',/,
```

```
     &    10X,' F L O W - R A T E - S I M U L A T I O N - by air',/,
     &    1X,70('*'),/)
  500       FORMAT(10X,E12.6,10X,E12.6)
  600       FORMAT(10X,'Pressure drop [mbar]',5X,'Flow rate [m3/h]',/,
     &    15X,E12.6,10X,E12.6)
C
      END
C
C
      SUBROUTINE PERMEARG(PM,R,T,AM,YITA,ALAMDA,RA,PERKD)
C
C!*********************************************************************
C!    Calculation the permeability of different layer                  !
C!*********************************************************************
C
            IMPLICIT INTEGER(I-N), DOUBLEPRECISION (A-H,O-Z)
            DIMENSION RA(4),PERKD(4),Y(4),Z(4)
C           DIMENSION TT1(4),TT2(4)
            DATA PAI/3.14/
C
      UM=DSQRT(8.0*R*T/(PAI*AM))
            Y=2.0*RA/ALAMDA
            Z=DEXP(-DLOG(Y+DSQRT(Y**2+1.0)))
            PERKD=(1.0-Z)*(RA*R*T/(AM*UM)+RA**2*PM/(8.0*YITA))+Z*16.0
     &       *RA*R*T/(3.0*PAI*AM*UM)
C
            RETURN
      END
```

8 Nomenclature

A	filtration area; constant in Eq. (3.6.20)	[m^2]; [-]
B	constant in Eq. (3.6.21)	[-]
D	spraying distance between the gun tip and the sample	[mm]
D_H	hydraulic diameter	[m]
$\bar{D}_{P2}$	surface average equivalent sphere diameter	[m]
d	diameter	[m]
F	acting force	[N]
f	friction parameter	[-]
G	molar flow rate	[mole]
i	layer numbers:	
	i=1 — TiO_2; i=2, 3 — 316L intermediate layers; i= 4 — substrate	
K	constant in Eq. (3.6.14)	[-]
k	permeability	[m^2]
k'	Kozeny constant	[-]
k_0	shape factor	[-]
k_{CK}	permeability in Carman-Kozeny model	[m^2]
k_D	permeability in Scott-Dullien model	[m^2/s]
L	thickness in filtration direction	[m]
L_e	effective length	[m]
M	molecular mass; number parameter	[g/mol]; [-]
N	nozzle size	[mm]
P	pressure	[bar]
P_c	capillary pressure	[Pa]
P_m	mean pressure	[Pa]
P''	wetting phase pressure	[Pa]
P'	non-wetting phase pressure	[Pa]
ΔP	pressure drop	[Pa]
$\dot{Q}$	flow rate	[m^3/s]
$\dot{Q}_L$	flow rate	[m^3/s]
q_i	particle size distribution parameter	[m]
R	gas constant;	[J/mol·K]

	radius in Eq. (4.6.3)	[m]
r	radius; ratio of the ture-to-apparent area of the solid in Eq.(4.6.2)	[m]; [-]
S_0	specific surface area based on solid's volume	[m^2]
S_P	specific surface area in Eq. (3.6.10)	[m^2]
SA	amount of suspension	[scale]
SB	spraying beam	[scale]
s	stripe distance	[mm]
T	temperature	[K]
t	time	[s]
V	spraying speed	[mm/min]
V_G	moving speed of the spraying gun	[mm/min]
V_P	specific volume in Eq. (3.6.10)	[m^2]
W	ellipse length	[mm]
Greek symbols		
α	permeability coefficient	[m^2]
β	permeability coefficient	[m]
ϕ	porosity; angle	[%]; [°]
γ	tortuosity factor	[-]
η	gas viscosity	[Pas]
φ	wetting angle	[°]
λ	mean free path	[m]
μ	fluid viscosity	[Pas]
ν	kinetic viscosity	[m^2/s]
θ	contact angle	[°]
θ_a	average apparent contact angle	[°]
ρ	density	[kg/m^3]
σ	surface tension	[N/m]
σ_{sl}	surface tension between solid and liquid	[N/m]
σ_{sg}	surface tension between solid and gas	[N/m]
σ_{lg}	surface tension between liquid and gas	[N/m]
τ	shear strength	[M/m^2]
υ	velocity	[m/s]
υ_g	gas velocity	[m/s]

$\bar{v}_m$	mean molecular velocity	[m/s]
ω_R	rotation speed of samples	[1/min]
ψ_i	particle shape parameter	[-]

The present work was developed during the three-year employment in the Institute for Materials and Processes in Energy Systems (IWV-1) of Research Center Jülich.

I want to express deep appreciation to Prof. Dr. Deltev Stöver for his supervision in the choice of the topic, helpful discussion about the work and the review of the thesis. Many thanks to Prof. Werner Theisen for his work in evaluating the thesis and to Prof. Eckhard Weidner for the chairmanship during the examination.

I am most grateful to Dr. Hans Peter Buchkremer. His wise instructions led a right way to solve the problems in the work. I profit so much from his kindness and experiences. His humour strikes me impressively.

I want to especially acknowledge Dr. Martin Bram. Under his patient guidance I learned so much in the material field. His strict working attitude and acuminous insight in the research were of great benefit to me. Needless to say that without his extremely valuable contributions to this thesis it could be not finished smoothly.

I also want to express my sincere appreciation to my officemate Ms. Dr. Edith Schüller. Her kindness and discussion did me a great deal of good.

I also want to take this opportunity to thank Ms. Kiki Portulidou, Mr. Bert Hobein, Mr. Jörg Böhm, with their help the project could be finished in time and successfully.

I will never forget the nice women group in IWV-1 — Ms. Dr. Edith Schüller, Ms. Silke Latzel, Ms. Juliane Mentz, and Ms. Dr. Franziska Träger, whose support helped me to conquer many difficulties.

Many thanks to Mr. Mark Kappertz, Ms. Sigrid Schwartz-Lückge, Ms. Andrea Lemmens, Dr. Wolfgang Fische, Dr. Egbert Wessel, Ms. Dr. Doris Sebold, whose efficient work in the measurements ensure my experiments to be carried out smoothly.

I appreciate the strong help from Mr. Volker Bader, Mr. Wolfgang Jungen, Mr. Blaß, Mr. Coenen, Mr. Mottonet, Mr. Fred Oellers and Mr. Stefan Heinz in the experiments.

I thank Ms. Ina Staszewsk, Mr. Stefan Giesen and Ms. Philipps for their soon help in any computer problem. And I thank Ms. Hiltrud Moitroux for her wondeful photographs of my probes.

The nice colleagues — Dr. Cui, Dr. Dietrich, Dr. Döring, Dr. Fu, Dr. Guo, Dr. Hannsch, Mr. Krone, Mr. Laatsch, Fr. Dr. Lange, Dr. Lehmann, Mr. Mai, Dr. Malléner, Dr. Marqué-López, Dr. Menzler, Mr. Mertens, Dr. Meulenberg, Dr. Müller, Dr. Pracht, Dr. Reckers, Mr. Richter, Dr. Rutenbeck, Mr. Siegert, Dr. Tietz, Dr. Uhlenbruck, Dr. Vaßen and Dr. Zahid, I would also like to thank you all for the help and advice during the years.

Many thanks to Dr. Zi Li and Mr. Simon Steigert in GKN Sinter Metals GmbH for their nice co-operation in the project.

Finally I owe much to my parents for their support and encouragement at all the time. I would dedicate this work to my gone father. Especially I want to acknowledge the strong support and many sacrifices of my husband Dr. Runxi He.

Forschungszentrum Jülich
in der Helmholtz-Gemeinschaft

Jül-4079
August 2003
ISSN 0944-2952